

Uncertainty Analysis of Carbon Sequestration in an Inclined Deep Saline Aquifer

by
Guang Yang

A thesis submitted in partial fulfillment for the
degree of Master of Science

in the
Department of Geology and Geophysics
University of Wyoming

April 2012

Declaration of Authorship

I, Guang Yang, declare that this thesis titled, *Uncertainty Analysis of Carbon Sequestration in an Inclined Deep Saline Aquifer* and the work presented in it are my own. I confirm that:

- This work was done wholly or mainly while in candidature for a research degree at this University.
- Where any part of this thesis has previously been submitted for a degree or any other qualification at this University or any other institution, this has been clearly stated.
- Where I have consulted the published work of others, this is always clearly attributed.
- Where I have quoted from the work of others, the source is always given. With the exception of such quotations, this thesis is entirely my own work.
- I have acknowledged all main sources of help.
- Where the thesis is based on work done by myself jointly with others, I have made clear exactly what was done by others and what I have contributed myself.

Signed:

Date:

Abstract

Department of Geology and Geophysics

Master of Science

by Guang Yang

Geologic Carbon Sequestration (GCS) is a proposed means to reduce atmospheric carbon dioxide (CO_2). In Wyoming, GCS is proposed for the Nugget Sandstone, an eolian sandstone exhibiting permeability heterogeneity. Using subsets of static site characterization data, this study builds a suite of increasingly complex geologic model families for the Nugget Sandstone in the Wyoming Overthrust Belt, which is an inclined deep saline aquifer. These models include: a homogeneous model (FAM1), a stationary geostatistical facies model with constant petrophysical properties in each facies (FAM2a), a stationary geostatistical petrophysical model (FAM2b), a stationary facies model with sub-facies petrophysical variability (FAM3), and a non-stationary facies model (with sub-facies variability) conditioned to soft data (FAM4). These families, representing increasingly sophisticated conceptual models built with increasing amounts of site data, were simulated with the same CO_2 injection test (50-year duration at $\sim 1/3$ Mt per year), followed by a 2000-year monitoring phase.

Based on the Design of Experiment (DOE), an efficient sensitivity analysis (SA) is conducted for all model families, systematically varying uncertain input parameters, while assuming identical production scenario (i.e., well configuration, rate, BHP constraint) and boundary condition (i.e., model is part of a larger semi-infinite system where the injected gas can flow out). Results are compared among the families at different time scales to identify parameters that have first order impact on select simulation outcomes. For predicting CO_2 storage ratio (SR) and brine leakage, at both time scales (i.e., end of injection and end of monitoring), more geologic factors are revealed to be important as model complexity is increased, while the importance of engineering factors is simultaneously diminished. In predicting each of the trapped and dissolved gases, when model is of greater complexity, more geologic factors are identified as important with increasing time. This effect, however, cannot be revealed by simpler models.

Based on results of the SA, a response surface (RS) analysis is conducted next to generate prediction envelopes of the outcomes which are further compared among the model families. Results suggest a large uncertainty range in the SR given the uncertainties of the parameter and modeling choices. At the end of injection, SR ranges from 0.18 to 0.38; at the end of monitoring, SR ranges from 0.71 to 0.98. In predicting the SR,

during the entire simulation time, uncertainty ranges of FAM2b, FAM3, and FAM4 are larger than those of FAM1 and FAM2a, since the former models incorporate more geological complexities. The uncertainty range also changes with time and with the model families. By the end of injection, prediction envelopes of all families are more or less similar. Over this shorter time scale, where heterogeneities near the injection site are not significantly different among the different model representations, simpler models can capture the uncertainty in the predicted SR. During the monitoring phase, prediction envelope of each family deviates gradually from one another, reflecting the different (evolving) large scale heterogeneity experienced by each family as plume migrates and grows continuously. Compared to FAM4 (i.e., the most sophisticated model), all other families estimate higher mean SRs. The lesser the amount of site data are incorporated (i.e., lesser geological complexities), the greater the estimated mean SR. In terms of magnitude and range of the uncertainty, prediction envelope of FAM3 is the closest to that of FAM4, while FAM2b's uncertainty range is the largest and FAM1 and FAM2a's ranges are small.

Finally, end-member gas plume footprint for each family is established from results of the RS designs (i.e., corresponding to SR minimum, median, and maximum). For FAM1 and FAM2a, at each time scale inspected, the end-member gas plume footprints are not as drastically different as in FAM2b, 3, and 4, since their SR uncertainty range is comparatively small. However, for families of greater geological complexity (i.e., FAM2b, FAM3, and FAM4), the differences are much more significant: gas plume of minimum SR sits around the wellbore and doesn't migrate far, while gas plume of maximum SR migrates a great distance from the wellbore.

To summarize, geologic factors and associated conceptual model uncertainty can dominate the uncertainty in predicting SR, brine leakage, and plume footprint. At the study site, better characterization of geologic data such as porosity-permeability transform and facies correlation structure, can lead to significantly reduced uncertainty in predictions. Given the current uncertainty in parameters and modeling choices, CO₂ plume predicted by the majority of the simulation runs is either trapped near the injection site (e.g., due to low formation permeability and its heterogeneity) or is gravity-stable under conditions of higher permeability and lower temperature gradient, suggesting a low leakage risk. The inclined Nugget Sandstone at the study site appears to be a viable candidate for safe GCS in this region.

Acknowledgements

First and foremost, I would like to express my sincere thanks to my advisor, Prof. Ye Zhang for her guidance, encouragement, patience, and financial support over the last three years. I would also like to acknowledge my committee members: Prof. John Kaszuba and Prof. Timothy Robinson for their time and input.

My thanks are also extended to the previous postdoc, Dr. Shuiquan Li, and research associate, Baozhong Liu, for their support in addressing software problems.

I am also extremely grateful to our departmental support, staff and office associates, Sondra Cawley and Diane Gerhart for their patience and assistance. In addition to that, I want to give special thanks to my parents, sister, and dear friends for their love and support. I would also like to express my thanks to BP for an internship that enabled me to enhance my geologic modeling capabilities.

Finally, I wish to acknowledge the funding source for this study, NSF grant EAR-0838250.

Contents

Declaration of Authorship	i
Abstract	ii
Acknowledgements	iv
List of Figures	vii
List of Tables	x
Abbreviations	xi
Physical Constants	xii
Symbols	xiii
1 Introduction	1
2 A Review of Uncertainty Analysis	6
3 Methodology	10
3.1 DOE Methodology	11
3.2 Data Collection and Interpretations	12
3.2.1 Geological Cross Section and Isopach Data	12
3.2.2 Geophysical Well Logs	13
3.2.3 Petrophysical Data	14
3.2.4 Engineering Data	17
3.2.5 Uncertainty in the Data	17
3.3 Static Reservoir Modeling	23
3.3.1 Nugget Sandstone Reservoir Description	23
3.3.2 Nugget Sandstone Facies Characterization	24
3.3.3 Family Models With Increasing Geologic Complexity	26
3.3.4 Geologic Modeling Procedures	27
3.3.4.1 FAM4 Models	28
Structural Framework	29

Gridding	30
Upscaling of Well Logs	30
Petrofacies Modeling	30
Petrophyscial Modeling	32
Quality Check (QC)	36
Petrofacies Proportion	36
Porosity Distribution	37
Petrofacies Model	37
Porosity Depth Trend	37
Uncertain Factors Varied In The PB design	37
3.3.4.2 FAM3 Models	38
3.3.4.3 FAM2b Models	40
3.3.4.4 FAM2a Models	40
3.3.4.5 FAM1 Models	41
3.3.4.6 Comparison Between Model Families	41
3.4 Dynamic Modeling of CO ₂ Injection & Monitoring (Simulation)	43
4 Results and Discussion	45
4.1 Screening Tests	45
4.2 RS Modeling & Verification	48
4.3 MC Analysis	55
4.4 Plume Footprint	61
5 Conclusions	65
 A Example Script of Eclipse 300 GASWAT simulation	 68
 Bibliography	 83

List of Figures

1.1	A regional map of southwestern Wyoming showing the model location, well locations, production fields and Thrust Belts in this area. The study site (bold outline) lies between the Hogsback Thrust and the Absaroka Thrust. Wells used in this study that penetrate to the depth of the Nugget Sandstone are designated according to API number. The hollow crossings are core data of the equivalent Weber Sandstone from the Greater Green River Basin [1]. Not all the core measurement data used are shown, some are located outside the map area.	2
1.2	Cross section of A-A' showing the inclined feature of Nugget Sandstone modeled. A schematic section is also shown below the scaled cross section. Note that this schematic section is not drawn in true scale (the scale displayed above A-A' cross section doesn't apply to the lower diagram) and spans a larger regional area. In both figures, model extent is indicated by the dashed line. A generalized stratigraphic column is included.	3
3.1	Log plot of well 4120147. Phi: Φ ; PhiD: Φ_D ; PhiN: Φ_N ; ILD: deep resistivity log; SP: spontaneous potential log. In this well, core porosity measurements (Phi_Core) have been shifted in depth to be consistent with the calculated well log porosities (Phi_Calculated), since depth information of core measurements can be inaccurate because of the missing interval of core samples.	15
3.2	Log calculated porosity versus core measured porosity. The transform suggests that the core porosities are on average 92% of the well log porosities, indicating a slight bias in the well log calculated porosities, which may be attributed to different measurement support or difference between effective porosity (core measured porosity) and total porosity (well log calculated porosity).	16
3.3	k_h max and k_h min from available Nugget Sandstone core measurements	18
3.4	k_v and k_h from available Nugget Sandstone core measurements	19
3.5	Porosity distribution with depth, compiled from Nugget Sandstone core measurements from the neighboring regions. A possible depth trend is fitted and used for soft conditioning.	20
3.6	Based on core measurements, end members of k_h - Φ transform are developed for a single Nugget Sandstone without facies distinction (a) and for two dominant rock types (b).	22
3.7	Relative permeability model of end member sandstones. Berea Sandstone represents the -1 case while Cardium Sandstone stands for the +1 case [2].	22
3.8	Temperature versus depth measurements from the temperature logs. Two possible temperature-depth gradients are fitted.	23

3.9	Facies coded by petrophysical values cutoff (petrofacies at left) and by neural networks (facies at right).	26
3.10	Schematic diagram of the 4 geologic modeling families	27
3.11	Factors varied in the PB design and their ranges of variation. Numbers indicate family ID. Engineering/Environmental factors are shared by all model families. Facies and ϕ correlation range and azimuth are of the horizontal direction. -1: minimum values; +1: maximum values.	28
3.12	Regional structural model of the Nugget Sandstone. Depth is in feet at subsea level. Positive value is above sea level, while negative value is below sea level. Location of this model is indicated in Fig.1. Model uses 5x vertical exaggeration. The arrow points to the north.	29
3.13	Histogram of petrofacies in the upscaled cells versus histogram of petrofacies in the well logs.	31
3.14	Histogram of porosity in the upscaled cells versus histogram of porosity in the well logs.	31
3.15	Experimental variogram and variogram model of vertical facies sequences. The gray curve represents the auto-fitted regression curve, and the blue curve stands for the variogram used during the modeling process.	32
3.16	A global vertical petrofacies proportion curve generated from all the 8 wells at the study site.	33
3.17	Lateral probability map for each petrofacies type. Arrow points North. . .	34
3.18	Petrofacies model corresponding to the center run of PB design. Arrow points North.	34
3.19	Experimental variograms and variogram models of ϕ for each petrofacies in three directions. The gray curve represents the auto-fitted regression curve, and the blue curve stands for the variogram used during the modeling process.	35
3.20	Petrofacies histogram of the geostatistical model plotted against that of the upscaled cells at the well locations.	36
3.21	Porosity histogram of the geostatistic model plotted against that of the upscaled cells at the well locations.	37
3.22	A petrofacies model cross section corresponding to the center run of the PB design. Arrow points north.	38
3.23	Porosity change with depth of: (a) petrofacies 1 (b) petrofacies 2 (c) petrofacies 3 (d) petrofacies 4. Arrow points north.	39
3.24	A k_h model realization, one for each family.	42
4.1	An example screening test result for FAM4 at a 90% significance level. Outcome is the SR at EOM. Statistically significant factors here include ϕ - k transform, petrofacies range, and residual gas saturation. Negative t-ratio means increasing value of this factor will reduce SR.	45
4.2	Verification of the RS storage ratio at the screening design points for each family: (left) EOI; (right) EOM.	58
4.3	Schematic of MC simulations based on the RS proxy model generated from the RS design.	59
4.4	cdf of the RS-predicted SR for each family: (left) EOI; (right) EOM. "MC w/ RS" is generated with 500,000 MC simulations (exhaustive cdf); "RS design" is cdf constructed using results from RS runs.	60

4.5	Prediction envelope of RS-predicted SR for each family over the entire simulation times. SRs between points of observation are linear interpolations.	61
4.6	Gas saturation (mobile + trapped CO ₂) predicted by each family (arrow points North) at EOI: (Left) Minimum SR; (Middle) Median SR; (Right) Maximum SR.	62
4.7	Gas saturation (mobile + trapped CO ₂) predicted by each family (arrow points North) at EOM: (Left) Minimum SR; (Middle) Median SR; (Right) Maximum SR.	63

List of Tables

3.1	List of Nugget Sandstone core data collected.	14
3.2	k_v/k_h ratio end members for each petrofacies.	35
3.3	Average ϕ and k_h for each petrofacies, corresponding to the center run of the PB design.	36
3.4	PB design for FAM4, -1/0/1 indicate different levels of values assigned to a factor.	39
3.5	PB design for FAM3.	40
3.6	PB design for FAM2b.	41
3.7	PB design for FAM2a.	41
3.8	PB design for FAM1.	42
4.1	Significant factors identified by the PB design for each family that impact the prediction of different outcomes. Significance level = 90%; EOI: end of injection; EOM: end of monitoring.	46
4.2	Response surface design for FAM1.	49
4.3	Response surface design for FAM2a.	50
4.4	Response surface design for FAM2b.	51
4.5	Response surface design for FAM3.	52
4.6	Response surface design for FAM4.	53
4.7	Parameter estimates of a 2nd order polynomial RS model of storage ratio for FAM4 at EOI.	56
4.8	An example of RS predicted SR values versus simulated SR values at PB design points for FAM4 at EOI. Comparison is for verification of the RS fitted model.	57
4.9	Summary of the RS error at the PB design points: Error = RS-predicted SR - simulated SR at PB points.	57

Abbreviations

BC	B oundary C ondition
DoE	D esign of E xperiment
EEF	E ngineering / E nvironmental F actors
EOI	E nd O f I njection
EOM	E nd O f M onitoring
FCA	F acies C orrelation A zimuth
FCR	F acies C orrelation R ange
GCS	G eologic C arbon S equestration
GF	G eologic F actors
MC	M onte C arlo
PB	P lackett B urman
PCA	P orosity C orrelation A zimuth
PCR	P orosity C orrelation R ange
PPT	P orosity~ P ermeability T ransform
RGS	R esidual G as S aturation
RPM	R elative P ermeability M odel
RS	R esponse S urface
SA	S ensitivity A nalysis
SAL	S ALinity
SGS	S equential G aussian S imulation
SIS	S equential I ndicator S imulation
SR	S torage R atio
TDS	T otal D issolved S olids
TG	T emperature G radient
VHR	V ertical / H orizontal-permeability R atio

Physical Constants

Gravity Coefficient $g = 9.81 \text{ m/s}^2$ (approximate)

Symbols

ϕ	porosity	dimensionless
k	permeability	mD
k_h	horizontal permeability	mD
k_v	vertical permeability	mD
ϕ_D	density log derived ϕ	mD
ϕ_N	ϕ from neutron porosity log	mD
ρ_m	matrix/grain density	g/cm ³
ρ_b	bulk density from density log	g/cm ³
ρ_f	fluid density	g/cm ³
$k_{h\max}$	permeability along the direction which fluids flow through most easily	mD
$k_{h\min}$	permeability along the direction 90 degree to that of $k_{h\max}$	mD

Dedicated to my parents and to my dear sister

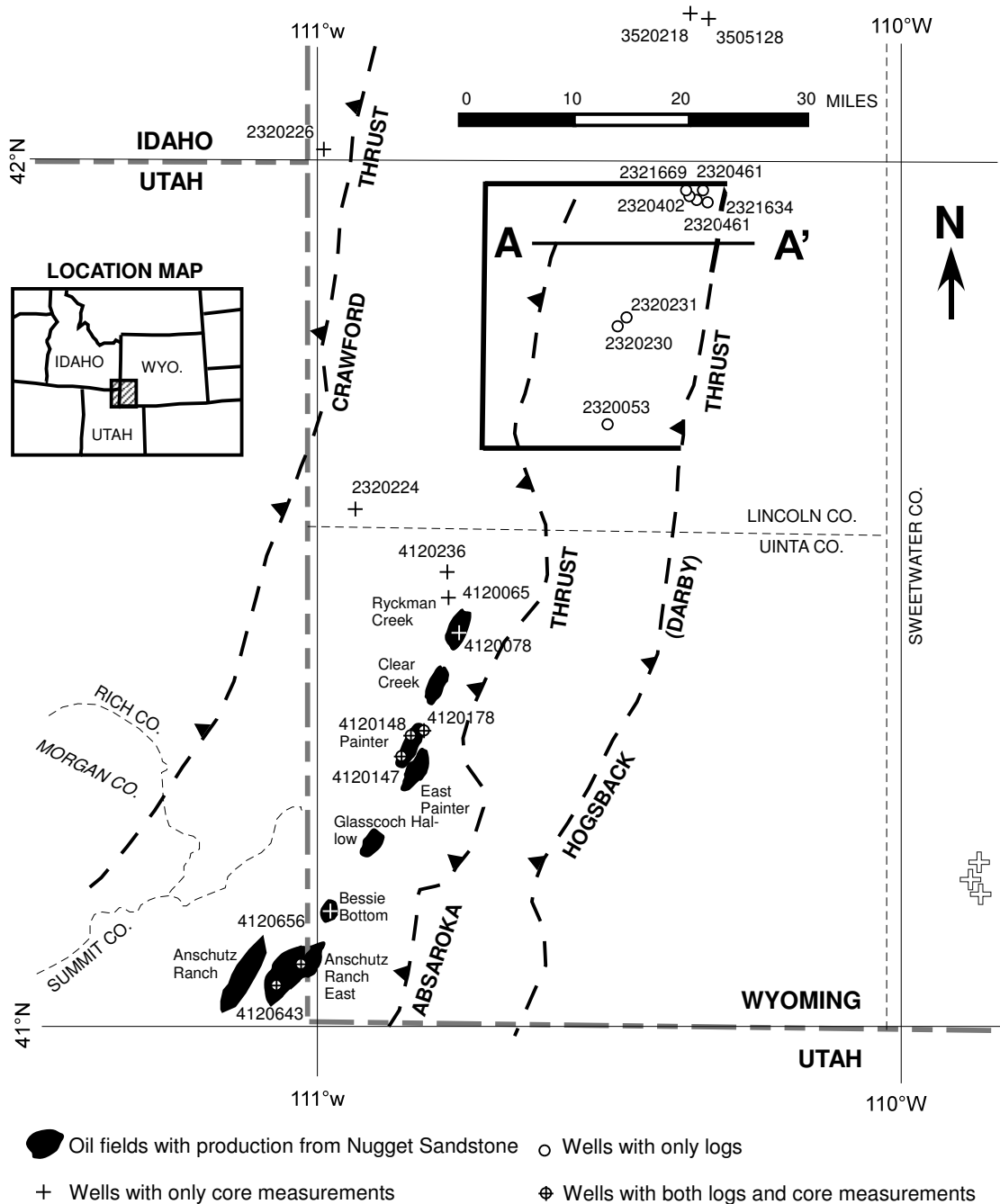
Chapter 1

Introduction

Carbon dioxide (CO_2) is believed to be the main cause of global climate change. Due to human activities, the level of CO_2 in the Earth's atmosphere is rising with severe implications for the environment. The International Panel on Climate Change (IPCC) predicts that the CO_2 concentration in the atmosphere may reach 570 ppmv by the year 2100, resulting in a rise of mean global temperature of around 3.42 °F (1.9 °C) and an increase in mean sea level of 38m [3].

To reduce the amount of CO_2 entering the atmosphere, a variety of actions have to be taken. Geological carbon sequestration (GCS) into deep saline aquifers is considered a promising option to mitigate global climate change [3]. Wyoming produces approximately 40% of the nation's coal and in 2000, coal-fired power plants in the state emitted a total of 51 million tons of CO_2 into the atmosphere. The emission rate is projected to increase with new energy demand [4], thus these power plants are chief targets for conversion to allow the capture of CO_2 and subsequent sequestration underground. To achieve large scale sequestration, deep saline aquifers with large storage capacity are needed. As part of a larger study investigating suitability of various geologic formations for GCS in Wyoming [5], this study investigates the Nugget Sandstone in the Overthrust Belt, which is a deep saline aquifer with a large storage potential (Figure 1.1). The study site is situated close to the 30 MW Green River Power Plant and the 2.1 GW Jim Bridger Power Plant.

In evaluating a GCS storage site, reservoir simulation is commonly performed using a geologic site model which describes subsurface structure, facies, and heterogeneity [3]. However, unlike petroleum reservoir modeling, GCS is a "cost center". To resolve detailed subsurface heterogeneity, expensive characterization effort is required. The greater the detail, the higher the cost. For the type, amount, and accessibility of data at a proposed storage site, different geologic models can be built, ranging from simple to



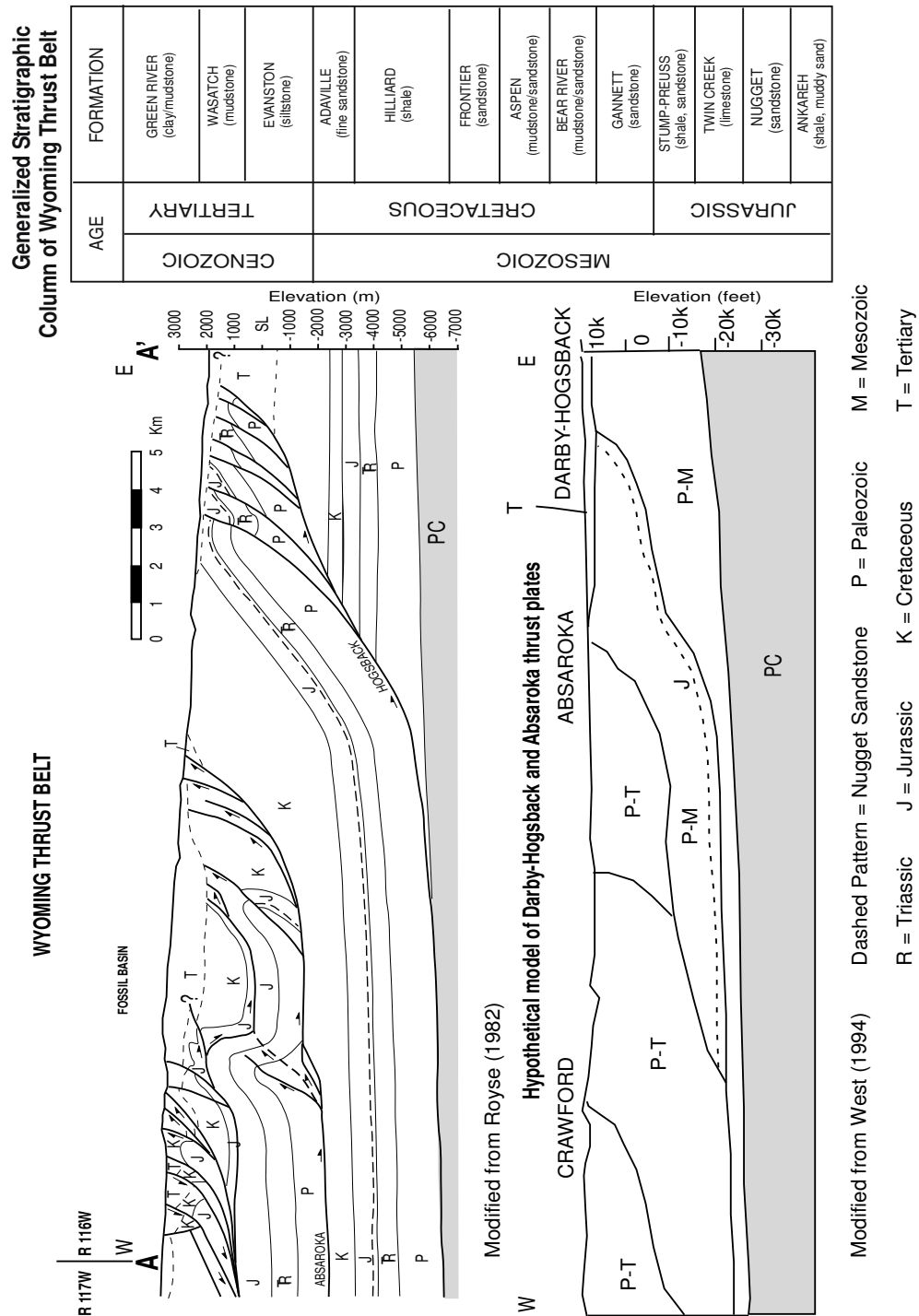


FIGURE 1.2: Cross section of A-A' showing the inclined feature of Nugget Sandstone modeled. A schematic section is also shown below the scaled cross section. Note that this schematic section is not drawn in true scale (the scale displayed above A-A' cross section doesn't apply to the lower diagram) and spans a larger regional area. In both figures, model extent is indicated by the dashed line. A generalized stratigraphic column is included.

complex. For example, petrophysical properties can be alternatively modeled assuming homogeneity or heterogeneity, the later requiring advanced modeling techniques supported by additional detailed data. Although such data can be obtained from drilling and logging the aquifer or high-resolution geophysical surveys, extensive borehole sampling or high-resolution surveys are not realistic for large aquifers designated for commercial CO₂ storage due to the significant cost constraint characterizing such data-poor settings. Thus, an important issue in GCS site assessment studies is to determine the right types of data to collect, and, based on these data, the right type of geologic model to construct, leading to a cost-effective strategy in data collection. An appropriate geologic model, as input to reservoir simulation, will ideally lead to adequate or sufficiently accurate predictions of the desired GCS performance measures, while models are not overly detailed and thus cost-prohibitive to construct.

In evaluating a GCS site, in addition to the cost issue, storage security in terms of leakage risk of the injected CO₂ back to the surface is an important concern [3]. At the typical depths considered for GCS (1~3 km), CO₂ is a supercritical fluid (referred to as “gas” herein) with a lower density than that of formation brine, thus its migration is driven by buoyancy, where the injected gas rises and flows toward the caprock. However, in large-scale storage where footprint of the injected gas is significant, finding perfect caprock at regional scales is problematic, as a variety of leakage pathways can exist in the caprock, including faults and fractures, lateral facies changes, and abandoned and possibly leaky wellbores [6]. To reduce the leakage risk, deeper injection where CO₂ is gravity-stable provides an attractive alternative: when the aquifer is sufficiently deep, CO₂ injected under high pressure may have a density exceeding that of formation brine [7], thus the injected gas can sink to the bottom of the aquifer instead of rising upwards [8]. Deeper injection also gives rise to a higher storage capacity, as more CO₂ mass can be stored per unit pore volume [9]. To date, deeper injection has not been investigated extensively in GCS field pilots or numerical simulation studies [10], though limited evidence suggests its viability. For example, in the Moxa Arch east of the Overthrust Belt, acid gas disposal into the Madison Limestone has been ongoing since 2005 without reporting leakage. At the Shute Creek gas plant (acid gas injection facility), Madison Limestone lies at a depth of ~5 km [5], greatly exceeding the depths typically considered for GCS.

This study aims to understand geologic model complexity and the associated data needs for simulating GCS in an inclined Nugget Sandstone formation in the Overthrust Belt. Here, the formation is a deep regional aquifer buried at depths up to 20,000 ft (6 km) (Figure 1.2). Although multiple Nugget Sandstone horizons occur in the region, this particular one is of interest for this study to investigate CO₂ storage and potential leakage from an inclined formation: when the injection depth is moderate, CO₂ density

could be lower than that of the formation brine and an inclined formation will accelerate up-dip migration, thus increasing leakage risk [11]; when the injection depth is higher, gravity-stable injection is possible due to increased CO₂ density (downdip migration is now possible, contributing to greater storage security). In addition, besides depth, other factors can influence CO₂ density, thus the direction of migration. For example, increasing reservoir temperature may reduce CO₂ density, offsetting the effect of increased depth. Low-permeability structures near the injector may create barriers to flow, regardless of its migration direction. These factors are uncertain at the proposed site and need to be analyzed systematically.

Within an uncertainty analysis framework, this study analyzes both model complexity in predicting GCS performance measures and the competing processes and effects that can influence CO₂ migration and leakage. For the Nugget Sandstone, the potential of gravity-stable CO₂ migration within it will be evaluated. The gravity-stable CO₂ migration here is defined as CO₂ migrating downward instead of upward, which would minimize leakage risk. The inclined formation may serve as an analog site for other deep saline aquifers in basins where connections to the surface or shallow subsurface exist. Here, though a site-specific study is presented, the uncertainty analysis methodology is applicable to analyzing other depositional environments. Though GCS is the application of interest, the methodology can be applied to oil/gas operations to facilitate the evaluation of important uncertainty factors influencing key economic metrics. In the next chapter, a review of the uncertainty analysis is introduced, before the study methodology is presented. Results are summarized leading to our conclusion and future research.

Introduction

Chapter 2

A Review of Uncertainty Analysis

In building and simulating a GCS model, a variety of uncertainty factors exist, including geological factors and conceptual modeling choices that influence reservoir heterogeneity, and engineering/environmental factors that influence gas trapping and migration. Numerous simulation studies have been conducted to model CO₂ flow in a variety of settings. The most frequent assumption made at various scales is aquifer homogeneity, as constrained by the quality and accessibility of site-specific data. However, permeability heterogeneity is the rule rather than the exception in natural aquifers [12], which exerts a significant impact on the subsurface behavior of the injected CO₂ [13]. Considering that the effective or equivalent parameters are routinely used to model field injections, understanding of the impact of effective parameterization on model predictions is needed [14]. Detailed characterization of heterogeneity, if available, is often limited to those of site-specific borehole data, which can be too sparse to resolve the main heterogeneity features. Facies modeling can be used to capture reservoir-scale geological features that are relevant to GCS. However, different geostastical methods can create different degrees of heterogeneity and connectivity (i.e. well-connected facies versus poorly connected facies).

Engineering and environmental factors can also influence CO₂ flow and its storage/trapping behavior in the formation. For example, there appear to be increasing concerns about the effect of relative permeability hysteresis on CO₂ residual trapping in the gas phase [15] [16] [17] [11]. Based on this effect, different injection strategies have been proposed to enhance residual trapping [18] [19]. A storage method that does not rely on impermeable cap rock to contain the CO₂ has been proposed by injecting CO₂ and brine into an aquifer together, followed by brine injection alone [20]. Due to CO₂ relative permeability hysteresis, 80 to 95% of the CO₂ can be immobilized in the form of

pore-scale droplets in the porous rock. While research is ongoing to determine the appropriate relative permeability model within the continuum framework, CO₂ modeling has invoked both hysteric and non-hysteric formulations. Furthermore, in sedimentary basins, aquifers considered suitable for GCS exist at different depths, exhibiting a wide range of temperature and pressure conditions. By exerting a significant effect on the injection behavior (i.e., pressure, phase separation), the in-situ CO₂ fluid properties (density, viscosity) need to be better understood [21]. Also, differences in formation brine salinity can affect CO₂ solubility: the greater the salinity, the lesser the dissolved CO₂ in brine. In addition, injection response also differs with boundary condition(BC): reservoir pressure will build up in closed and semi-closed systems, limiting the amount of CO₂ that can be injected [22].

Difference in simulation outcomes can be caused by the various settings of the fluid flow simulators. Industrial simulation software offers the industry's most complete and robust set of numerical solutions for fast and accurate prediction of dynamic behavior for all types of reservoirs and degrees of complexity including structure, geology, fluids, and development schemes. Other simulators have been developed, or are under development, that specifically deal with CO₂ storage. Stauffer et al. (2008) conducted CO₂ injection simulations on a 3D hydrostratigraphic model of the Rock Springs Uplift using FHEM (Los Alamos National Lab) [4]. Yamamoto et al. (2009) modeled industrial-scale CO₂ injection in Tokyo Bay using a parallel multiphase flow simulator TOUGH2-MP/ECO2N (Lawrence Berkeley National Lab) [23].

All above sources of uncertainties contribute to uncertainty in predicting CO₂ storage in geologic formations. Given the limited budget and often extremely high cost of exploring these uncertainties, an assessment of the most influential uncertainty factors is critical. Such factors once identified, would be those that need to be better characterized, reducing their uncertainties and thus the uncertainty in prediction. However, in building a geologic site model, as more complexity is incorporated, more geologic uncertainty factors come into play. As demonstrated in this study, the list of "heavy hitters" (i.e., factors whose variations have significant impact on a prediction outcome) can change with the modeling choice. This issue is not limited to GCS, but reflects a key problem in subsurface uncertainty analysis. In this research, a systematic effort is made to probe into this issue, with the aim of obtaining insights to facilitate the development of cost-effective GCS models that are accurate in assessing CO₂ storage and leakage. In the following discussion, a review of uncertainty analysis is presented.

In subsurface modeling, uncertainty analysis is usually initiated with a parameter sensitivity analysis (SA). Traditionally, SA is conducted one parameter at a time to evaluate the sensitivity of model outcomes in response to parameter variation [24]. For each

parameter varied, 3 values are typically defined (e.g., P10, P50, P90), reflecting a prior assessment of parameter uncertainty. A base-case simulation run is defined with all parameters assuming P50 levels. In additional runs, a parameter is set at its P10 level and then its P90 level, while all other parameters are kept at their P50 levels. (Given N parameters varied, $2N+1$ simulations are needed.) Tornado diagrams are generated to rank the effect of each parameter on a given outcome, although this ranking can be biased, since the runs do not explore the full parameter space, e.g., parameter combinations on parameter space boundary are not evaluated. The SA also assumes that all parameters varied are independent from one another, although in reality parameters are often correlated. To overcome these issues, alternative techniques are developed based on Monte Carlo (MC) sampling. For example, uncertainty of an outcome is estimated by assuming probability density functions (pdfs) for all uncertain input parameters. In MC sampling, values of the uncertain parameters are randomly drawn from these pdfs. Based on the sampling, a reservoir simulation is conducted. Distribution of the outcome is evaluated by repeated MC calls and thus repeated simulations. However, this method, though conceptually straightforward, is computationally intensive as often hundreds, if not thousands, of runs are needed to adequately sample the parameter space. This becomes an issue with large models requiring long simulation times. A practical way to overcome this is to develop a computationally efficient proxy model for the reservoir simulator.

Design of Experiment (DoE) methodology is a promising new tool in reservoir uncertainty analysis. DoE aims to fully explore the parameter space, is computationally efficient, and does not assume parameter independence. Its results can be used to create a Response Surface (RS) model, an analytic function that can be quickly evaluated for any parameter combinations. After suitable verification, the RS model becomes a proxy model for reservoir simulation. An MC analysis can then be conducted with the RS model to assess uncertainty in the model outcomes. This analysis is orders of magnitude faster than that based on reservoir simulations. Due to its efficiency and flexibility, DoE has been widely applied in analyzing static (i.e., pore volume) and dynamic reservoir properties [25] [26]. For example, studies have focused on identifying geologic factors that influence reservoir heterogeneity and flow behaviors, ignoring uncertainty in engineering parameters [27] [28] [29] [30] [31] [32] [33]. Other studies focus on the importance of engineering factors, while assuming a fixed geologic model [34] [35] [36] [37] [38]. Some studies look at both sources of uncertainty [39] [40], while others have incorporated both into reservoir history matching and optimization [41] [42] [43] [44]. In analyzing CO₂ modeling (mostly in EOR applications), DoE and RS have also been implemented, but the majority of the studies focuses on engineering factors that assume a fixed geologic model [45] [46] [47] [48] [49] [50]. In a few cases, permeability variance

or anisotropy ratio is varied, although reservoir heterogeneity pattern is fixed [51] [52]. It is worth noting that the majority of sensitivity analysis in GCS modeling relies on the traditional SA approach, varying one or two parameters at a time [53] [54].

To date, few studies have investigated the full range of geologic, engineering, and environmental uncertainty in GCS modeling. For an inclined deep aquifer, this study conducts an uncertainty analysis of GCS modeling according to the DoE methodology. Using subsets of static site characterization data, multiple families of geologic models are built at increasing complexities. Important uncertainty parameters are identified for each family, before an RS analysis is conducted to assess uncertainty in predicting CO₂ storage. Results are analyzed and compared among the families, yielding insights into the effect of model complexity on parameter importance and prediction uncertainty. Since CO₂ flow is dominated by viscous forces during injection and gravity force during monitoring, the list of the most influential factors with regard to a selected set of prediction outcomes may change over time, as well as the uncertainty in predictions themselves. Thus, all uncertainty measures are evaluated at multiple time scales. In the following section, we provide an overview of the DoE method, before the static and dynamic modeling approaches are introduced.

A Review of Uncertainty Analysis

Chapter 3

Methodology

The uncertainty analysis is outlined below, consisting of three steps (parameters varied in the SA are also referred to as factors):

- (1) Using subsets of site characterization data, generate 4 families of geologic models with increasing complexity, from a deterministic homogeneous model to a hierarchical stochastic model conditioned to hard and soft data;
- (2) For each family, conduct a SA with a screening design to identify key uncertainty factors that impact select simulation outcomes, as: (a) important factors that need to be better characterized; (b) input to an RS uncertainty analysis;
- (3) For each family, after pooling together all the important factors identified over different time scales during step (2), conduct an RS analysis to assess prediction uncertainty of select outcomes. This analysis consists of: (a) generating an RS design based on the important factors; (b) verifying of the RS model; (c) creating of prediction envelope of the outcomes with the verified RS model; (d) comparing of uncertainty in the outcomes among the families.

In steps (2) & (3), the outcomes are: brine leakage through the formation top and the side boundary near the ground surface, residual CO₂, dissolved CO₂, and CO₂ mass storage ratio: $SR = (\text{dissolved} + \text{residual CO}_2) / (\text{total injected CO}_2)$. Residual CO₂ is gas-phase CO₂ trapped in the formation pore space. In the deeply buried Nugget Sandstone, velocity of the groundwater is expected to be low, thus most of the dissolved CO₂ is considered immobile. The dissolved and residual CO₂ are immobilized, while the

mobile free-phase CO₂ continues its migration, driven by the density contrast with that of the formation brine. All outcomes are examined at 7 different times, including end of injection (EOI) and end of monitoring (EOM).

3.1 DOE Methodology

The geologic model families are created according to specifications outlined in the DoE. For each family, a SA is conducted by simultaneously varying a subset of the uncertain input parameters according to a design table [55]. The parameters varied can be continuous or categorical, the later often reflecting modeling choices. Results of DoE are compiled and examined with Multivariate Analysis of Variance (MANOVA) to identify parameters that have statistically significant effects on a simulation outcome. Though a variety of designs are available (the same design can be used for analyzing multiple outcomes), a two-level Plackett-Burman (PB) design is used here, which is most effective when parameters varied are orthogonal, i.e., uncorrelated. For all families, a center run is added to the PB design, i.e., all parameters assume median values. This center run is used to evaluate the curvature-level of parameter interaction and non-linearity. Compared to other designs, PB is parsimonious in selecting a parameter subset for simulations, providing large savings in program execution time. However, the PB design can only identify main effects as well as confounding interactions with the main effects. It is the most useful as a screening tool to identify significant uncertainty factors with minimum simulation runs. In reservoir analysis, PB design alone is used in scoping studies to guide early data collection [28] [32] [33], while PB combined with RS designs is effective in analyzing a variety of uncertainty measures [40] [31] [35].

The RS analysis consists of fitting an analytical function to a simulation outcome [56]. This function is generated by running reservoir simulations according to an RS design using factors previously identified by the screening (PB) design as important to predicting the outcome. In the RS design, three values for each factor are necessary, i.e., -1/0/+1, which can correspond to key probabilities of a factor, though it is not a requirement. Based on the simulated outcomes, an RS model, here a quadratic polynomial, is fitted using the least square method. Though other fitting methods exist (e.g., kriging, splines, neural net), the quadratic polynomial is found accurate and robust in analyzing reservoir models [39] [26] [35]. The RS model is first verified at points in the parameter space that do not concur with the RS design. In this study, these points are selected at the PB design points, which lie on the boundary of the parameter space. According to [26], such extreme test runs can exaggerate the RS errors, though this decision can lead to significant savings in computation. After verification, the RS model is considered a

proxy for reservoir simulation, i.e., a predictive model of the relationship between the important input factors and simulation outcomes (responses). MC sampling is then run on the RS by randomly drawing the factors according to their respective pdfs, leading to a pdf of the outcome.

It's worth pointing out that a variety of RS designs are available, e.g., Space Filling, fractional factorial, Latin Hypercube, D-optimal, Central-Composite, although a “best” design is often problem dependent. Thus, researchers rely on verification to test the robustness of the chosen design in replicating simulated values at non-design points. In this study, Central-Composite designs are used. Results are verified at the PB design points. In the MC analysis, to assign pdf to each uncertain input factor (including continuous and categorical variables), a Gaussian distribution is assumed for most factors (i.e., the +1/-1 range corresponds to $\sim 99\%$ probability), since information on exact pdf shapes is lacking. An uniform distribution for relative permeability model is assigned, thus each end member function is assumed to exist in equal probability. The DoE and RS analysis is performed with JMP 9.0, a package developed by Statistical Analysis Software, Inc.

In the DoE, input parameters for CO₂ simulation are either fixed (those that vary little in a typical GSC site) or variable (the so-called “factors”). The later group includes geologic factors (GF) and engineering/environmental factors (EEF). GF are those whose variations control aquifer heterogeneity; for each model family, the choice of GF depends on its level of complexity (discussed later). EEFs for all families include: relative permeability model (RPM), residual gas saturation (RGS), reservoir temperature gradient (TG), ratio of vertical to lateral intrinsic permeability (VHR), and brine salinity (SAL) (Figure 3.11). These factors and their uncertainties are largely independent of aquifer heterogeneity and the geologic factors contributing to it. All EEF are included in the PB designs for all families. In the following sections, these factors and their uncertainties will be discussed in detail.

3.2 Data Collection and Interpretations

3.2.1 Geological Cross Section and Isopach Data

To construct a regional-scale geologic model, geological cross sections [57] [58] and three isopach maps of the Twin Creek Limestone, Nugget Sandstone, and Ankareh Formation [59] [60] [61] are collected. These data, along with formation markers from wells drilled at the study site (Figure 1.1), are used to interpret a regional Nugget Sandstone structure including formation contacts.

3.2.2 Geophysical Well Logs

Fourteen wells are used during the geologic modeling process. Among them, 8 wells (API:2320053, 2320230, 2320231, 2320402, 2320461, 2320647, 2321634, 2321669) are located at the model site. Unfortunately, core measurements are not available for these wells. Therefore, 6 wells (3720422, 4120147, 4120148, 4120178, 4120643, 4120656) with abundant core measurement data from neighboring regions are incorporated into our database to calibrate the calculated porosity from wireline log signals to the core measured porosity (these data are referred to as "well log porosity" and "core porosity" hereafter, respectively). The underlying rationale is that core porosity is treated as more accurate, although detailed petrographical studies are needed to clarify the discrepancy between core and log porosities [62]. However, image logs (e.g., Formation MicroImager) and detailed core description are not available at the study site. The core porosities are also used for developing facies coding and permeability(k)-porosity(ϕ) semilog transforms. Five out of these 6 wells are located at the production fields to the west of the Absaroka Thrust fault (Figure 1.1). Although the Nugget Sandstone in that area is a prolific gas and condensate producer [63], in our study region, it is a deep, inclined saline aquifer with limited and frequently incomplete data.

At the study site and nearby regions, each well on average has 4~5 raster geophysical well logs (e.g., Density, Gamma Ray, Sonic, Neutron). All of these logs have been digitized and used for petrophysical calculation and facies coding with Interactive Petrophysics 3.6. For the 6 wells with both well logs and core measurements, data from both sources are plotted together. For quality assurance, porosity data are aligned together for depth shift and checking correlation. One example of well plot (API: 4120147) is shown in Figure 3.1. Formulaes used here for calculating the porosity from well log signals are : $\Phi_D = (\rho_m - \rho_b) / (\rho_m - \rho_f)$, $\Phi_{Cal} = (\Phi_D + \Phi_N) / 2$. Φ_D is density log derived porosity, Φ_N is porosity from neutron porosity logs, ρ_m is matrix/grain density, ρ_b is bulk density log, and ρ_f is fluid density. Next the calculated porosity values are plotted against the core porosity measurements at the same depth (Figure 3.2). The fitted transform is used to calibrate well log derived porosity of the 8 wells at the study site without core measurements (Figure 1.1). Although the correlation between core measured porosity and well log derived porosity is not very good, a single transform is adopted here to simplify the study. For facies coding, fuzzy logic implemented within Interactive Petrophysics could be used if detailed core descriptions are available [64] [65]. Since such data are not available, facies coding is implemented using petrophysical properties cutoffs (details will be discussed later in facies descriptions). Finally, the well log data were also interpreted to obtain estimates, if available, of formation fluid type, saturation content, and temperature. Well log data (e.g., spontaneous potential and resistivity logs

TABLE 3.1: List of Nugget Sandstone core data collected.

Township	Range	Field	Well API
39N	113W	Wildcat	3920018
39N	114W	Game Hill	3920032
39N	117W	Wildcat	3920028
27N	113W	Hogsback	3505128
27N	114W	Dry Piney	3520218
26N	95W	Wildcat	3721098
24N	120W	Wildcat	2320226
19N	119W	Whitney Canyon-Carter Creek	2320224
18N	118W	Wildcat	4120118
18N	118W	Wildcat	4120236
17N	119W	Wildcat	4120065
17N	119W	Ryckman Creek	4120078
16N	119W	Painter	4120362
16N	119W	Painter	4120178
16N	119W	Painter	4120148
15N	119W	Painter	4120135
15N	119W	Painter	4120112
15N	120W	Painter	4120147
15N	120W	Painter	4120360
15N	120W	Painter	4120359
13N	121W	Wildcat	4120640
13N	121W	Anschutz Ranch East	4120656
13N	121W	Anschutz Ranch East	4120643
13N	120W	Bessie Bottom	4120477

) and well production records for the Nugget Sandstone indicate that at most of the study site, in-situ formation fluid is predominantly NaCl-type brine [5]. For some wells, temperature measurements also exist. These data were used to provide estimates of average formation temperature and vertical temperature gradient, based on which an initial temperature field was assigned to the CO₂ simulation model.

3.2.3 Petrophysical Data

Limited core-based petrophysical data are available in the surrounding regions of the study site [66], and some of those cores' locations are shown in Figure 1.1. Well-log calculated porosity and permeability were calibrated against core measurements at the same well to obtain log-linear correlation functions. Fractures are seen in some cores [66] [67]. A complete list of the core data collected from the neighboring regions is shown in Table 3.1.

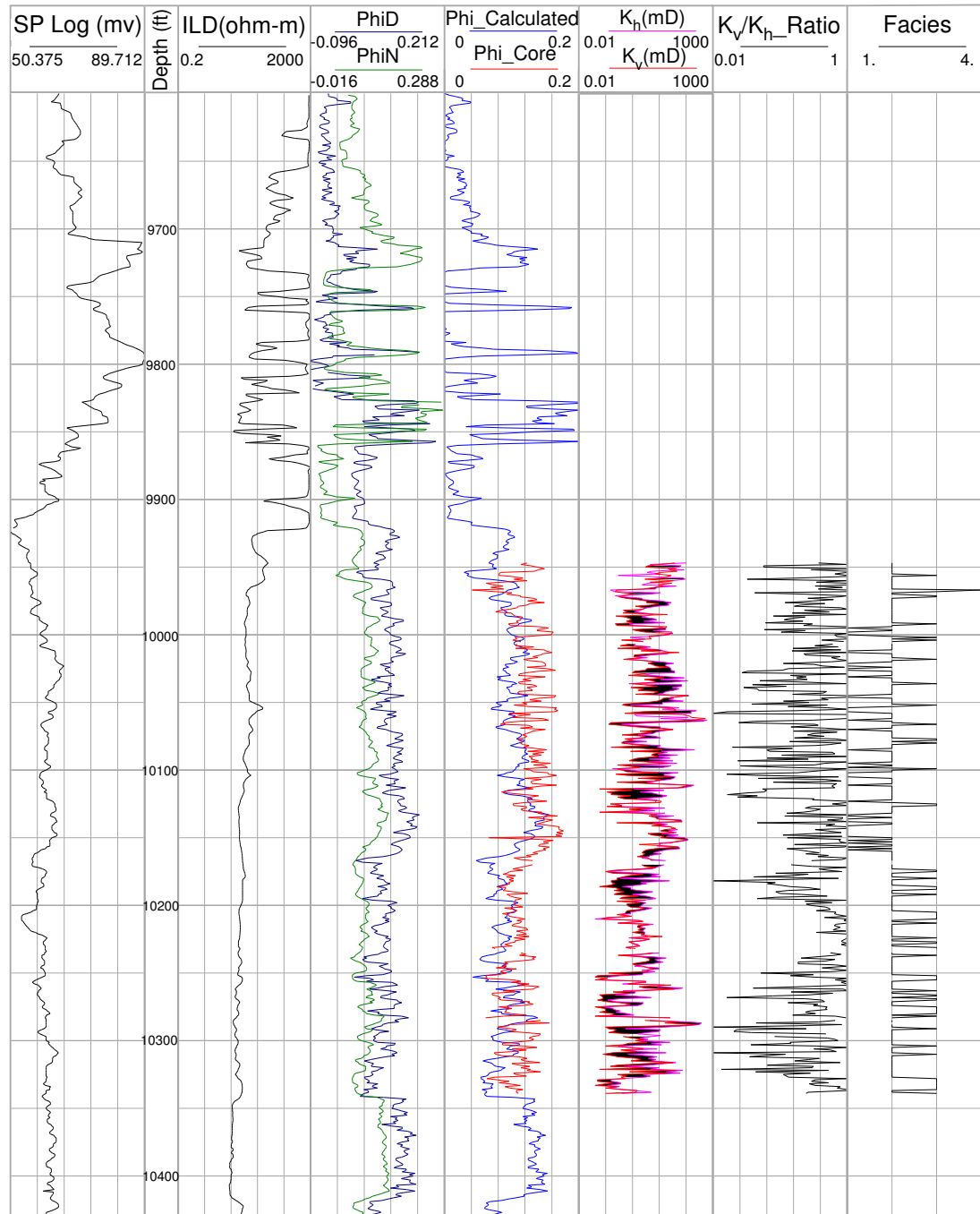


FIGURE 3.1: Log plot of well 4120147. Phi: Φ ; PhiD: Φ_D ; PhiN: Φ_N ; ILD: deep resistivity log; SP: spontaneous potential log. In this well, core porosity measurements (Phi_Core) have been shifted in depth to be consistent with the calculated well log porosities (Phi_Calculated), since depth information of core measurements can be inaccurate because of the missing interval of core samples.

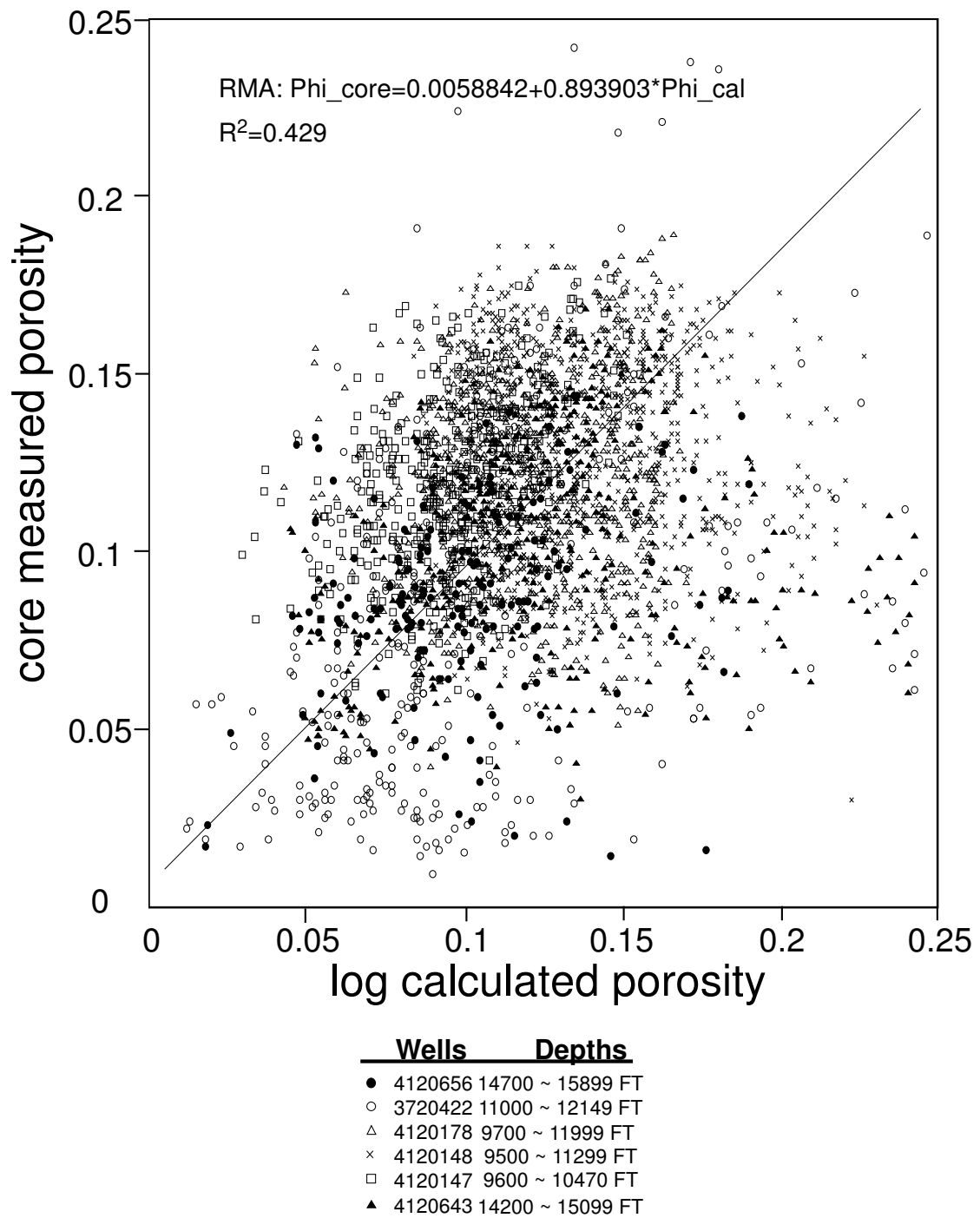


FIGURE 3.2: Log calculated porosity versus core measured porosity. The transform suggests that the core porosities are on average 92% of the well log porosities, indicating a slight bias in the well log calculated porosities, which may be attributed to different measurement support or difference between effective porosity (core measured porosity) and total porosity (well log calculated porosity).

3.2.4 Engineering Data

Relative permeability is of significant interest when it comes to multiphase flow simulation. As discussed in the previous review section, relative permeability of CO₂ has a remarkable effect on gas flow, mobility, and residual trapping in a CO₂-brine system. To simulate CO₂ storage in the Nugget Sandstone, the gas-phase relative permeability, its hysteresis function, and its endpoint saturations are selected from core flooding experiments on sandstone cores [68] [2]. Capillary pressure function, measured on similar cores, is also obtained [69].

3.2.5 Uncertainty in the Data

Various sources of uncertainty are commonly present during the geologic modeling and flow simulation process. In this study, selected uncertainty factors are investigated, and their uncertainty ranges varied in the DoE analysis are discussed in the following:

(1) From the core data analyzed in other studies [63] [70], the upper part of the Nugget Sandstone represented in the cores studied is comprised of stacked dune and mostly dry interdune deposits (good reservoir quality), while the lower part are mostly dry-to-damp interdune deposits (poor reservoir quality). However, because of varied amounts of erosion associated with the post-Jurassic unconformity, the more porous and higher permeability stratigraphic interval is not necessarily always located at the top of the formation. Therefore, this uncertainty is incorporated in building different geologic model families.

(2) Previous studies and core measurement data of the Nugget Sandstone both indicate the existence of fractures [66] [67]. However, the existence of fractures in situ cannot be ascertained, since there are no core descriptions available. Image logs, e.g., Formation MicroImager, would be needed to distinguish between diagenesis generated and drilling induced fractures. In the Overthrust Belt, at the Anschutz Ranch East Field and the Painter Field, the Nugget Sandstone is observed to have experienced significant structural diagenesis overprint. Here, core analyses suggest that primary Nugget Sandstone ϕ and k (as controlled by depositional processes) have been modified by compaction, cementation, dissolution, quartz overgrowths, molds, grain-coating, and the formation of pore-bridging illite [71] [70] [72]. Both open and gouge-filled fractures are observed, with widely varying strike orientations, whereas fracture dip is dominated by high angles approaching vertical [71] [73]. Similar structural diagenesis overprints are observed in the Frontier Sandstone in north-central Wyoming at 6.3 km depth [74]. However, in-situ subsurface stress conditions at the study site may differ from those observed in the

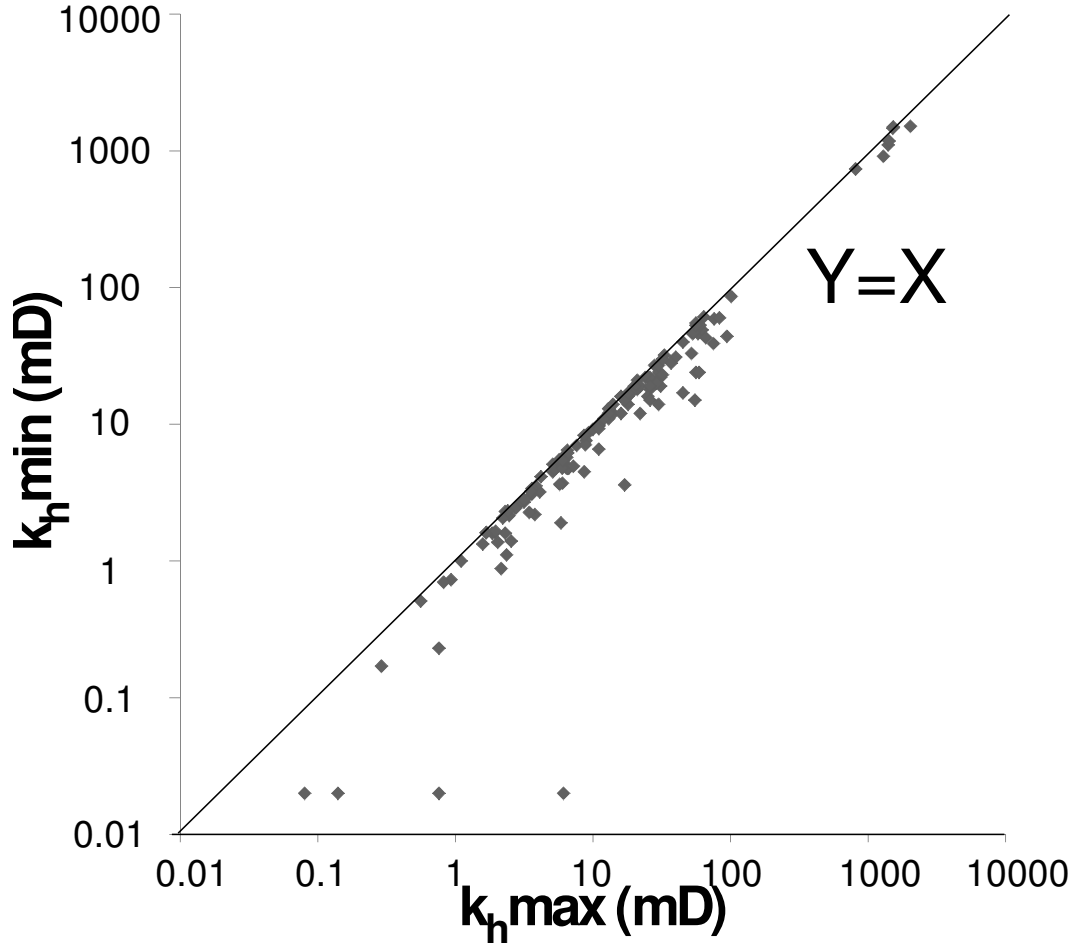
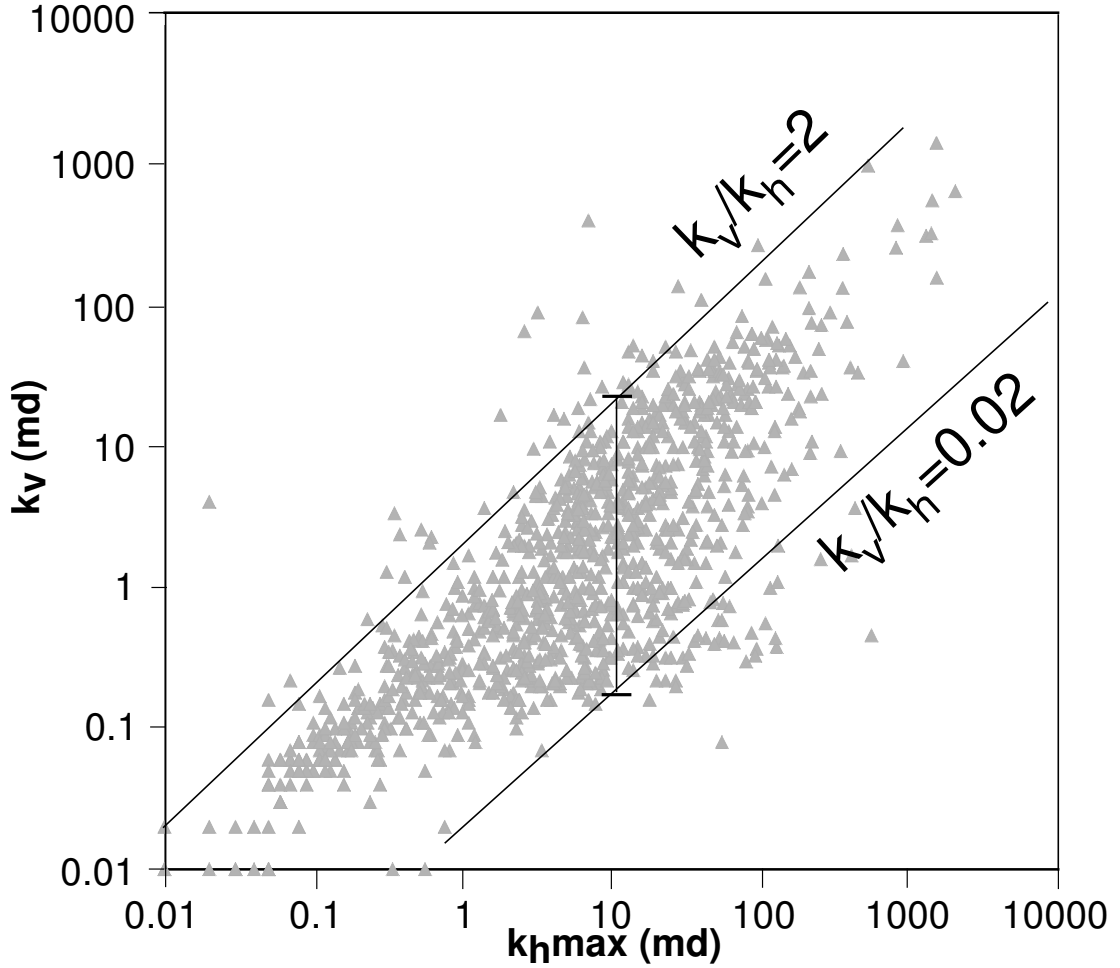


FIGURE 3.3: k_h max and k_h min from available Nugget Sandstone core measurements

neighboring regions. Fractures can become important to fluid flow when their density is high, either forming an interconnected network as fluid barriers or pathways depending on how connected and how open they are. Also, fracture-induced enhanced vertical permeability and reduced horizontal permeability can affect gas migration. Therefore, this uncertainty is accounted for in building the geologic model, which is then propagated into gas injection simulations. According to the core measurements, while the horizontal directional permeability is mostly isotropic (Figure 3.3), the ratio of vertical to horizontal permeability (k_v/k_h) exhibits a large range of variation (Figure 3.4), suggesting the existence of both open and closed (or no) fractures. In the DoE uncertainty analysis, for k_v/k_h , if facies difference is not taken into consideration, the +1 case is set to 2, while the -1 case is set to 0.02. The +1 case could be explained by high-angle open fractures; -1 case may correspond to matrix anisotropy, cores with sealed fractures [75], or other mechanisms, e.g., cross bedding, cementation, deformation bands [76] [77]. End members of k_v/k_h for different facies are introduced later in the facies descriptions section.

FIGURE 3.4: k_v and k_h from available Nugget Sandstone core measurements

(3) Studies indicate that a porosity-depth trend commonly exists in formations that extend over large depth intervals. Porosity generally decreases with increasing depth of burial [1] [70] [78]. A possible reason for this could be the growth of orthochemical quartz, which forms overgrowths around detrital quartz grains and fills the pore spaces between them. Core measurements of the Nugget Sandstone in the neighboring regions at different depths and the measurements of the equivalent Weber Sandstone are integrated to investigate a possible porosity-depth trend in-situ. After collecting all the data, a possible porosity-depth trend is identified (Figure 3.5). However, due to subsurface complexity and variations in diagenetic effects, this trend is not strong compared to those observed elsewhere.

(4) During formation structure modeling, in regions with sparse data control, formation thickness interpolation was used. However, we did not examine this uncertainty source in the later sensitivity analysis.

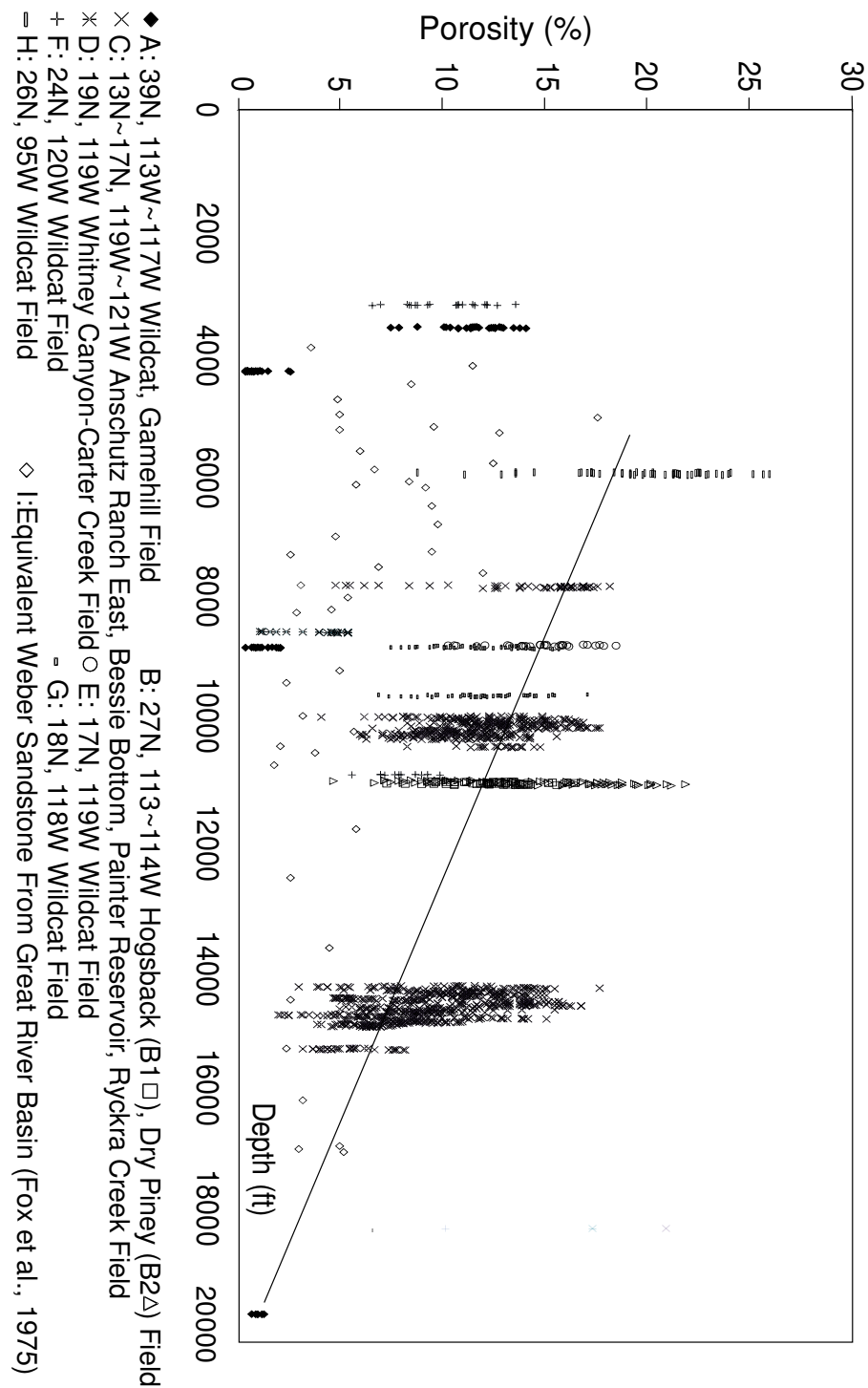


FIGURE 3.5: Porosity distribution with depth, compiled from Nugget Sandstone core measurements from the neighboring regions. A possible depth trend is fitted and used for soft conditioning.

(5) Paleocurrent studies suggest that the facies of Nugget Sandstone are often aligned northeast, ranging from N20E to N70E [79]. At the Overthrust Belt, however, the in-situ azimuth of the Nugget Sandstone facies is uncertain, which will be accounted for in the sensitivity analysis by varying this angle from N5E to E5S.

(6) The lateral extent of various depositional facies of Nugget Sandstone is uncertain. End members are defined based on those observed for the Navajo Sandstone, a Nugget Sandstone equivalent in Utah [80]: The +1 case is set to 10,000 m (32,800 ft) while -1 case is set to 100 m (328 ft).

(7) k_h can be populated from ϕ with a log-linear transform [32] [5]. However, data of the Nugget Sandstone are quite scattered (Figure 3.6). To minimize bias in fitting a single transform to averaged reservoir quality rocks, end member transforms are first fitted to all scattered data (Figure 3.6; left). These transforms are used to populate k_h from Φ of the Nugget Sandstone, without distinguishing the rock type (i.e., good versus poor reservoir quality rocks). However, the porosity-permeability relationship can be different for different facies. Two major “rock type” populations of the Nugget Sandstone were first proposed by Stan Kolodzie from porosity and water saturation crossplots of log-derived data [63]. The first population (rock type 2) is a series of low-angle stratifications associated with wet interdunes (corresponding to petrofacies 4) and low-relief sand sheets (corresponding to petrofacies 3) (Figure 3.6; right). The second population (rock type 1) consists of dune grainfall (corresponding to petrofacies 1) and cross-bedded wind-ripple deposits not affected by water presence (corresponding to petrofacies 2). Accordingly, two sets of end member transforms are defined from the same scattered data (Figure 3.6, right). Details on categorizing 4 petrofacies are described later in the facies description section.

(8) Since Nugget Sandstone relative permeability measurements are not available, three different relative permeability models are chosen from [2] and are ranked by their water saturation and relative permeability end points during the drainage period. The +1 end member is Cardium Sandstone, while the -1 end member is Berea Sandstone (Figure 3.7). In the Cardium Sandstone, CO₂ can flow at nearly 3 times the speed as in the Berea Sandstone, due to its high end-point relative permeability.

(9) End member temperature gradient is inferred from available temperature logs of wells perforating the shallower Nugget Sandstone (Figure 3.8). Given the depth range of the model ($\sim 7,000$ ft above sea-level to $\sim 12,000$ ft below sea-level), the end members

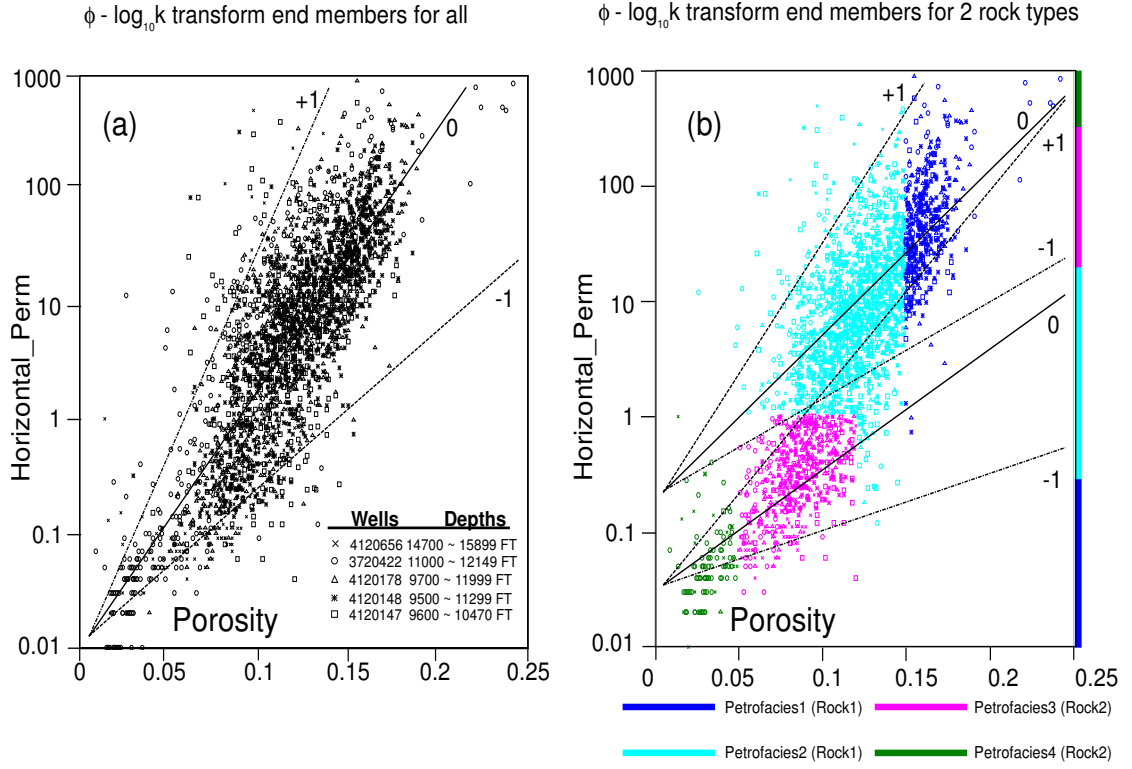


FIGURE 3.6: Based on core measurements, end members of k_h - Φ transform are developed for a single Nugget Sandstone without facies distinction (a) and for two dominant rock types (b).

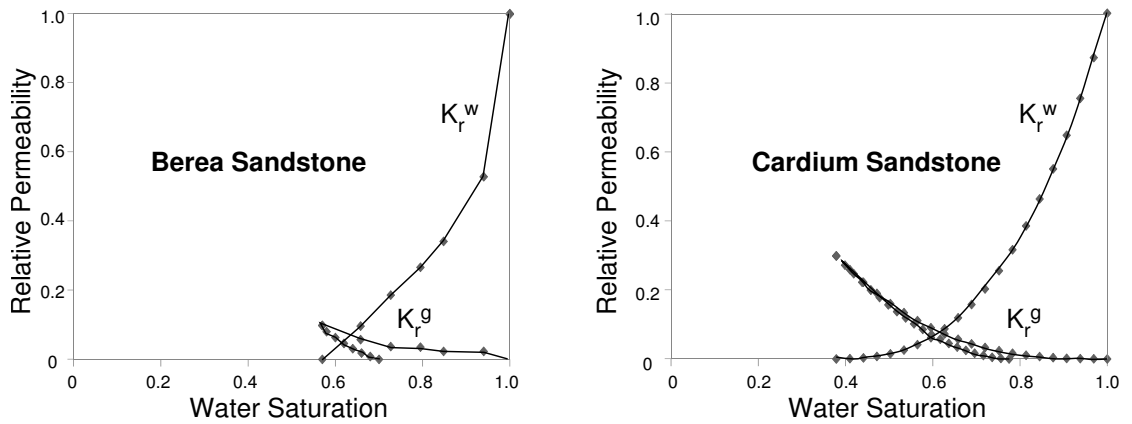


FIGURE 3.7: Relative permeability model of end member sandstones. Berea Sandstone represents the -1 case while Cardium Sandstone stands for the +1 case [2].

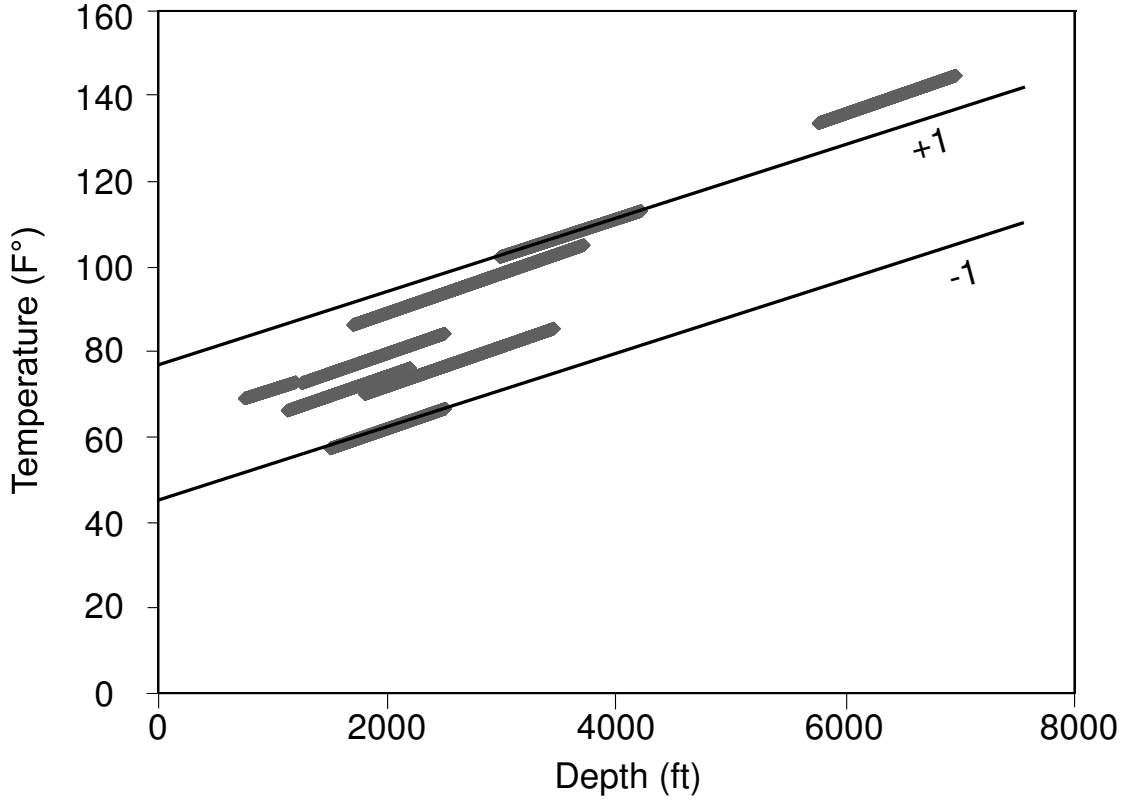


FIGURE 3.8: Temperature versus depth measurements from the temperature logs. Two possible temperature-depth gradients are fitted.

generate either a cool or a warm formation, which will impact gas density, gravity effect, and therefore gas migration.

(10) Total dissolved solids (TDS) in the Nugget Sandstone brine ranges from 10,000 to 115,000 ppm [5]. To investigate the impact of salinity on GCS, the -1 case of TDS is set to 10,000 ppm, while +1 case of TDS is set to 100,000 ppm. Ideally, salinity initialization in the model would be performed on a cell-by-cell basis, given the depth range of our model. However, this is not an option in the simulator we used. There are other simulation modules available, but they have limitations as well. Reasons of choosing the current simulator will be discussed in section 3.4.

3.3 Static Reservoir Modeling

3.3.1 Nugget Sandstone Reservoir Description

The Jurassic eolian Nugget Sandstone in the Overthrust Belts of southwest Wyoming and northeast Utah is a textually heterogeneous formation with anisotropic reservoir

properties inherited primarily from the depositional environment. This extensive formation was deposited primarily by eolian processes in a coastal to inland sand sea or erg [81]. It extends from south-central and southwestern Wyoming to southeastern Idaho and northern Utah, increasing in thickness from east to west, from less than 100 ft to over 2,000 ft (30~600 m) [82]. The Nugget Sandstone are stratigraphically equivalent to the Navajo Sandstone of Colorado, Utah, and Arizona, and to the Aztec Sandstone of southern Nevada [82] [83]. Its original reservoir quality has been modified by diagenesis and overprinted by tectonism [63]. Two different stratification types are usually identified, for this formation, each with characteristic porosity, permeability, permeability directionality, and pore geometrical attributes. Dune deposits (good reservoir facies) primarily consist of avalanche deposits (grainfall or grainflow) and wind-ripple cross-strata. These high-permeability facies are commonly affected by local quartz and nodular carbonate cementation, chlorite precipitation, and minor framework and cement dissolution. Low-permeability, gouge-filled micro-faults and deformation bands are the predominant deformational overprint. Fractures are more likely to reduce horizontal permeability and possibly redirect fluid flow through the dune facies [70]. Interdune, sand-sheet, and other water-associated deposits (poor reservoir facies) are often characterized by low-angle wind-ripple laminae and more irregular bedding. Water-associated Nugget Sandstone stratification generally contains the finest grained depositional textures and has the poorest reservoir properties. These non-dune facies contain intergranular micritic carbonate and illite precipitates, which are most affected by compaction and pressure solution phenomena. Open vertical fractures are somewhat more likely in this lower permeability rock, providing local and intermittent effective permeability paths [71]. A high degree of heterogeneity results from variations in grain size, sorting, mineralogy, and thickness between cross strata. Porosity and permeability variations between facies and their arrangement in stacked vertical sequences result in stratigraphic layering of the reservoir. In the Nugget Sandstone, there appears directional permeability trends due to consistent Nugget Sandstone dune orientations, with the maximum permeability parallel to dune slipfaces. Average porosity in this formation is approximately 12% and permeability ranges from 0.1 to 1000 mD [5].

3.3.2 Nugget Sandstone Facies Characterization

In this study, dune and interdune were grouped into four depositional facies: Grainflow (GF), Cross-bedded Wind-ripple (CWR), Low-angle Wind-ripple laminae (LWR), and Water-associated Deposits (WD). In the model building process, four petrofacies were distinguished which correspond to these depositional facies types, as discussed below. In this study, when petrofacies are explicitly modeled (i.e., FAM2b, FAM3, and FAM4),

end-member k_v/k_h ratios will be developed separately, one set of end members for each petrofacies.

Grainflow (GF) facies (Petrofacies 1):

Nugget grainflow deposits are either visually distinct and even-textured, or more visually indistinct and uneven in appearance [63]. The even-textured, distinct bedding is interpreted to result from grainflow of non-cohesive dry sand. This type of stratification has looser packing, and thus higher porosity and permeability than the uneven, indistinct deposits. The porosity of distinct grainflow is normally higher than 15%. However, considering all of the Nugget grainflow strata present in the Thrust Belt producing trend, porosity ranges from approximately 5% to 25% (average 12~13%), and arithmetic average horizontal permeability ranges from several mD to hundreds of mD. Effective directional permeability ratios within amalgamated grainflow deposits approach 1.0, and the texture is more homogeneous than the wind-ripple deposits. Therefore, the +1 case of k_v/k_h ratio is set to 1 and -1 case is set to 0.2. In the Painter Field on the hanging wall of the Absaroka Thrust fault, the grainflow facies is the most abundant subfacies, comprising 45% of the Nugget Sandstone core examined and is most common in the upper two-thirds of the Nugget Sandstone, the averaged porosity of which is 14.5% [70]. This value is used as a cutoff during the petrofacies coding process "—" rocks with porosity higher than 14.5% are categorized as Petrofacies 1.

Wind-ripple facies (Petrofacies 2 & 3):

Wind-ripple deposits appear texturally heterogeneous in the photomicrograph, with porosity $\leq 12\%$ and directional whole-core permeability ranging from several mD to tens of mD in horizontal directions [63]. Meanwhile, vertical permeability is only hundredths of mD. Due to their inversely graded structure, this significant directional disparity is inherent in ripple-generated bedforms. Accordingly, wind-ripple facies is associated with the lowest k_v/k_h ratio observed in our core data. The +1 case of k_v/k_h ratio is thus set to be 0.2 and -1 case is set to 0.02. In the Thrust Belt producing trend, porosity in the Nugget Sandstone wind-ripple strata ranges from about 3% to 12% (average 7 ~ 8%), and arithmetic average horizontal permeability is commonly ≤ 1 mD (with a range from hundredths to tens of mD) [63]. It appears as cross-strata (CWR) in dune deposits and as low-angle laminae (LWR) in interdune/sandsheet deposits. Reservoir quality of CWR is usually better than LWR. The 1mD permeability value is used as a cutoff for differentiating CWR (Petrofacies 2, $k \geq 1$ mD) and LWR (Petrofacies 3, $k < 1$ mD) during the petrofacies coding process.

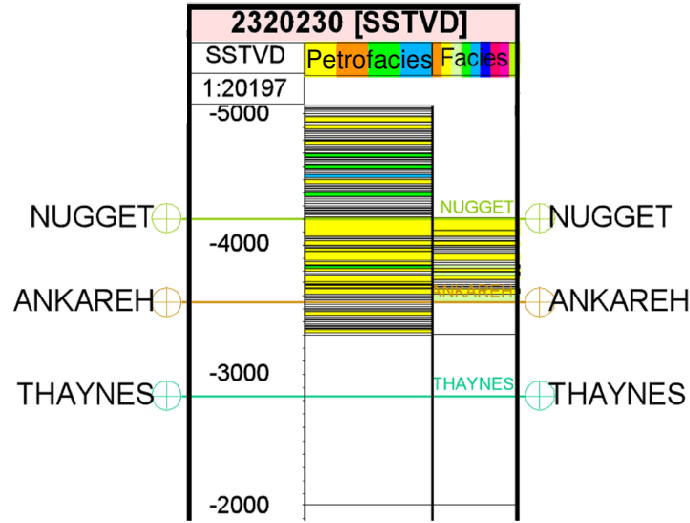


FIGURE 3.9: Facies coded by petrophysical values cutoff (petrofacies at left) and by neural networks (facies at right).

Water-associated Deposits (WD) (Petrofacies 4):

Water-associated Nugget Sandstone deposits generally have the poorest reservoir properties because of their finest grained depositional textures [70]. Porosity ranges from 2% to 9% (average 5 ~ 6%), and arithmetic average maximum k_h is several hundredths of an mD (ranging up to approximately 1 mD) [63]. The 5% porosity is used as a cutoff for distinguishing the WD facies during the petrofacies coding process. WD facies type has the highest k_v/k_h ratio because of bioturbation [63] [70], therefore the +1 case of k_v/k_h ratio is set to 2 and -1 case is set to 0.2.

Petrofacies defined by the above petrophysical cutoffs are very close to the result of automatic facies coding created using Neural Networks [5]. At well 2320230, results of these two different coding schemes are compared side-by-side (Figure 3.9), with similar outcomes in the grouping of the facies.

3.3.3 Family Models With Increasing Geologic Complexity

Optimal CO₂ geologic sequestration modeling hinges on obtaining a detailed understanding of reservoir complexity and on consolidating that information into whatever level of detail is appropriate for the scale of the problem being addressed. To build a very complex, highly detailed geological model requires great effort and is very time consuming.

In this study, based on subsets of the characterization data, a suite of increasingly complex geologic model families are built, extending from the ground surface to the footwall

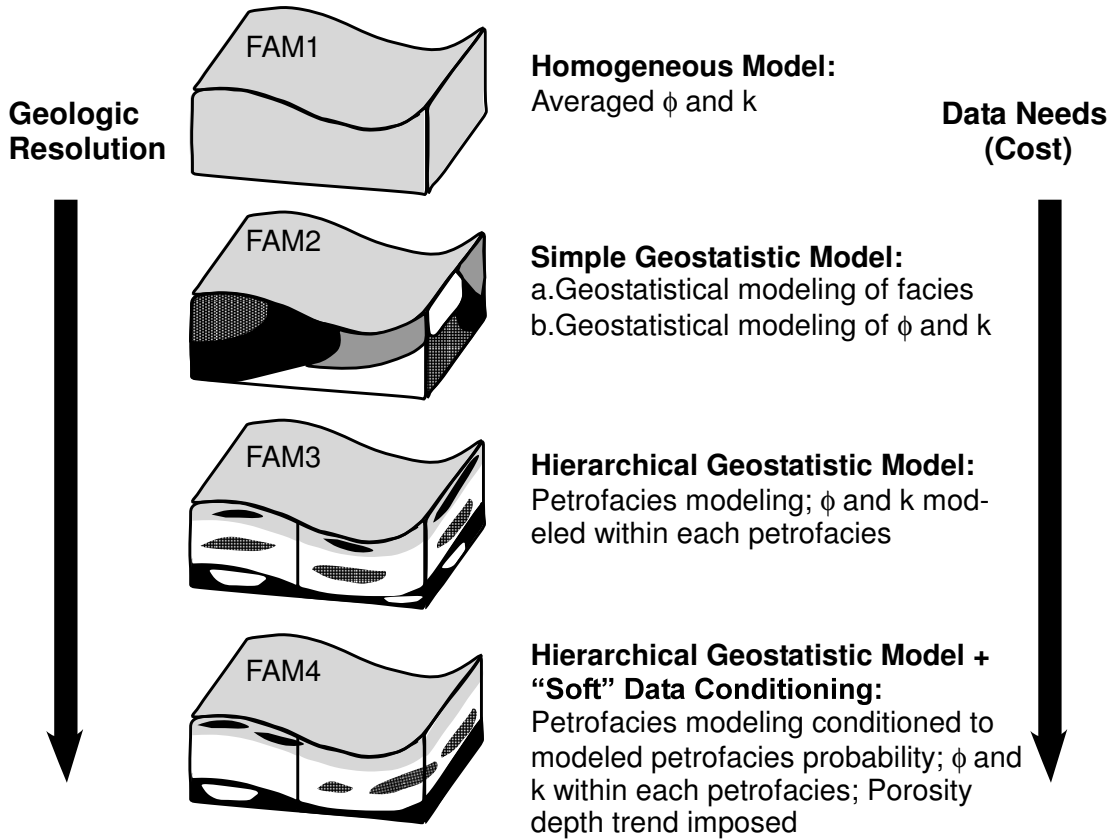


FIGURE 3.10: Schematic diagram of the 4 geologic modeling families

of the Absaroka Thrust: a homogeneous model (FAM1), a stationary geostatistical facies (FAM2a) and petrophysical (FAM2b) model, a stationary facies model with sub-facies petrophysical variability (FAM3), and a non-stationary facies model (with sub-facies variability) conditioned to both hard and soft data (FAM4) (Figure 3.10). These families, representing alternative conceptual models built with increasing data, share the same external geometry, grid, CO₂ injection design (e.g., well location, injection rate/duration, bottomhole pressure constraints), and boundary condition (BC). The families vary only in how aquifer heterogeneity is represented, as discussed below. In FAM1, only EEFs are varied due to the homogeneity assumption. Model building procedure for FAM2, FAM3, and FAM4 is dictated by the PB design and the number of FF increases in response to increasing model complexity (Figure 3.11).

3.3.4 Geologic Modeling Procedures

In this study, the most complex model (FAM4) is built first to determine the mean porosity and permeability for the simpler models (i.e., FAM1 and FAM2a). In this section, the model families are described in the order of decreasing model complexity.

<i>FAM ID</i>	GF in the PB Design	Ranges
3 & 4	Petrofacies correlation range (FCR)	100 to 10000 m (Hansen, 2007)
	Petrofacies correlation azimuth (FCA)	N5E to E5S
	ϕ - k transform (PPT)	See Fig. 3.6
2	ϕ correlation azimuth (PCA)	N5E to E5S
	ϕ correlation range (PCR)	Differs for each facies
1	Engineering/Environmental Factors	<i>See Table Below</i>

EEF	RPM	RGS	TG	VHR	SAL
- 1	See Fig. 3.7	0.2	See Fig. 3.8	See Fig. 3.4	10,000 ppm
+ 1	See Fig. 3.7	0.3	See Fig. 3.8	See Fig. 3.4	100,000 ppm

FIGURE 3.11: Factors varied in the PB design and their ranges of variation. Numbers indicate family ID. Engineering/Environmental factors are shared by all model families. Facies and ϕ correlation range and azimuth are of the horizontal direction. -1: minimum values; +1: maximum values.

The complete geological modeling workflow for building a FAM4 model is presented; the same procedure for building the other families models are not repeated.

3.3.4.1 FAM4 Models

To create the FAM4 models, these steps are followed: (1) creation of a structural framework; (2) creation of an appropriate simulation grids; (3) upscaling high-resolution well log Φ and facies data to the simulation grid; (4) geostatistical facies modeling (in the simulation grid) conditioned to soft data (facies probability cube); (5) facies-specific Φ and k modeling (Φ modeling is conditioned by a Φ -depth trend).

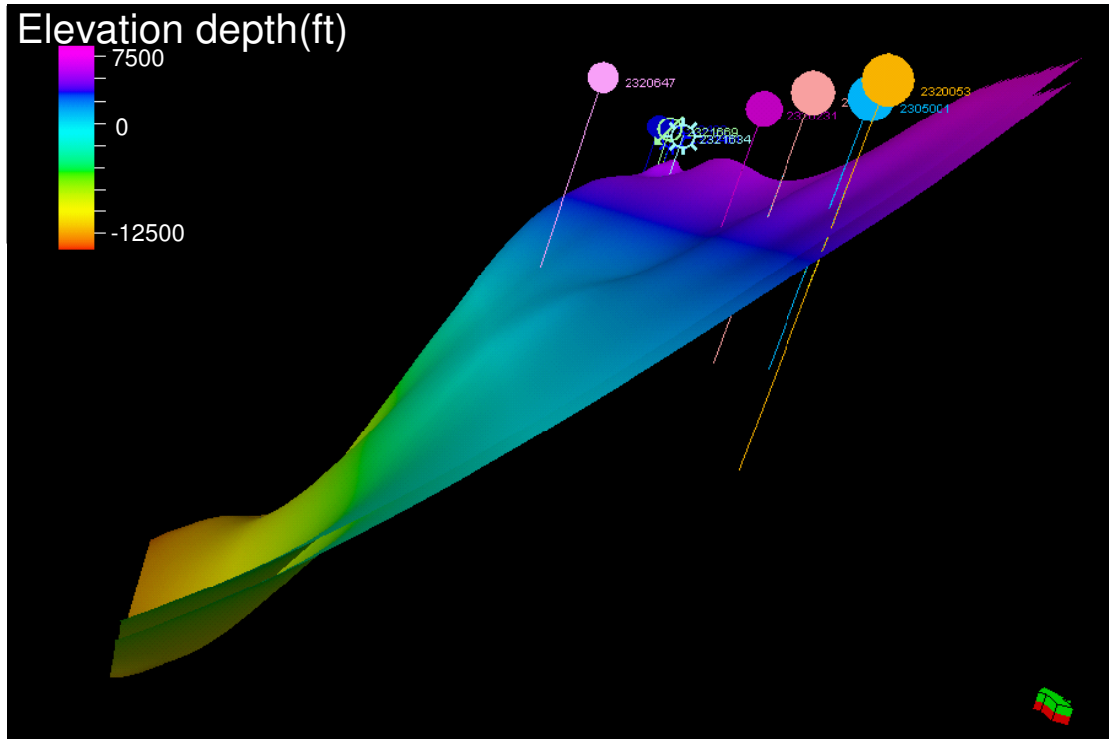


FIGURE 3.12: Regional structural model of the Nugget Sandstone. Depth is in feet at subsea level. Positive value is above sea level, while negative value is below sea level. Location of this model is indicated in Fig.1. Model uses 5x vertical exaggeration. The arrow points to the north.

Structural Framework Using the structural modeling tools in Petrel [84], well logs, cross sections, and isopach maps were integrated at the regional scale to create formation horizon correlations. Four horizons were interpreted, each representing a major contact between formations: top of the Twin Creek Limestone, top of the Nugget Sandstone, top of the Ankareh Shale, and bottom of the Ankareh Shale. The top of Nugget Sandstone and the top of Ankareh Shale are used to determine the structural framework of the Nugget Sandstone (Figure 3.12). Though faults may exist in the study region, the available data do not support detailed interpretations of their locations, thus faults are not modeled.

In interpreting the horizons, two points must be acknowledged: (1) in addition to the well logs, the horizons were constrained by geological cross sections and isopach maps. These maps were digitized first and many control-points were imported into Petrel to provide synthetic markers which were used, along with the digitized logs, to constrain the horizons; (2) in regions with sparse data control, formation thickness was interpolated, which allows physically correct extrapolation of the formation thickness throughout the modeled region.

Gridding By default, Petrel uses a corner grid technique for creating a model grid within the structural framework. To shorten simulation time, we aim to keep the number of grid cells within half a million. On the other hand, we still want to keep the number of grid cells in the vertical direction large enough so that the upscaling of well logs can still be accurate (discussed below). After a number of trials, a final model with 306,180 grid cells is used: NX=126; NY=162; NZ=15, NX, NY, and NZ are the number of grid cells in the x, y, and z direction, respectively.

Upscaling of Well Logs In general, wire-line logs are recorded in one-half foot intervals. However, flow simulation grids are typically much coarser, otherwise simulations may take inordinate amount of time to complete. The usual practice in industry (personal communication with BP geologic modeling team) is to build a fine geologic model with a grid vertical resolution of half a foot, and then use upscaling techniques to coarsen the fine grid to create a simulation grid with fewer cells. However, this process is not done in this study. A simulation grid is built directly from upscaling the well logs.

Using the majority vote method, a close match between the upscaled petrofacies histogram and the well logs petrofacies histogram was obtained (Figure 3.13), after a number of trials setting the grid cell vertical resolution. The proportion of each petrofacies is consistent with those observed for the Nugget Sandstone in previous studies [70].

Using the Arithmetic Average method and the neighbor cell choosing method (this averaging option will include log values from all cells adjacent to the upscaled cell which are at the same layer with the upscaled cell), a close match was obtained between the upscaled Φ histogram and the well logs Φ histogram (Figure 3.14).

Petrofacies Modeling After upscaling of the well logs, petrofacies modeling is conducted. In the DoE, two factors that control petrofacies population in the aquifer, i.e., horizontal facies correlation range (FCR) and azimuth (FCA), are varied in addition to the EEF which are shared with all the other model families. Facies horizontal correlation range uncertainty is determined based on the observation of the Navajo Sandstone, a Nugget equivalent in Utah [80]. Vertical correlation range is fitted from the vertical facies variogram model (Figure 3.15). Due to the sparsity of wells, horizontal variograms are often constructed with fewer lag distances, thus horizontal variogram modeling suffers greater uncertainty than vertical variogram modeling. As for the horizontal petrofacies azimuth, its uncertainty is based on those modeled for the Nugget Sandstone in the Moxa Arch region east of the study site [5]. In FAM4, petrofacies modeling is additionally constrained by a 3D petrofacies probability cube created from interpolating well

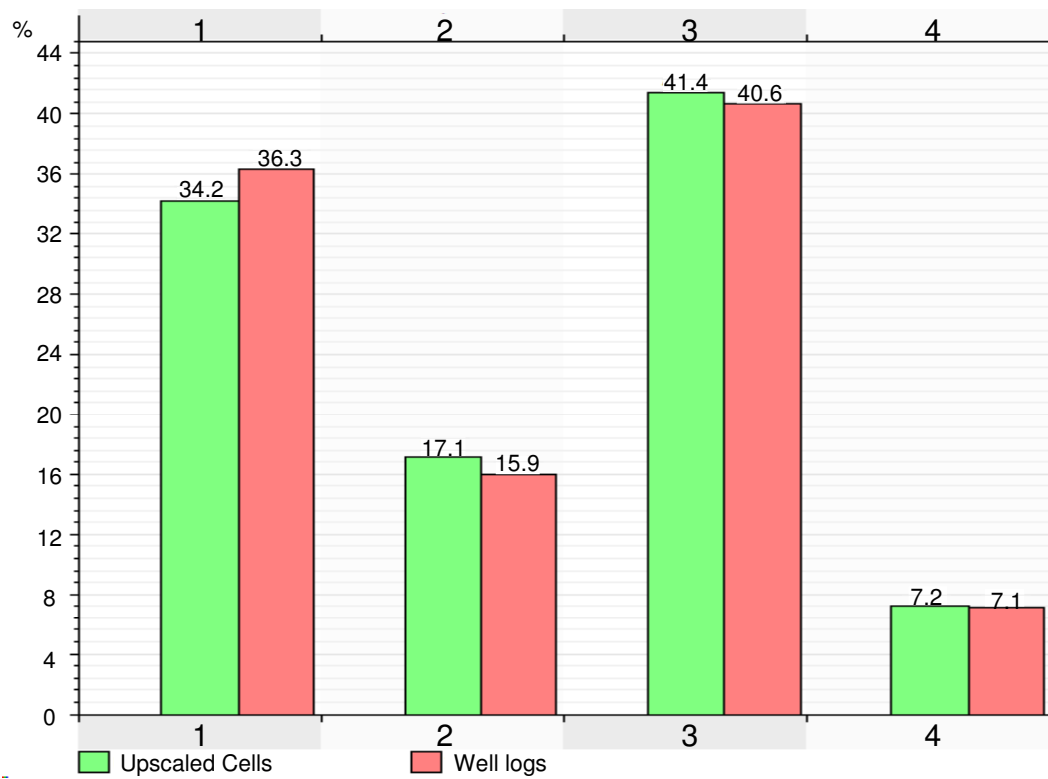


FIGURE 3.13: Histogram of petrofacies in the upscaled cells versus histogram of petrofacies in the well logs.

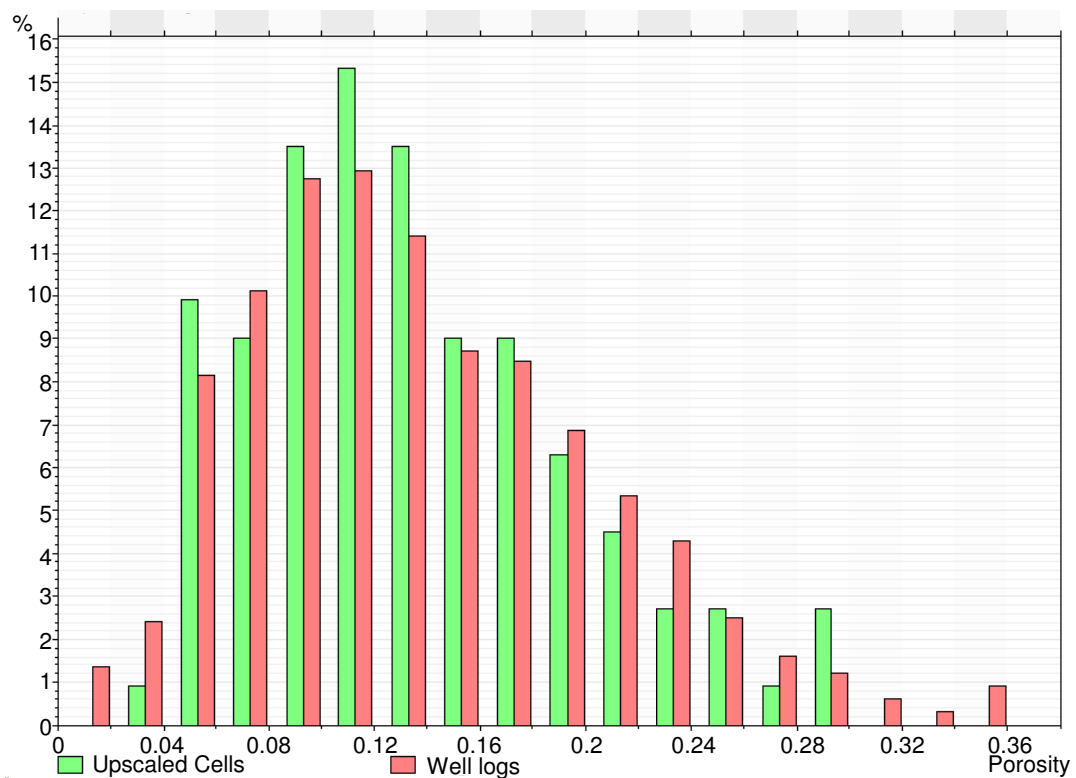


FIGURE 3.14: Histogram of porosity in the upscaled cells versus histogram of porosity in the well logs.

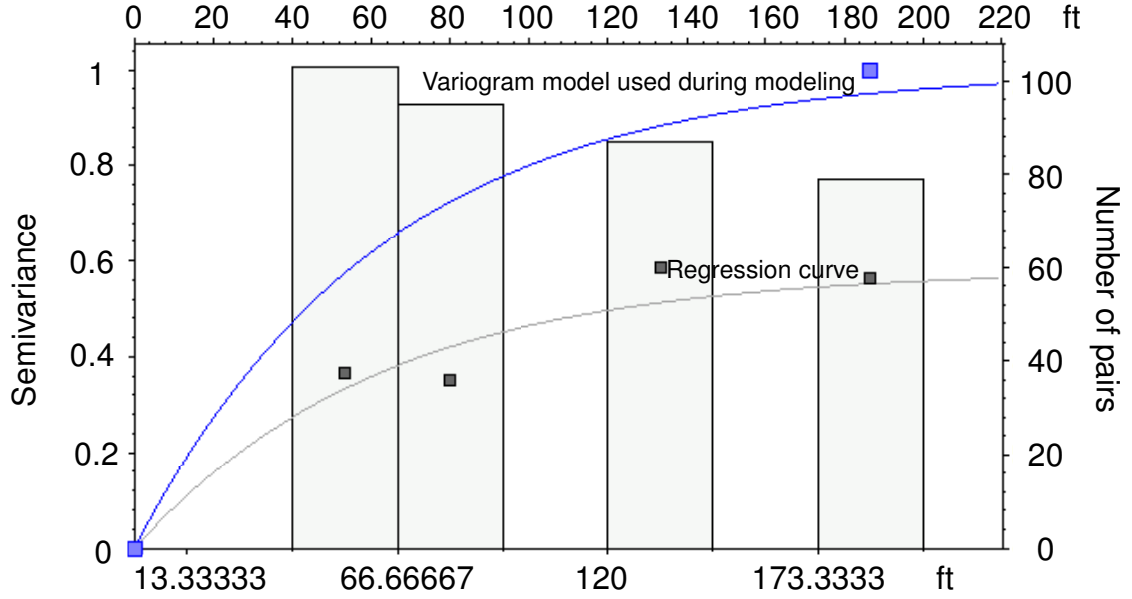


FIGURE 3.15: Experimental variogram and variogram model of vertical facies sequences. The gray curve represents the auto-fitted regression curve, and the blue curve stands for the variogram used during the modeling process.

data. The method of creating petrofacies probability models from well data and how it is used to condition petrofacies modeling is described in [85] [86] [84]. In this study, a global vertical petrofacies proportion curve (Figure 3.16) is first generated from all the 8 wells at the study site, since there are no data indicating a distinct transition of the depositional environment. In other words, there is no propensity zoning (also note that Nugget Sandstone is deposited in a sand sea). Petrofacies 1 and 2, which correspond to dune deposits, are most likely to occur in the upper Nugget Sandstone. Based on the upscaled petrofacies types at the 8 wells, probability of finding a particular facies for each model layer is determined by the proportion of that facies among all the facies at that layer (depth), then the probability values between the wells are interpolated using kriging (Figure 3.17). Combined with the global vertical petrofacies proportion curve, a 3D petrofacies probability cube is generated which is used to constrain geostatistical petrofacies modeling based on Sequential Indicator Simulation (SIS). A final petrofacies model for FAM4 is shown in Figure 3.18, corresponding to the center run of the PB design, i.e., all parameters assume their median values.

Petrophyscial Modeling The petrophysical modeling procedure follows 3 steps: (1) geostatistical ϕ modeling for each facies based on horizontal ϕ correlation range (PCR), horizontal ϕ azimuth (PCA), and soft conditioning data; (2) for each petrofacies, populating k_h from ϕ with a log-linear transform; (3) for each petrofacies, populating k_v from k_h using different k_v/k_h ratios.

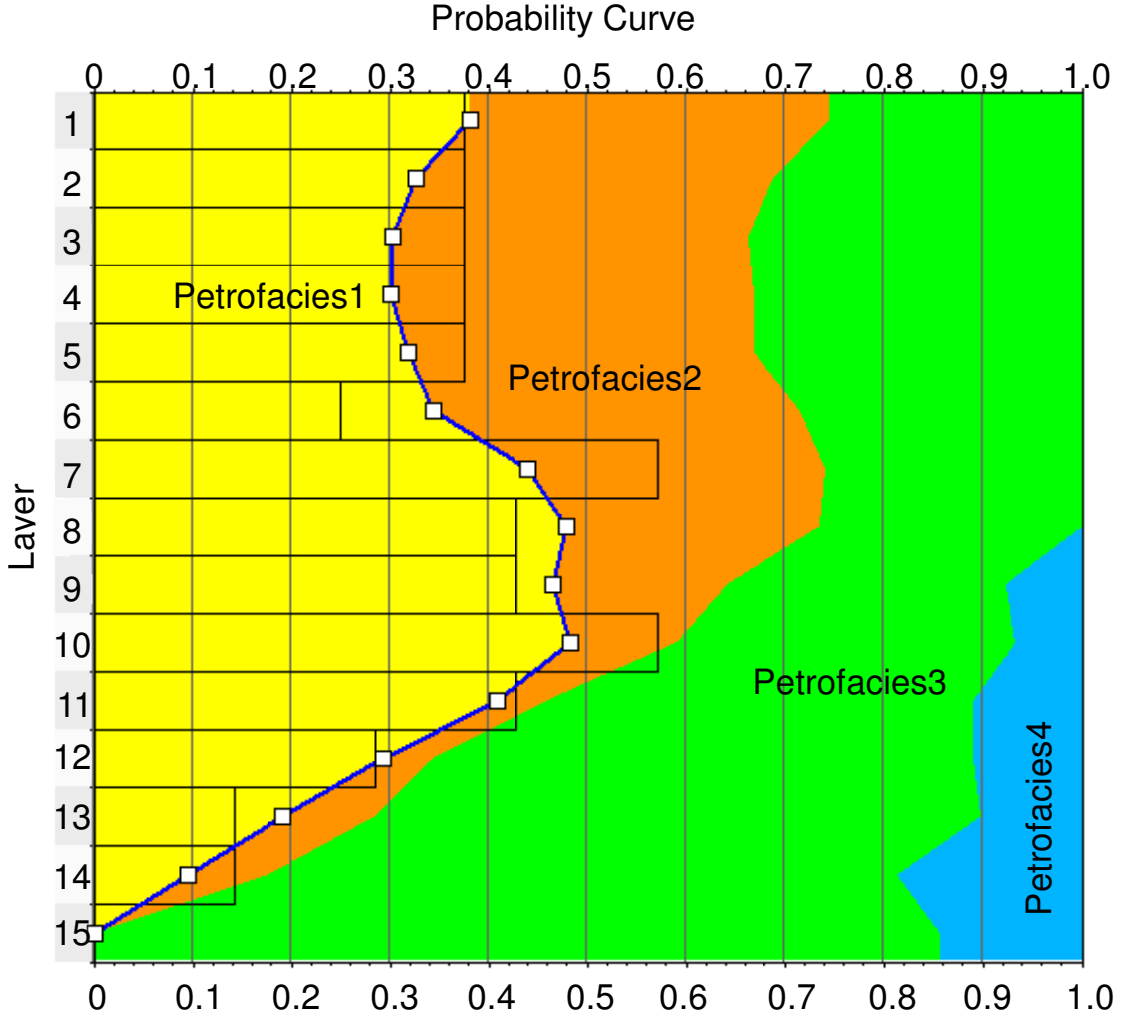


FIGURE 3.16: A global vertical petrofacies proportion curve generated from all the 8 wells at the study site.

For ϕ modeling in each petrofacies, the “0” case (median value) of PCR is determined by fitting a ϕ variogram model to the horizontal experimental variograms (Figure 3.19, first two columns). The +1 case is set to two times of the median PCR and the -1 case is set to half of the median PCR. Again, vertical correlation range is fitted and not varied since it has enough data of support (Figure 3.19, last column). In each petrofacies, porosity modeling is populated with Sequential Gaussian Simulation (SGS). In addition, during porosity modeling, a porosity-depth trend (Figure 3.5) is imposed to soft condition the data.

Next, horizontal permeability of each petrofacies is populated from ϕ with a log-linear transform (PPT). As discussed previously, the particular PPT transform is selected based on which of the two rock types the specific petrofacies belongs to (Figure 3.6, right). PPT is also varied in the DoE as a GF [87], minimizing bias in fitting a single transform to scattered data (Figure 3.6, right). Three PPT are developed for each rock

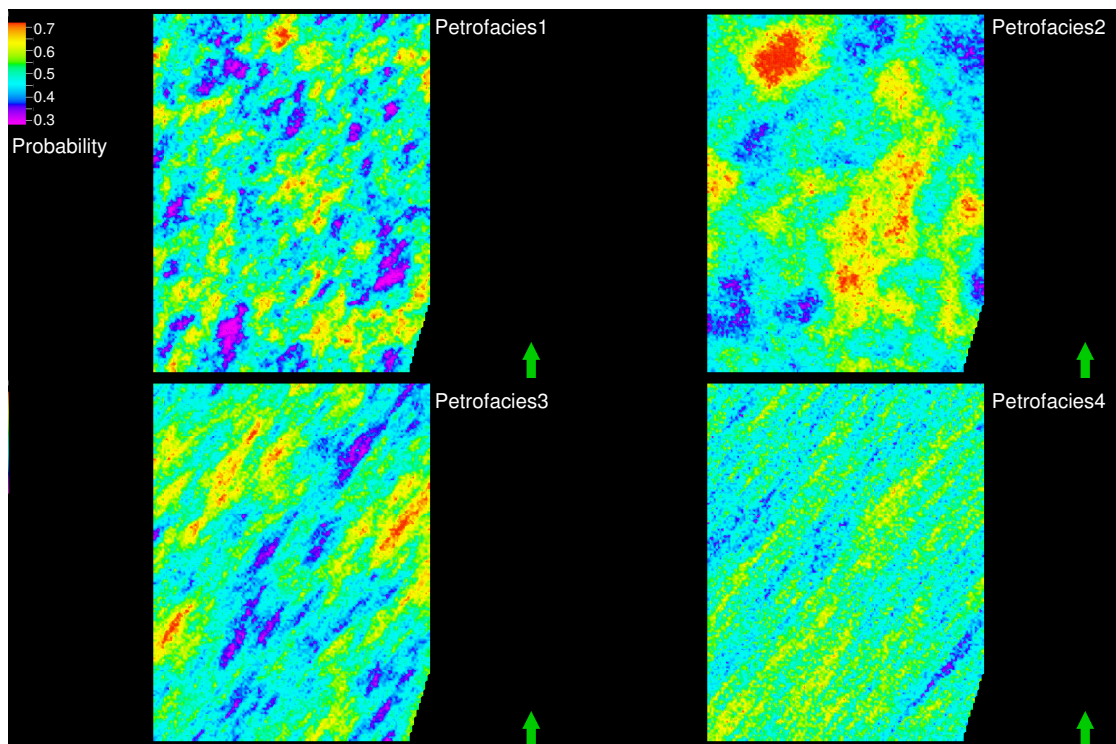


FIGURE 3.17: Lateral probability map for each petrofacies type. Arrow points North.

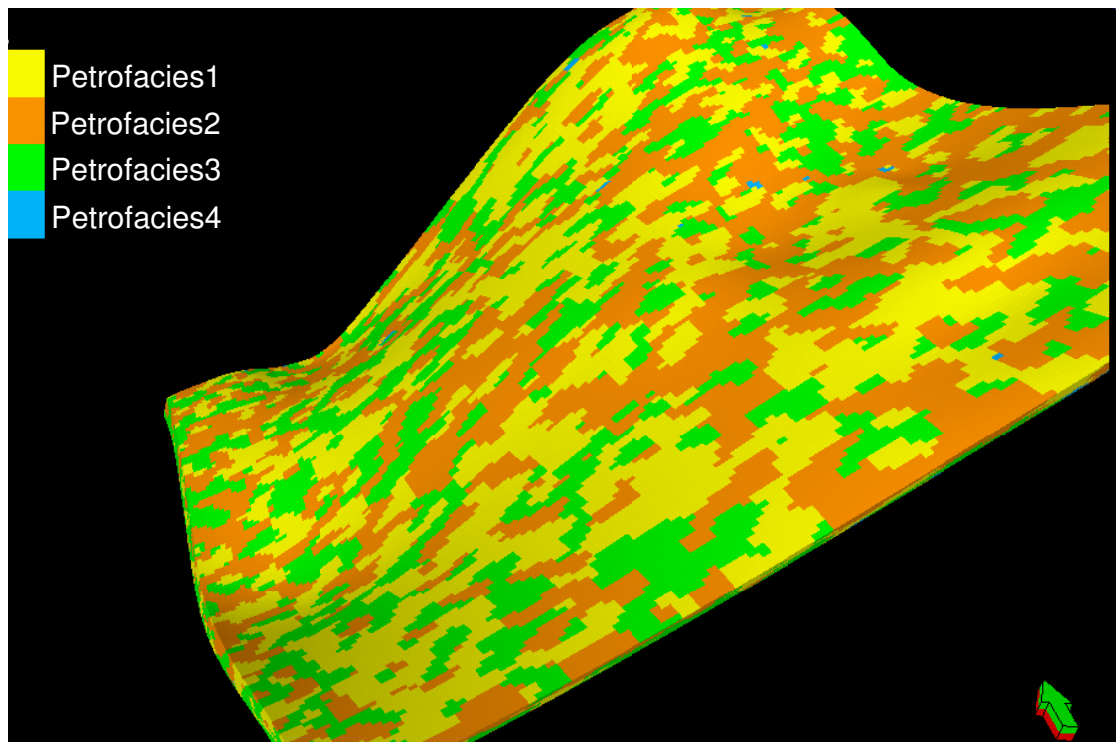


FIGURE 3.18: Petrofacies model corresponding to the center run of PB design. Arrow points North.

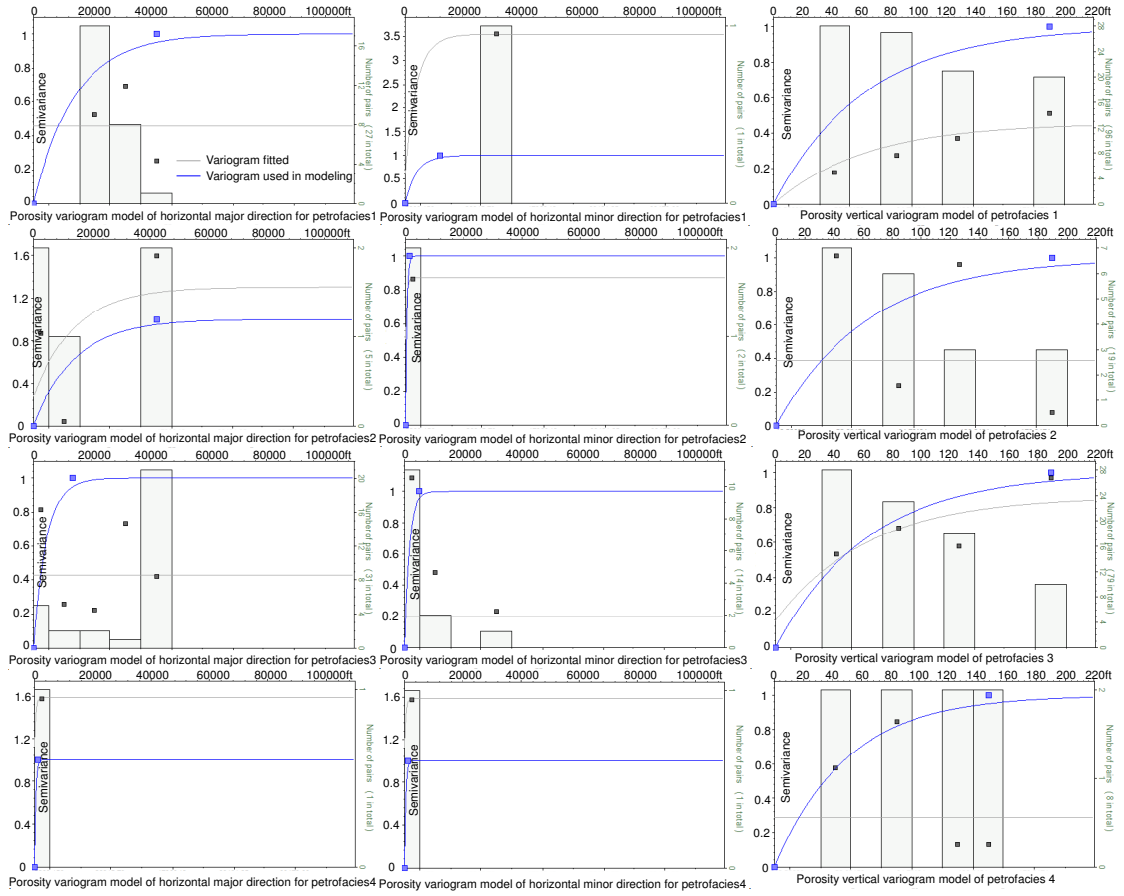


FIGURE 3.19: Experimental variograms and variogram models of ϕ for each petrofacies in three directions. The gray curve represents the auto-fitted regression curve, and the blue curve stands for the variogram used during the modeling process.

TABLE 3.2: k_v/k_h ratio end members for each petrofacies.

Petrofacies type	+1 case	0 case	-1 case
1	1	0.5	0.2
2	1	0.5	0.2
3	0.2	0.1	0.02
4	2	1	0.2

type; petrofacies 1 & 2 are associated with rock type 1, petrofacies 3 & 4 are associated with rock type 2. Table 3.2 summarizes the end member k_v/k_h ratios for each petrofacies (detailed discussion in the selection of each is provided in 3.3.2).

From the expected petrophysical distribution in FAM4 (i.e., center run of the PB design), average ϕ and the corresponding k_h can be calculated for each petrofacies (Table 3.3). These data reflect the mean petrophysical properties, and these values are consistent with those described in 3.3.2 for each corresponding depositional facies [63] [70]. These average values are assigned to each petrofacies in FAM2a.

TABLE 3.3: Average ϕ and k_h for each petrofacies, corresponding to the center run of the PB design.

Petrofacies type	Average ϕ	Average k_h
1	0.1926	382.91
2	0.1291	12.72
3	0.0915	0.33
4	0.05	0.10

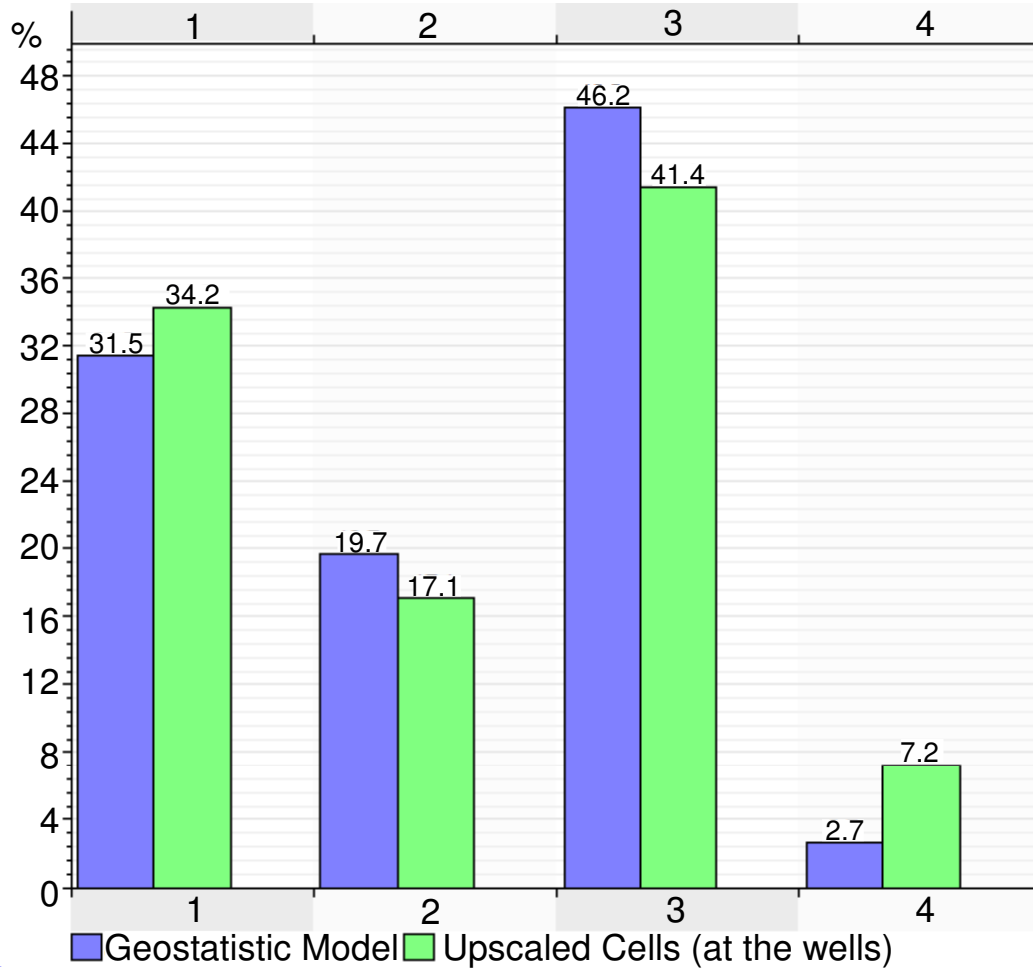


FIGURE 3.20: Petrofacies histogram of the geostatistical model plotted against that of the upscaled cells at the well locations.

Quality Check (QC) After geostatistical modeling of petrofacies and ϕ in the interwell region, QC is an essential step to make sure all input data and constraints are properly honored. For FAM4 models, four QC steps are conducted:

Petrofacies Proportion Petrofacies histogram of the model is plotted against that of the upscaled cells at the well locations (Figure 3.20). We can see that the proportions of each facies is well maintained, except for a somewhat lower estimate for petrofacies 4.

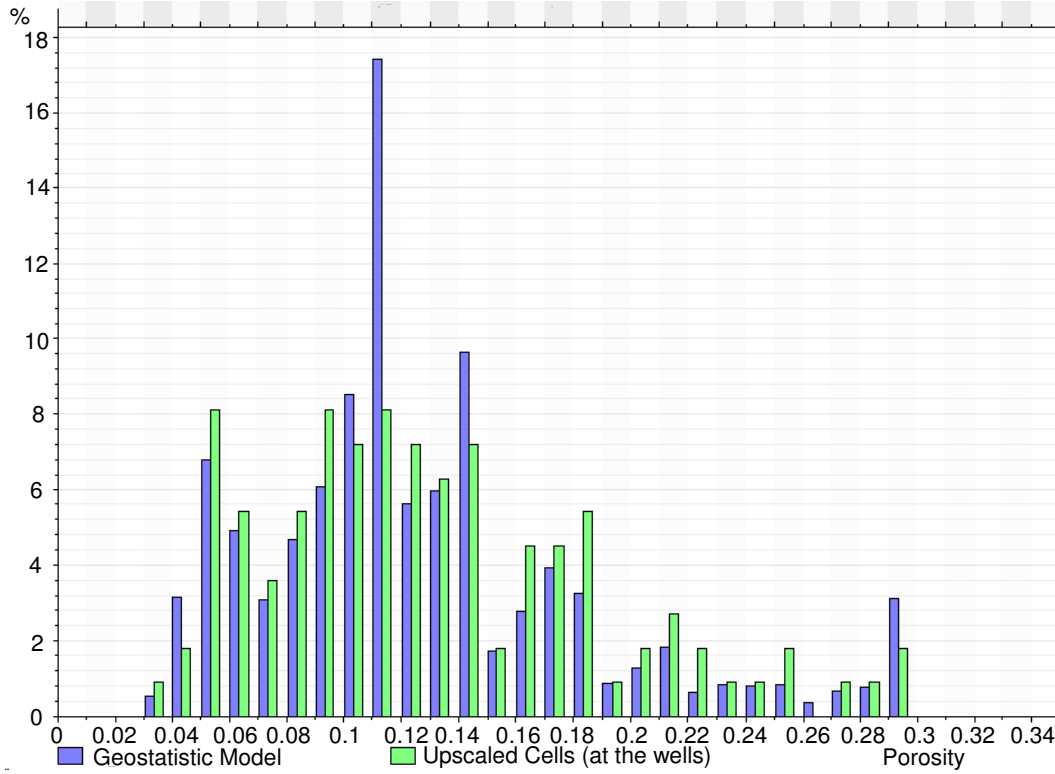


FIGURE 3.21: Porosity histogram of the geostatistic model plotted against that of the upscaled cells at the well locations.

Porosity Distribution To check whether porosity distribution is honored, a histogram of the geostatistic ϕ model is plotted against the input porosity histogram of the upscaled ϕ at the well locations (Figure 3.21). These two histograms are closely matched.

Petrofacies Model A cross section of the model is shown to determine if the petrofacies model is honoring the vertical proportion curve (Figure 3.22). Petrofacies 1 and 2 are mostly situated in the upper Nugget Sandstone, while petrofacies 4 is mostly located in the lower Nugget Sandstone. This is consistent with the specified vertical petrofacies proportion curve.

Porosity Depth Trend ϕ change with depth for each petrofacies is shown in Figure 3.23. In each petrofacies, porosity decreases with increasing depth. Thus, the porosity-depth trend is properly honored.

Uncertain Factors Varied In The PB design All uncertain factors considered for FAM4 are summarized in Figure 3.11. In addition, facies probability cube and a porosity-depth trend are imposed during the modeling process. These two factors,

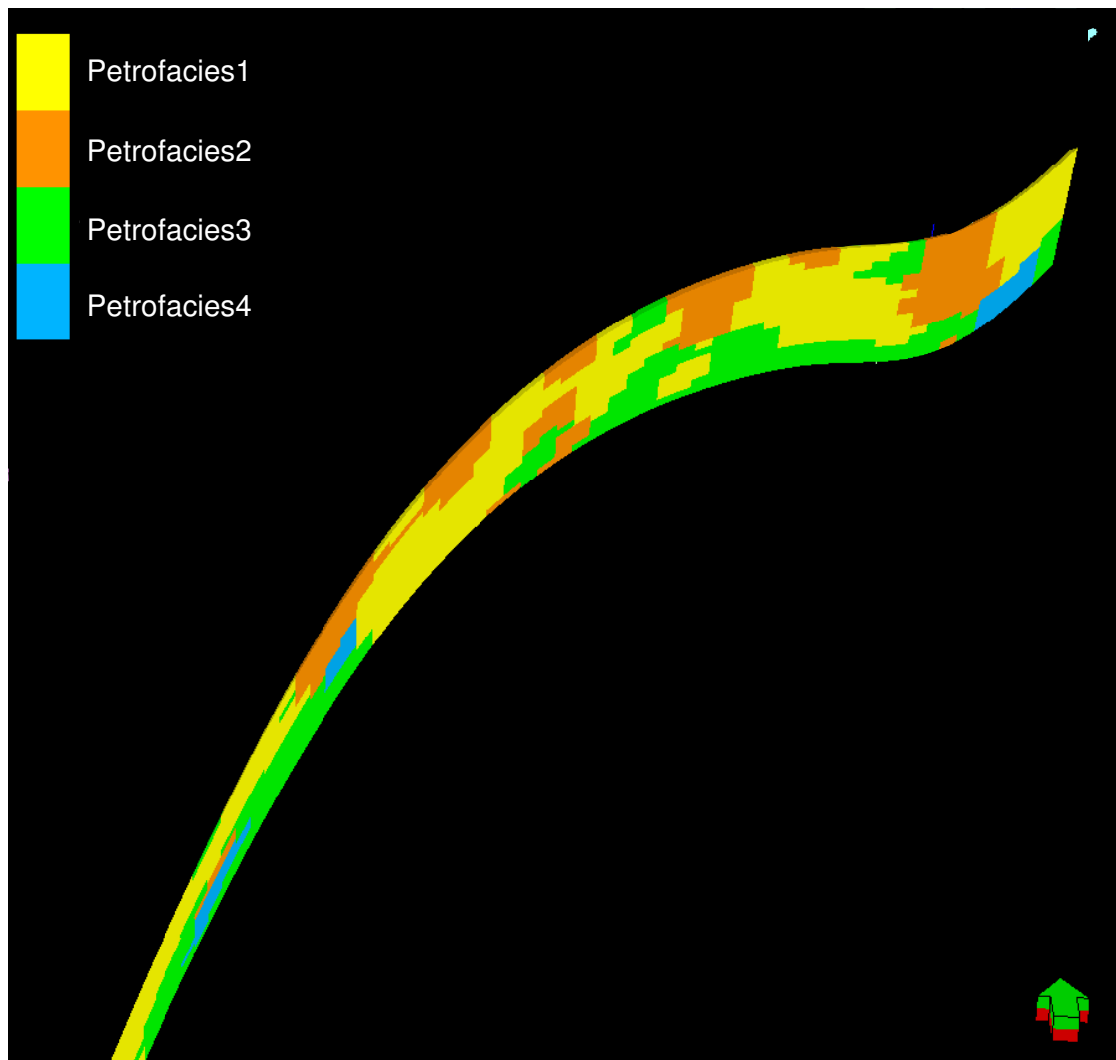


FIGURE 3.22: A petrofacies model cross section corresponding to the center run of the PB design. Arrow points north.

considered soft data, are incorporated into the model building process, but not in the PB design. Their impact is evaluated by comparing the outcomes of FAM4 with those of FAM3 (no conditioning). The PB design for FAM4 is shown in Table 3.4.

3.3.4.2 FAM3 Models

In FAM3, the modeling process is the identical to that of FAM4, except it doesn't incorporate soft conditioning data, i.e., the facies probability cube for facies modeling and the depth trend for porosity modeling. The PB design table for FAM3 is shown in Table 3.5.

TABLE 3.5: PB design for FAM3.

Runs	FCA	FCR	PCA	PCR	PPT	VHR	SAL	RGS	RPM	TG
Run 1	1	1	1	-1	1	-1	1	-1	-1	-1
Run 2	1	1	1	1	-1	1	-1	1	-1	-1
Run 3	1	-1	1	-1	1	-1	-1	-1	-1	1
Run 4	-1	-1	-1	-1	1	1	-1	-1	1	-1
Run 5	0	0	0	0	0	0	0	0	0	0
Run 6	-1	-1	1	-1	-1	1	1	1	1	-1
Run 7	-1	-1	1	1	1	1	-1	1	-1	1
Run 8	1	-1	-1	-1	-1	1	1	-1	-1	1
Run 9	-1	-1	-1	1	1	-1	-1	1	-1	-1
Run 10	1	1	-1	-1	1	-1	-1	1	1	1
Run 11	-1	1	-1	-1	1	1	1	1	-1	1
Run 12	-1	1	1	-1	-1	1	-1	-1	1	1
Run 13	1	1	-1	1	-1	1	-1	-1	-1	-1
Run 14	-1	1	-1	1	-1	-1	-1	-1	1	1
Run 15	1	-1	-1	1	1	1	1	-1	1	-1
Run 16	-1	-1	1	1	-1	-1	1	-1	-1	1
Run 17	-1	1	1	1	1	-1	1	-1	1	-1
Run 18	-1	1	-1	-1	-1	-1	1	1	-1	-1
Run 19	1	-1	1	-1	-1	-1	-1	1	1	-1
Run 20	1	-1	-1	1	-1	-1	1	1	1	1
Run 21	1	1	1	1	1	1	1	1	1	1

3.3.4.3 FAM2b Models

FAM2b is a geostatistical petrophysical model, without considering modeling the 4 petrofacies. After upscaling well logs ϕ to the simulation grid, ϕ is directly populated in the interwell region using SGS, using a single set of ϕ variogram models fitted to all (up-scaled) ϕ at the well locations (not shown). k_h is then populated from ϕ using end members of PPT. It should be emphasized that since FAM2b doesn't model facies, only a single set of k_h - ϕ transform end members is used (Figure 3.6; left). Similarly, the k_v/k_h ratio end members are developed for the entire Nugget Sandstone, based on data shown in Figure 3.4. For each cell, the -1 case is set to 0.02 and the +1 case is set to 2. The PB design table for FAM2b is shown in Table 3.6.

3.3.4.4 FAM2a Models

FAM2a is a geostatistical petrofacies model, without considering sub-facies petrophysical variations. Four discrete petrofacies are categorized and modeled in an identical procedure as described above for FAM4. In FAM2a, ϕ and k are homogeneous within each petrofacies, their values shown in Table 3.3. The PB design table for FAM2a is shown in Table 3.7.

TABLE 3.6: PB design for FAM2b.

Runs	PCA	PCR	PPT	VHR	SAL	RGS	RPM	TG
Run 1	0	0	0	0	0	0	0	0
Run 2	-1	-1	-1	1	-1	-1	1	-1
Run 3	1	-1	1	1	1	-1	-1	-1
Run 4	1	1	1	-1	-1	-1	1	-1
Run 5	-1	1	-1	1	1	1	-1	-1
Run 6	1	-1	-1	-1	1	-1	-1	1
Run 7	-1	-1	1	-1	1	1	1	-1
Run 8	1	-1	-1	1	-1	1	1	1
Run 9	-1	1	1	1	-1	-1	-1	1
Run 10	-1	1	-1	-1	1	-1	1	1
Run 11	-1	-1	1	-1	-1	1	-1	1
Run 12	1	1	-1	-1	-1	1	-1	-1
Run 13	1	1	1	1	1	1	1	1

TABLE 3.7: PB design for FAM2a.

Runs	FCA	FCR	VHR	SAL	RGS	RPM	TG
Run 1	1	-1	-1	-1	1	-1	-1
Run 2	-1	-1	-1	1	-1	-1	1
Run 3	1	1	-1	-1	-1	1	-1
Run 4	1	1	1	1	1	1	1
Run 5	-1	-1	1	-1	1	1	1
Run 6	0	0	0	0	0	-1	-1
Run 7	-1	1	-1	1	1	1	-1
Run 8	-1	-1	1	-1	-1	1	-1
Run 9	1	1	1	-1	-1	-1	1
Run 10	1	-1	-1	1	-1	1	1
Run 11	1	-1	1	1	1	-1	-1
Run 12	-1	1	-1	-1	1	-1	1
Run 13	-1	1	1	1	-1	-1	-1

3.3.4.5 FAM1 Models

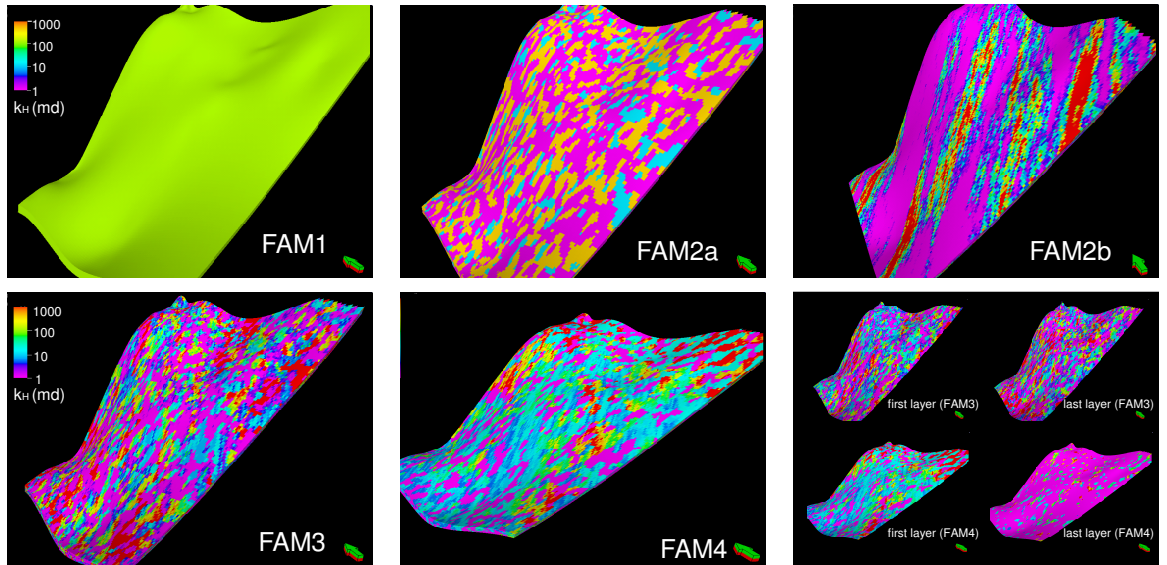
FAM1 is a simple homogeneous model, with a mean ϕ (0.13) and a mean k_h (123.2 mD) established from averaging those of FAM4. The PB design table for FAM1 is shown in Table 3.8.

3.3.4.6 Comparison Between Model Families

A realization of horizontal permeability from each model family is shown (Figure 3.24), corresponding to the center run of the PB design, i.e., all parameters assume their median values. Depending on the modeling choice and the amount of supporting data, different heterogeneity patterns are created. FAM1 and FAM2 models have less internal

TABLE 3.8: PB design for FAM1.

Runs	VHR	SAL	RGS	RPM	TG
Run 1	-1	1	-1	1	1
Run 2	0	0	0	-1	-1
Run 3	-1	-1	1	-1	-1
Run 4	1	-1	-1	1	-1
Run 5	1	1	1	-1	-1
Run 6	-1	-1	-1	1	-1
Run 7	1	1	-1	-1	-1
Run 8	1	-1	1	1	1
Run 9	1	1	1	1	1
Run 10	1	-1	-1	-1	1
Run 11	-1	1	-1	-1	1
Run 12	-1	1	1	1	-1
Run 13	-1	-1	1	-1	1

FIGURE 3.24: A k_h model realization, one for each family.

structure than models of FAM3 and FAM4 as expected. In FAM3, facies distribution is statistically homogeneous throughout the reservoir and as mean k_h does not vary across the layers. In FAM4, reservoir rocks with good quality are observed in the upper Nugget Sandstone because of the conditioning by facies probability cube. Thus, permeability is much higher in the lower reservoir layers. In addition, due to the porosity-depth trend imposed in FAM4, permeability of models in this family gradually decreases with increasing depth, while this effect is absent in all the other families. Figure 3.24 here serves to illustrate the difference in mean heterogeneity representation among the model families. Additional variability also exists among the models created for each family, when geologic parameters and modeling choices are varied according to the DoE.

3.4 Dynamic Modeling of CO₂ Injection & Monitoring (Simulation)

The same CO₂ storage scenario is simulated in all models using GASWAT of Eclipse 300, a multiphase compositional simulator that can incorporate temperature variation with depth. Other simulators such as CO2STORE are also available. However, due to the fact that our study site is a deep inclined aquifer, other simulators are generally not suitable. For example, CO2STORE module is limited by temperature (maximum: 100°C (212 °F)) and pressure (maximum: 600 bar) ranges as constrained by existing experimental data. Temperature and pressure conditions at our study site generally exceed these maximum values when depth is greater than 3 km. GASWAT models gas/aqueous phase equilibrium through an equation of state. Three components: CO₂, H₂O, NaCl, are defined. Initial pressure in the model is hydrostatic, with a reference pressure set at 5412 psi at depth =12,000 ft (a brine density of 1.04 g/cm³ is assumed). Reservoir temperature is assigned based on interpolated temperature log data (Figure 3.8). Model boundaries are represented by a Carter-Tracy analytical aquifer of a large radius and thickness [88], which ensures an open boundary that allows the formation brine, and later CO₂, to flow out. Model is considered part of a larger semi-infinite system where the injected gas and formation brine can flow out from the top, bottom, and sides of the formation. This is consistent with the known regional geologic framework. The lower BC at the Absaroka Fault is uncertain and is assumed open in this study, based on the hydrocarbon charging history of the Nugget Sandstone of oil fields to the west of the thrust fault (Figure 1.1). Source rock for these oil fields is thought to be subthrust Cretaceous shales [63] [70] and the Absaroka thrust formed during late Cretaceous [89] (Figure 1.2). The Absaroka Thrust existed at the time when hydrocarbons first began to migrate (Eocene or later) [70], thus the thrust fault (i.e., the lower boundary of the model) should be leaky so that hydrocarbons could migrate to the Jurassic Nugget Sandstone reservoirs above the hanging wall. For the present time, however, precise nature of this fault-bounded boundary is not clear. Additional simulations are run, setting this BC to no-flow, without significantly changing the simulation outcomes. It is well known that flow disturbance is generally not significantly influenced by the BC type, if the boundary lies far from the center of disturbance [90].

The choice of BC ensures that excessive pressure buildup will not occur near the injection well, which is perforated at a depth of 13,500 ft. A fixed mass injection rate of 1/3 M tons/year is used and the injection phase lasts 50 years. An injector bottomhole pressure constraint is set at 180 % hydrostatic pressure to prevent hydraulically fracturing the formation [5]. Due to the open BC, pressure buildup in the reservoir is modest, and the constant injection rate was maintained by all families. Thus, all models have injected

the same amount of CO₂ over a 50-year period. A total of 17 Mt of CO₂ has been injected, corresponding to 1/3 the emission rate of a small power plant (note that the total amount of CO₂ injected is largely constrained by the lower end member of the k_h - ϕ transform). To achieve a higher injection rate, multiple injectors can be utilized, whereas pressure buildup can be additionally controlled by adding brine producers [14]. These scenarios are not investigated in this study. Since the effect of model complexity on the long-term fate of the injected CO₂ is also of interest, a post-injection monitoring phase is simulated for 1950 years. This time frame is selected so that the CO₂ plume will migrate far enough from the injector, thus the effect of large-scale heterogeneity on CO₂ migration and trapping can be evaluated. For each family, at increasing time scales, parameters important to predicting brine leakage, trapped gas, dissolved gas, and CO₂ storage ratio (SR) are identified, along with the uncertainty in selected outcomes.

Finally, different equations of state (EOS) are available in describing phase density and mutual solubility of free-phase CO₂ and formation brine of difference salinities. However, due to low solubility of H₂O in gaseous or supercritical CO₂, differences in phase density estimates by different EOS do not appear to significantly influence simulation results [8]. Thus, potential differences in EOS as adopted by different reservoir simulators is not investigated (though the SA methodology can accommodate this uncertainty as a categorical factor), and all simulations are conducted with GASWAT.

Methodology

Chapter 4

Results and Discussion

Results of this study are presented in four sections: (1) screening test outcomes; (2) RS modeling and verification; (3) MC analysis assessing uncertainty in the outcomes; (4) end-member plume footprint for each model family.

4.1 Screening Tests

Screening test results of all model families are examined for 4 outcomes (Table 4.1). For predicting the SR at EOM, t-ratio of each factor is listed for FAM4, which is used to determine the significance of this factor in predicting the SR (Figure 4.1). The statistical tests are conducted for all outcomes, and at different times (not shown).

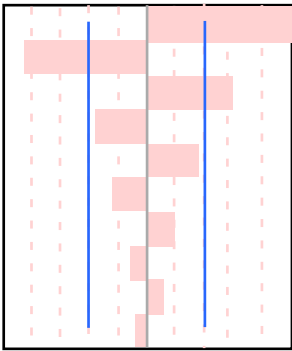
Outcome: Storage Ratio				FAM4 (EOM)	
Term	Estimate	Std Error	t Ratio		Prob> t
PPT	0.0987	0.017782	5.55		0.0002*
FCR	-0.0845	0.017782	-4.75		0.0008*
RGS	0.0595	0.017782	3.35		0.0074*
PCA	-0.0359	0.017782	-2.02		0.0711
RPM	0.034678	0.017782	1.99		0.0741
SAL	-0.0236	0.017782	-1.33		0.2139
VHR	0.018	0.017782	1.01		0.3353
TG	-0.010422	0.017782	-0.60		0.5623
FCA	0.0104	0.017782	0.58		0.5716
PCR	-0.0084	0.017782	-0.47		0.6488

FIGURE 4.1: An example screening test result for FAM4 at a 90% significance level. Outcome is the SR at EOM. Statistically significant factors here include ϕ - k transform, petrofacies range, and residual gas saturation. Negative t-ratio means increasing value of this factor will reduce SR.

TABLE 4.1: Significant factors identified by the PB design for each family that impact the prediction of different outcomes. Significance level = 90%; EOI: end of injection; EOM: end of monitoring.

Brine Leakage	EOI	EOM	Number of Runs
FAM1	RPM/SAL	RPM/SAL	13
FAM2a	FCR	FCR	13
FAM2b	PPT/PCA	PPT	13
FAM3	PPT	PPT	21
FAM4	PPT/FCR/FCA/VHR	PPT/FCR/FCA/VHR	21
Trapped Gas	EOI	EOM	Number of Runs
FAM1	TG	SAL/RPM/RGS	13
FAM2a	RPM	RGS/SAL/RPM	13
FAM2b	RPM/PPT/RGS	PPT/SAL/PCA/RGS	13
FAM3	RPM/PPT	PPT/RGS	21
FAM4	RPM/PPT/RGS/TG	PPT/SAL/FCR/RGS	21
Dissolved Gas	EOI	EOM	Number of Runs
FAM1	SAL/RPM/TG	SAL/RPM/VHR	13
FAM2a	SAL	SAL	13
FAM2b	PPT/SAL/TG/RPM/PCA	PPT/SAL	13
FAM3	PPT/SAL	PPT/PCA	21
FAM4	PPT/SAL/FCR	PPT/FCR/SAL	21
SR	EOI	EOM	Number of Runs
FAM1	TG	SAL	13
FAM2a	RPM	VHR	13
FAM2b	PPT/TG	PPT/RGS	13
FAM3	PPT/RPM	PPT/RPM	21
FAM4	PPT/RPM/RGS	PPT/FCR/RGS	21

In FAM4, PPT, FCR, FCA, VHR are the 4 most important factors predicting brine leakage over the entire simulation time, indicating that brine leakage is dominated by permeability distribution. This is expected, because permeability distribution determines the evolution of reservoir pressure, which controls the flow of formation brine. In predicting trapped gas, results at EOI are somewhat different from those at EOM, reflecting changing dominant flow process in the reservoir over time: after injection ceases, gravity gradually out-competes viscous drive. The relative permeability model and the temperature gradient are the most important during injection but become unimportant by EOM. During monitoring, PPT and FCR have a dominant effect on increasing the amount of trapped gas: higher mean permeability and greater lateral continuity of the high-k facies contribute to more lateral plume spreading period. More brine is in contact with the gas, thus more residual trapping during imbibition. Moreover, these factors are consistently dominating the prediction of the trapped gas, because gas is continuously migrating along the tilted reservoir. In predicting dissolved gas, PPT and FCR are the

most important factors, due to similar reasons described: more lateral plume spreading causes more gas to contact brine, and therefore more dissolution.

For each family, results are compared *at different timescales*. In predicting brine leakage, the important factors remain the same for all families, indicating that this outcome is consistently controlled by the pressure behavior of the model. In predicting trapped gas, results differ among the families to some degree. For FAM2, 3, and 4, RPM is important by EOI but becomes unimportant by EOM, suggesting a competing relationship between viscous force and gravity during the transition from injection to monitoring. The same explanation goes for FAM1, where TG is important during injection but not during monitoring. In predicting dissolved gas, spreading of the gas plume becomes more important during monitoring. For example, for FAM3 and FAM4, PCA and FCR becomes more important than SAL by EOM. Over all timescales, SAL consistently exerts a negative effect on the amount of dissolved gas, as expected.

When comparing results across model families *at the same time*, we observe: as model complexity increases, compared to the EEFs varied, geologic factors which determine permeability distribution in the reservoir become increasingly important for predicting the performance metrics, especially by EOM. This is revealed when we examine PPT, which is a geologic factor incorporated in FAM2b, 3, and 4. For each family, PPT is dominantly important for all the outcomes evaluated at all the time scales considered. However, many reservoir simulation studies are conducted based on a fixed geological model (e.g., a deterministic layered model). A sensitivity study is then conducted varying a variety of EEFs. Given a simple geologic model (e.g., FAM1), some EEFs may be identified as dominant factors influencing the outcomes. However, as demonstrated here, when complexity is built into the geologic model reflecting increasing knowledge of the site condition (which can be obtained at the increased cost of characterization), the sensitivity study should incorporate additional uncertain geological factors. These factors become dominant while some of the EEFs become far less important. For example, in our simple families, RPM and RGS are identified as key factors. But as more geologic complexity is incorporated, these factors are giving way to factors such as PPT and FCR.

Clearly, the notion that residual gas saturation exerts a dominant control on predicting trapped gas is true only when the geologic model is known. For deep saline aquifers where site data are extremely sparse, uncertainty in building the site model will likely dominate the prediction outcomes over uncertainty of such factors as residual gas. This is because permeability can vary over many orders of magnitude, thus uncertainty factors influencing its magnitude, orientation, and connectivity can induce large changes in the permeable pathways through which gas migrates. Magnitude of permeability also

influences the speed of gas migration and reservoir pressure. Parameters such as RGS only vary within 1 order of magnitude, exerting much less impact on the prediction uncertainty. For a data-sparse system being considered for gas disposal or other applications, resources should be first devoted to characterizing geologic uncertainty factors such as ϕ - k transform and facies correlation structure.

4.2 RS Modeling & Verification

For each family, at two time scales (EOI and EOM), the PB design has identified a set of important uncertainty parameters. After pooling together all the important parameters, an RS design based on these parameters is generated to develop a proxy model for reservoir simulation. The pooling result is an union of all the parameters identified important for each selected simulation outcome over the two time scales (EOI and EOM). For example, if PPT is not important at EOI but becomes important at EOM, PPT is included in the RS design. Also, if PPT is not important regarding trapped gas but is important with regard to dissolved gas, it is included in the RS design as well. The RS designs are typically of higher resolution than the screening design, thus more simulation runs are needed. For the families, the number of runs dictated by the RS design is 44 (FAM1), 44 (FAM2a), 46 (FAM2a), 44 (FAM3), 80 (FAM4) (Table 4.2 ~ Table 4.6). For each family, the RS model is a 2nd order polynomial that is fitted to these simulation outcomes. Storage ratio RS models are created at different timescales: 2011(start of injection), 2041, 2061(EOI), 2310, 2810, 3210, 3610, and 4010(EOM). An example 2nd order polynomial RS model of storage ratio for FAM4 at EOI is shown in Table 4.7.

The RS models are first verified by comparing their predictions to simulation outcomes that were not used in generating the RS model, i.e., the PB design points. Following the example, the predicted SR values using fitted RS model are compared to the simulated SR values at PB design points for FAM4 at EOI (Table 4.8). Though such selection may overestimate the RS error, this comparison still yields small differences (Table 4.9). Means of the errors are close to 0.0, standard deviations are generally small and decrease with time, and the error distributions are frequently symmetric around the means (Figure 4.2). Furthermore, had the verification points been selected internal to the parameter space, the RS error would be expected to be even smaller. Given the above results, the RS models are considered adequate proxy models and will be used in the MC uncertainty analysis.

TABLE 4.2: Response surface design for FAM1.

Runs	TG	RPM	RGS	SAL	VHR
Run 1	1	1	1	1	1
Run 2	0	1	0	0	0
Run 3	1	-1	-1	-1	1
Run 4	-1	1	-1	1	1
Run 5	0	0	0	0	0
Run 6	1	-1	-1	-1	-1
Run 7	0	0	-1	0	0
Run 8	0	0	0	0	-1
Run 9	-1	1	-1	1	-1
Run 10	-1	1	1	-1	-1
Run 11	-1	1	1	1	-1
Run 12	-1	-1	-1	-1	1
Run 13	1	0	0	0	0
Run 14	-1	1	-1	-1	1
Run 15	-1	-1	-1	-1	-1
Run 16	1	1	-1	1	-1
Run 17	1	-1	1	-1	1
Run 18	0	0	0	0	0
Run 19	1	1	1	1	-1
Run 20	1	1	-1	-1	1
Run 21	-1	0	0	0	0
Run 22	-1	-1	1	-1	1
Run 23	1	-1	-1	1	-1
Run 24	1	1	1	-1	-1
Run 25	-1	1	-1	-1	-1
Run 26	0	-1	0	0	0
Run 27	-1	1	1	-1	1
Run 28	-1	1	1	1	1
Run 29	-1	-1	-1	1	-1
Run 30	0	0	0	0	1
Run 31	1	-1	1	-1	-1
Run 32	-1	-1	1	1	-1
Run 33	-1	-1	1	-1	-1
Run 34	1	1	-1	-1	-1
Run 35	1	-1	1	1	-1
Run 36	-1	-1	-1	1	1
Run 37	1	1	-1	1	1
Run 38	0	0	0	1	0
Run 39	1	-1	-1	1	1
Run 40	-1	-1	1	1	1
Run 41	1	-1	1	1	1
Run 42	0	0	0	-1	0
Run 43	0	0	1	0	0
Run 44	1	1	1	-1	1

TABLE 4.3: Response surface design for FAM2a.

Runs	FCR	RPM	RGS	SAL	VHR
Run 1	-1	-1	1	1	1
Run 2	-1	-1	-1	-1	1
Run 3	1	1	1	-1	1
Run 4	0	0	1	0	0
Run 5	0	0	0	0	0
Run 6	-1	-1	1	1	-1
Run 7	0	0	-1	0	0
Run 8	-1	1	1	1	-1
Run 9	1	1	1	1	-1
Run 10	1	-1	-1	-1	-1
Run 11	-1	1	-1	-1	1
Run 12	-1	1	1	1	1
Run 13	1	-1	-1	1	1
Run 14	-1	0	0	0	0
Run 15	1	1	-1	1	-1
Run 16	1	-1	1	1	1
Run 17	1	-1	1	-1	1
Run 18	0	1	0	0	0
Run 19	-1	1	-1	1	1
Run 20	1	0	0	0	0
Run 21	-1	-1	-1	1	-1
Run 22	0	0	0	0	0
Run 23	-1	1	1	-1	-1
Run 24	1	1	-1	1	1
Run 25	1	1	1	-1	-1
Run 26	1	-1	-1	1	-1
Run 27	1	1	-1	-1	1
Run 28	-1	1	-1	1	-1
Run 29	-1	1	-1	-1	-1
Run 30	1	1	1	1	1
Run 31	1	-1	-1	-1	1
Run 32	1	1	-1	-1	-1
Run 33	0	0	0	1	0
Run 34	0	0	0	-1	0
Run 35	-1	-1	1	-1	1
Run 36	-1	-1	-1	1	1
Run 37	0	-1	0	0	0
Run 38	-1	-1	1	-1	-1
Run 39	0	0	0	0	-1
Run 40	0	0	0	0	1
Run 41	1	-1	1	-1	-1
Run 42	-1	1	1	-1	1
Run 43	-1	-1	-1	-1	-1
Run 44	1	-1	1	1	-1

TABLE 4.4: Response surface design for FAM2b.

Runs	PPT	PCA	RPM	RGS	SAL	TG
Run 1	1	1	1	1	1	-1
Run 2	-1	-1	-1	-1	1	-1
Run 3	0	0	0	0	1	0
Run 4	-1	1	1	-1	-1	1
Run 5	1	0	0	0	0	0
Run 6	1	1	-1	-1	-1	1
Run 7	0	0	0	0	0	-1
Run 8	1	-1	1	1	-1	-1
Run 9	1	-1	-1	-1	1	1
Run 10	0	1	0	0	0	0
Run 11	-1	1	1	-1	1	-1
Run 12	-1	-1	1	-1	1	1
Run 13	0	0	0	0	0	0
Run 14	-1	-1	1	-1	-1	-1
Run 15	1	-1	-1	1	-1	1
Run 16	-1	-1	-1	-1	-1	1
Run 17	1	1	-1	1	-1	-1
Run 18	-1	1	1	1	-1	-1
Run 19	0	0	0	-1	0	0
Run 20	1	1	-1	-1	1	-1
Run 21	-1	1	-1	-1	1	1
Run 22	-1	1	-1	1	-1	1
Run 23	-1	0	0	0	0	0
Run 24	-1	-1	-1	1	-1	-1
Run 25	1	-1	-1	-1	-1	-1
Run 26	0	0	0	0	0	0
Run 27	1	1	1	-1	1	1
Run 28	-1	-1	1	1	-1	1
Run 29	-1	-1	-1	1	1	1
Run 30	0	0	0	0	-1	0
Run 31	-1	1	-1	1	1	-1
Run 32	-1	-1	1	1	1	-1
Run 33	1	-1	1	-1	-1	1
Run 34	0	0	1	0	0	0
Run 35	1	-1	-1	1	1	-1
Run 36	0	0	0	1	0	0
Run 37	0	0	-1	0	0	0
Run 38	-1	1	-1	-1	-1	-1
Run 39	1	1	1	-1	-1	-1
Run 40	1	-1	1	-1	1	-1
Run 41	1	-1	1	1	1	1
Run 42	1	1	-1	1	1	1
Run 43	0	0	0	0	0	1
Run 44	-1	1	1	1	1	1
Run 45	1	1	1	1	-1	1
Run 46	0	-1	0	0	0	0

TABLE 4.5: Response surface design for FAM3.

Runs	PPT	RPM	RGS	SAL	PCA
Run 1	1	1	1	1	-1
Run 2	-1	-1	-1	1	1
Run 3	-1	-1	-1	-1	1
Run 4	0	0	0	0	0
Run 5	1	1	-1	1	-1
Run 6	1	-1	1	1	-1
Run 7	0	0	0	1	0
Run 8	-1	1	-1	-1	-1
Run 9	1	-1	1	-1	1
Run 10	0	1	0	0	0
Run 11	0	-1	0	0	0
Run 12	1	-1	-1	-1	-1
Run 13	-1	1	1	-1	-1
Run 14	0	0	0	0	-1
Run 15	-1	1	-1	1	1
Run 16	1	-1	1	1	1
Run 17	1	-1	-1	1	-1
Run 18	1	1	1	-1	1
Run 19	0	0	0	0	1
Run 20	0	0	0	0	0
Run 21	1	1	1	1	1
Run 22	-1	-1	-1	-1	-1
Run 23	-1	1	-1	-1	1
Run 24	0	0	-1	0	0
Run 25	-1	-1	-1	1	-1
Run 26	1	-1	1	-1	-1
Run 27	0	0	1	0	0
Run 28	1	-1	-1	-1	1
Run 29	-1	-1	1	1	1
Run 30	1	1	-1	-1	1
Run 31	1	1	-1	-1	-1
Run 32	-1	1	1	-1	1
Run 33	1	0	0	0	0
Run 34	1	1	1	-1	-1
Run 35	-1	-1	1	1	-1
Run 36	-1	1	1	1	-1
Run 37	-1	1	1	1	1
Run 38	-1	1	-1	1	-1
Run 39	1	-1	-1	1	1
Run 40	0	0	0	-1	0
Run 41	-1	0	0	0	0
Run 42	-1	-1	1	-1	1
Run 43	1	1	-1	1	1
Run 44	-1	-1	1	-1	-1

TABLE 4.6: Response surface design for FAM4.

Runs	PPT	FCR	FCA	VHR	RPM	RGS	SAL
Run 1	-1	1	1	1	1	-1	-1
Run 2	1	1	-1	-1	-1	1	1
Run 3	1	1	1	1	-1	-1	-1
Run 4	1	-1	1	-1	1	-1	1
Run 5	-1	-1	-1	-1	-1	-1	-1
Run 6	-1	0	0	0	0	0	0
Run 7	-1	1	-1	-1	1	-1	-1
Run 8	1	1	-1	-1	-1	-1	-1
Run 9	1	1	1	1	-1	1	1
Run 10	1	-1	1	-1	-1	-1	-1
Run 11	1	-1	1	1	-1	-1	1
Run 12	1	1	-1	-1	1	-1	1
Run 13	0	1	0	0	0	0	0
Run 14	-1	1	1	1	-1	1	-1
Run 15	0	0	0	1	0	0	0
Run 16	-1	-1	-1	1	-1	-1	1
Run 17	0	0	0	0	-1	0	0
Run 18	1	-1	-1	1	-1	-1	-1
Run 19	-1	-1	1	-1	-1	1	-1
Run 20	1	1	1	-1	1	-1	-1
Run 21	-1	1	1	-1	-1	1	1
Run 22	0	0	0	0	0	-1	0
Run 23	-1	1	-1	1	1	-1	1
Run 24	-1	-1	-1	1	1	-1	-1
Run 25	1	-1	1	1	1	-1	-1
Run 26	1	1	-1	-1	1	1	-1
Run 27	-1	1	-1	-1	1	1	1
Run 28	1	1	-1	1	1	1	1
Run 29	-1	1	1	1	1	1	1
Run 30	-1	1	-1	1	1	1	-1
Run 31	1	1	1	-1	-1	-1	1
Run 32	1	1	-1	1	-1	-1	1
Run 33	0	0	0	0	0	1	0
Run 34	0	0	0	0	0	0	0

Continued on Next Page...

Table 4.6 – (Continued)

Runs	PPT	FCR	FCA	VHR	RPM	RGS	SAL
Run 35	0	0	-1	0	0	0	0
Run 36	-1	-1	1	-1	1	-1	-1
Run 37	-1	1	1	1	-1	-1	1
Run 38	0	0	1	0	0	0	0
Run 39	-1	1	-1	1	-1	1	1
Run 40	-1	-1	-1	-1	1	1	-1
Run 41	-1	-1	-1	1	-1	1	-1
Run 42	1	-1	-1	1	1	-1	1
Run 43	-1	-1	1	1	1	1	-1
Run 44	1	1	1	1	1	1	-1
Run 45	1	-1	1	1	-1	1	-1
Run 46	0	-1	0	0	0	0	0
Run 47	1	-1	1	1	1	1	1
Run 48	-1	-1	1	1	-1	1	1
Run 49	-1	-1	1	-1	-1	-1	1
Run 50	-1	-1	-1	-1	-1	1	1
Run 51	1	-1	1	1	1	1	-1
Run 52	-1	1	1	-1	1	-1	1
Run 53	-1	1	-1	-1	-1	-1	1
Run 54	1	1	1	1	1	-1	1
Run 55	1	1	1	-1	1	1	1
Run 56	-1	-1	1	1	1	-1	1
Run 57	0	0	0	0	0	0	0
Run 58	1	1	1	-1	-1	1	-1
Run 59	-1	-1	1	1	-1	-1	-1
Run 60	-1	1	-1	1	-1	-1	-1
Run 61	1	-1	-1	-1	1	1	1
Run 62	0	0	0	0	0	0	-1
Run 63	1	-1	1	-1	-1	1	1
Run 64	1	0	0	0	0	0	0
Run 65	0	0	0	0	0	0	1
Run 66	1	-1	-1	-1	-1	1	-1
Run 67	-1	1	1	-1	-1	-1	-1
Run 68	-1	1	-1	-1	-1	1	-1

Continued on Next Page...

Table 4.6 – (Continued)

Runs	PPT	FCR	FCA	VHR	RPM	RGS	SAL
Run 69	-1	-1	1	-1	1	1	1
Run 70	0	0	0	0	1	0	0
Run 71	1	-1	-1	-1	1	-1	-1
Run 72	1	1	-1	1	-1	1	-1
Run 73	1	1	-1	1	1	-1	-1
Run 74	1	-1	-1	-1	-1	-1	1
Run 75	-1	-1	-1	-1	1	-1	1
Run 76	1	-1	-1	1	-1	1	1
Run 77	0	0	0	-1	0	0	0
Run 78	-1	1	1	-1	1	1	-1
Run 79	1	-1	1	-1	1	1	-1
Run 80	-1	-1	-1	1	1	1	1

4.3 MC Analysis

For each family, the RS models (at 7 different timescales) are used to assess the prediction uncertainty of the SR, which arises from uncertainty of the input parameters — both GF and EEf. This is accomplished by running 500,000 MC simulations with the RS model, through randomly sampling the input parameters (i.e., axes of the RS model) according to their respective univariate pdfs. A random drawing of a vector of the input parameters gives rise to one RS-predicted outcome. Therefore, after 500,000 drawings, 500,000 RS-predicted SR values would be generated (Figure 4.3). After ranking these 500,000 outcomes, a cdf of the SR can be created (e.g., Figure 4.4; solid line). Typically, a set of MC runs takes less than one second to run on a PC workstation.

From the cdf, certain quantiles could be drawn. In this study, a prediction envelope is defined by an interval between P10 and P90 quantiles. Prediction envelope of the RS-predicted SR is compared among the families over the entire simulation time (Figure 4.5). Results suggest a large uncertainty range in the SR, given the uncertainties in parameters and modeling choices. At the end of injection, SR ranges from 0.18 to

TABLE 4.7: Parameter estimates of a 2nd order polynomial RS model of storage ratio for FAM4 at EOI.

Terms	Estimate	Std Error
Intercept	0.2285063	0.012458
PPT	0.0718446	0.005365
FCR	-0.008572	0.005365
FCA	0.0130932	0.005365
VHR	0.0341801	0.005365
RPM	-0.097358	0.005365
RGS	0.0122996	0.005365
SAL	-0.022164	0.005365
PPT*FCR	-0.007941	0.005448
PPT*FCA	0.0115555	0.005448
FCR*FCA	0.0062935	0.005448
PPT*VHR	0.0335989	0.005448
FCR*VHR	-0.019132	0.005448
FCA*VHR	-0.009681	0.005448
PPT*RPM	-0.003863	0.005448
FCR*RPM	0.0017663	0.005448
FCA*RPM	-0.00324	0.005448
VHR*RPM	-0.001706	0.005448
PPT*RGS	0.0113343	0.005448
FCR*RGS	-0.001621	0.005448
FCA*RGS	-0.001088	0.005448
VHR*RGS	0.0033376	0.005448
RPM*RGS	0.0029401	0.005448
PPT*SAL	-0.007479	0.005448
FCR*SAL	0.0009748	0.005448
FCA*SAL	-0.005545	0.005448
VHR*SAL	-0.00302	0.005448
RPM*SAL	-0.004809	0.005448
RGS*SAL	-0.003945	0.005448
PPT*PPT	0.010062	0.028601
FCR*FCR	-0.004114	0.028601
FCA*FCA	-0.000762	0.028601
VHR*VHR	0.0122268	0.028601
RPM*RPM	-0.008793	0.028601
RGS*RGS	0.0202575	0.028601
SAL*SAL	0.0162771	0.028601

TABLE 4.8: An example of RS predicted SR values versus simulated SR values at PB design points for FAM4 at EOI. Comparison is for verification of the RS fitted model.

PB runs	PPT	FCR	FCA	VHR	RPM	RGS	SAL	RS pre- dicted SR	PB simu- lated SR
Run 1	1	1	1	-1	-1	-1	1	0.385	0.402
Run 2	-1	1	1	1	-1	1	-1	0.298	0.319
Run 3	1	-1	1	-1	-1	-1	-1	0.414	0.418
Run 4	1	-1	-1	1	1	-1	-1	0.335	0.392
Run 5	0	0	0	0	0	0	0	0.229	0.246
Run 6	-1	-1	-1	1	1	1	1	0.131	0.094
Run 7	1	-1	-1	1	-1	1	-1	0.596	0.662
Run 8	-1	-1	1	1	-1	-1	1	0.291	0.281
Run 9	1	-1	-1	-1	-1	1	-1	0.386	0.633
Run 10	1	1	1	-1	1	1	-1	0.281	0.383
Run 11	1	1	-1	1	-1	1	1	0.453	0.438
Run 12	-1	1	-1	1	1	-1	-1	0.100	0.119
Run 13	-1	1	1	1	-1	-1	-1	0.292	0.299
Run 14	-1	1	-1	-1	1	-1	-1	0.121	0.121
Run 15	1	-1	1	1	1	-1	1	0.279	0.236
Run 16	-1	-1	-1	-1	-1	-1	1	0.272	0.272
Run 17	1	1	-1	-1	1	-1	1	0.102	0.118
Run 18	-1	1	-1	-1	-1	1	1	0.279	0.285
Run 19	-1	-1	1	-1	1	1	-1	0.119	0.120
Run 20	-1	-1	1	-1	1	1	1	0.065	0.0917
Run 21	1	1	1	1	1	1	1	0.276	0.8

TABLE 4.9: Summary of the RS error at the PB design points: Error = RS-predicted SR - simulated SR at PB points.

Family	EOI [min, mean, max, std]			EOM [min, mean, max, std]		
FAM1	$[-2.1 \times 10^{-1},$ $1.3 \times 10^{-1}]$	$1.0 \times 10^{-4},$	$2.1 \times 10^{-1},$	$[-3.5 \times 10^{-2},$ $2.0 \times 10^{-2}]$	$1.0 \times 10^{-2},$	$5.0 \times 10^{-2},$
FAM2a	$[-5.5 \times 10^{-1},$ $1.6 \times 10^{-1}]$	$-4.0 \times 10^{-2},$	$1.6 \times 10^{-1},$	$[-8.2 \times 10^{-2},$ $4.0 \times 10^{-2}]$	$1.0 \times 10^{-3},$	$1.1 \times 10^{-1},$
FAM2b	$[-5.4 \times 10^{-1},$ $1.5 \times 10^{-1}]$	$-4.0 \times 10^{-2},$	$3.0 \times 10^{-2},$	$[-1.6 \times 10^{-1},$ $6 \times 10^{-2}]$	$-9.0 \times 10^{-3},$	$8.8 \times 10^{-2},$
FAM3	$[-1.2 \times 10^{-1},$ $4.0 \times 10^{-2}]$	$-9.6 \times 10^{-3},$	$5.0 \times 10^{-2},$	$[-3.6 \times 10^{-1},$ $1.5 \times 10^{-1}]$	$-4.0 \times 10^{-2},$	$1.7 \times 10^{-1},$
FAM4	$[-5.2 \times 10^{-1},$ $1.2 \times 10^{-1}]$	$-4.0 \times 10^{-2},$	$4.0 \times 10^{-2},$	$[-1.9 \times 10^{-1},$ $6.0 \times 10^{-2}]$	$-2.0 \times 10^{-2},$	$7.0 \times 10^{-2},$

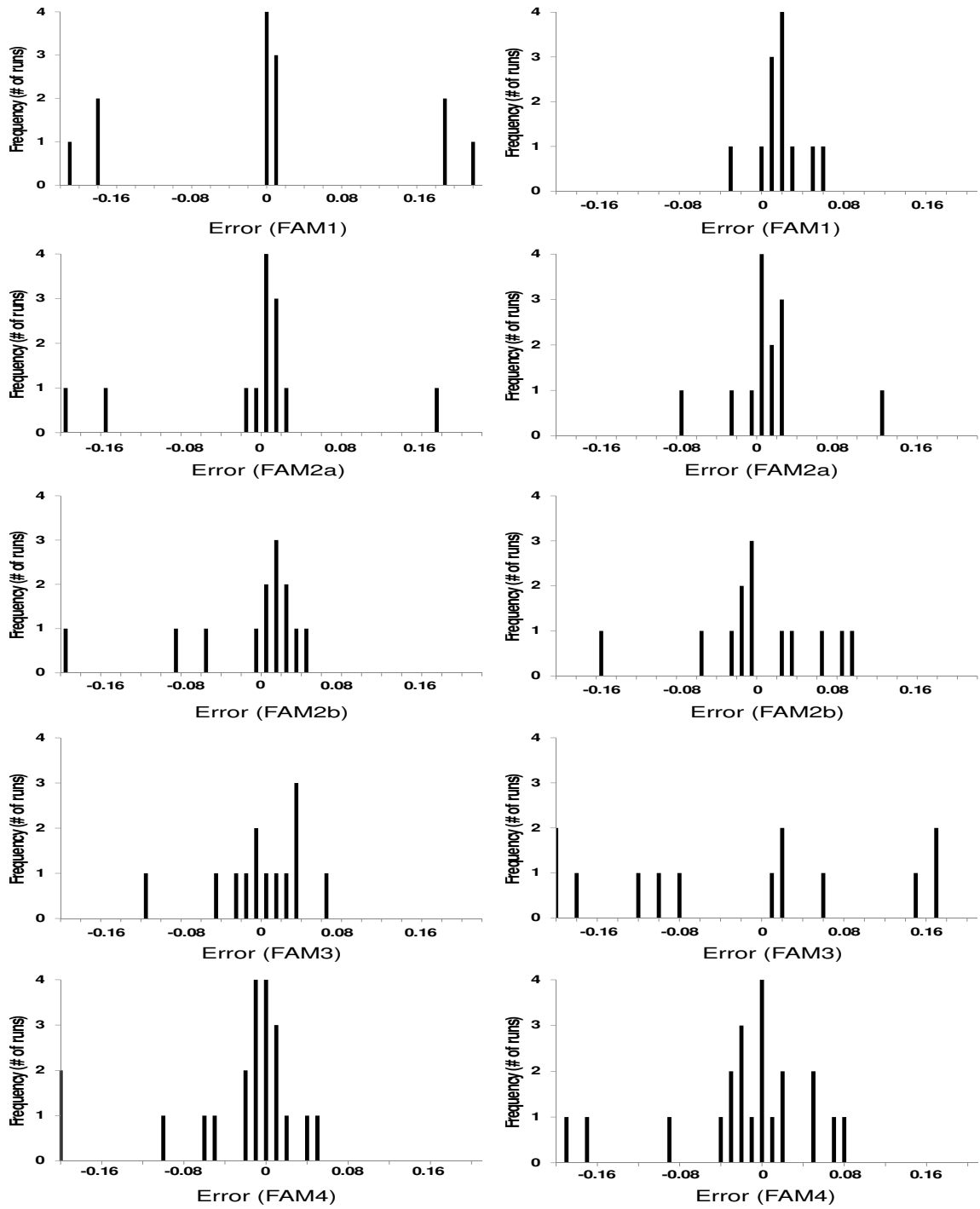


FIGURE 4.2: Verification of the RS storage ratio at the screening design points for each family: (left) EOI; (right) EOM.

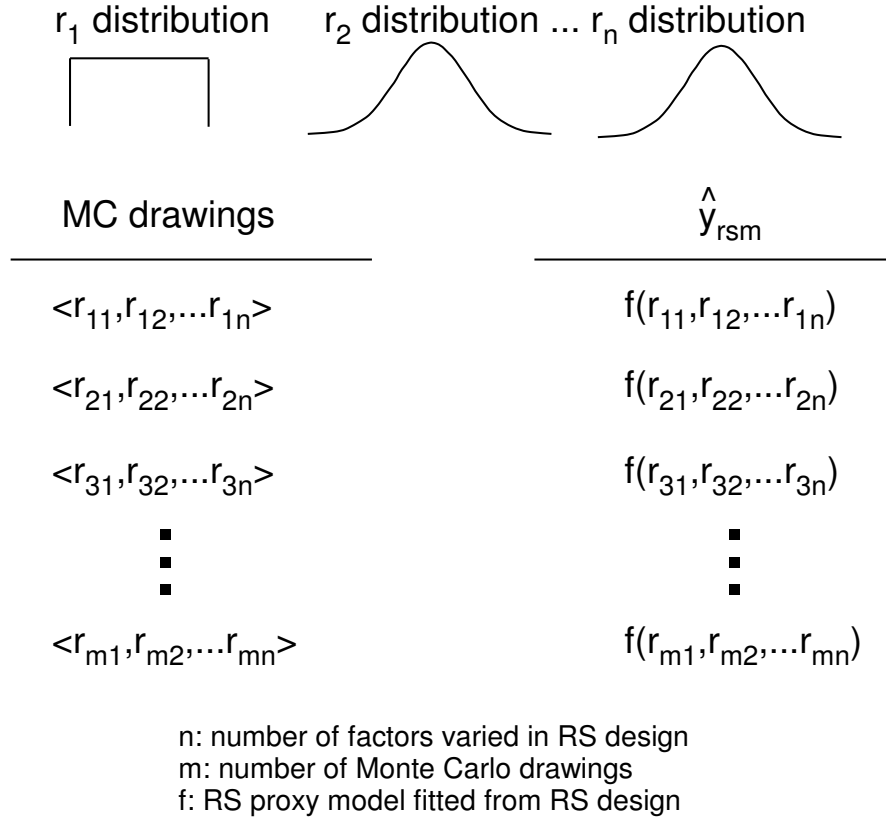


FIGURE 4.3: Schematic of MC simulations based on the RS proxy model generated from the RS design.

0.38. At the end of monitoring, SR ranges from 0.71 to 0.99. At all times, uncertainty ranges of FAM2b, FAM3, and FAM4 are larger than those of FAM1 and FAM2a, since the former models incorporate more geological complexities. However, the degree of variation in capturing the uncertainty range changes both with time and with the model complexity. By EOI, prediction envelopes of all families are more or less similar: during this shorter time frame, where plume migration is limited, heterogeneities near the injection site are not significantly different among the different model representations, thus simpler models can predict SR uncertainty that is similar to the complex models. During monitoring, prediction envelopes of each family deviate gradually from one another, reflecting different (evolving) large scale heterogeneity experienced by each family as the plume migrates and grows continuously. Compared to FAM4 (i.e., the most sophisticated model), all other families estimate higher mean SRs: the simpler the model, the greater the estimated mean SR. When comparing both magnitude and range of the uncertainty, prediction envelop of FAM3 is the closest to that of FAM4 (FAM2b's uncertainty range is the largest and FAM1 and FAM2a's ranges are much smaller).

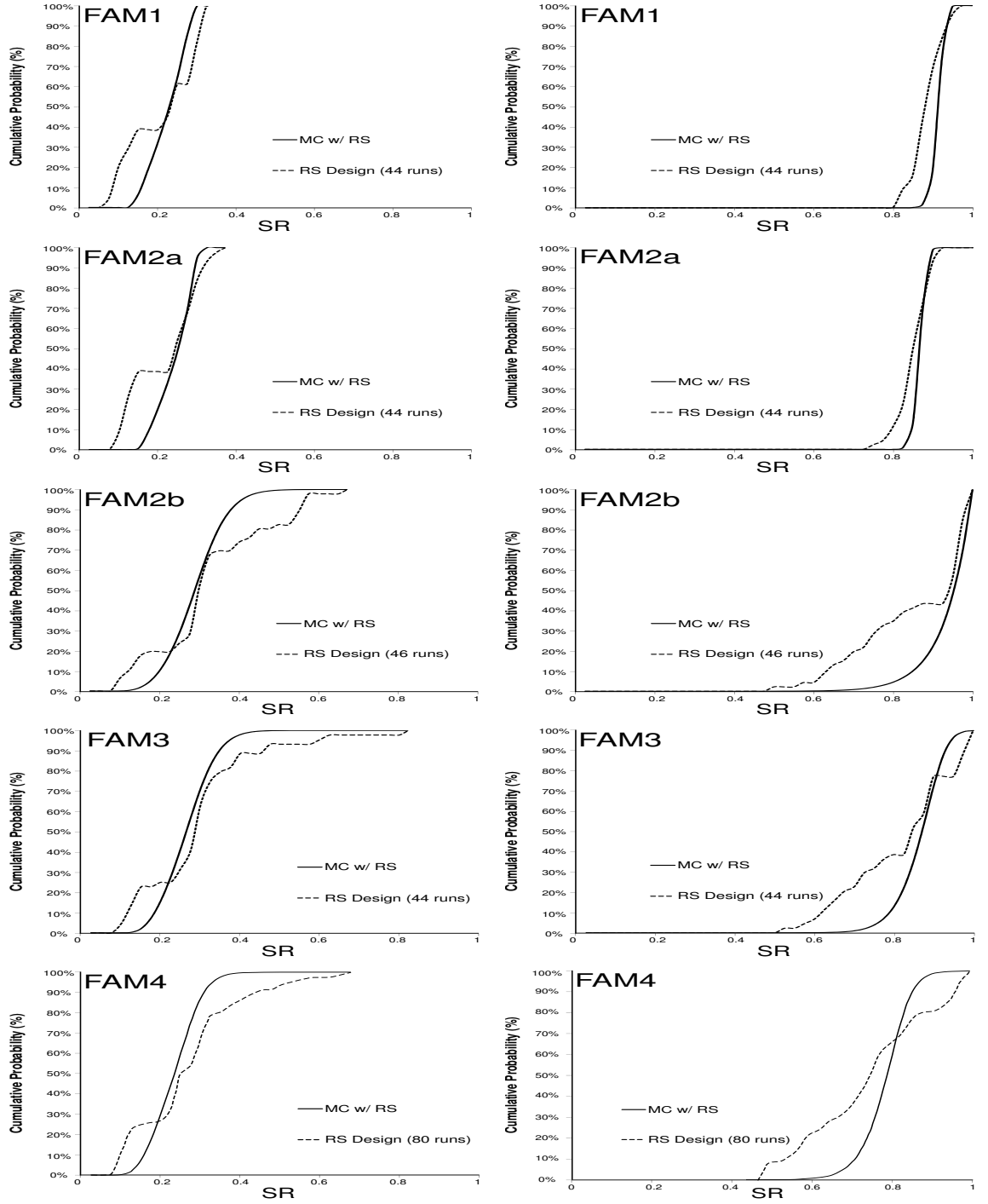


FIGURE 4.4: cdf of the RS-predicted SR for each family: (left) EOI; (right) EOM. “MC w/ RS” is generated with 500,000 MC simulations (exhaustive cdf); “RS design” is cdf constructed using results from RS runs.

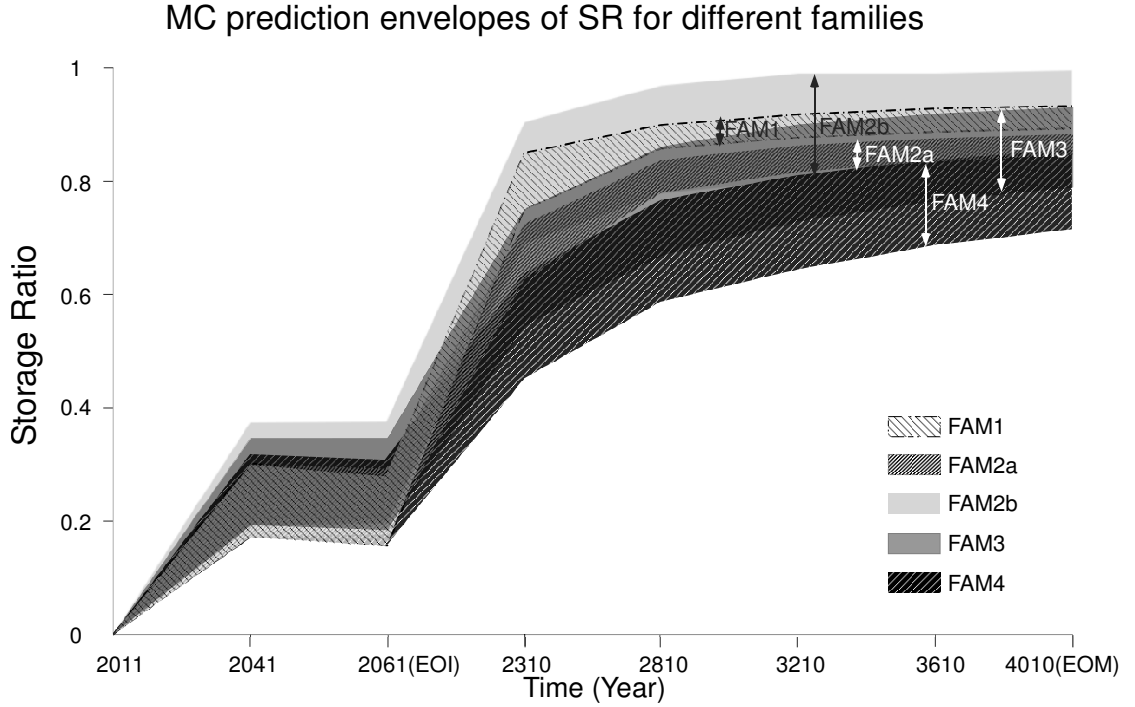


FIGURE 4.5: Prediction envelope of RS-predicted SR for each family over the entire simulation times. SRs between points of observation are linear interpolations.

4.4 Plume Footprint

From the RS design runs, a non-exhaustive cdf is also constructed, at two time scales (e.g., Figure 4.4; dashed line). Compared to the exhaustive cdf, its shape is much less smooth, as expected (the full parameter space is not sampled by the RS design), though it has captured, for the most part, the minimum and maximum SRs of the exhaustive cdf. This suggests that end-member simulation outcomes other than the SR may be identified from these design runs. One particular outcome of interest is the footprint of the gas-phase CO_2 plume, defined as the model layer with the maximum lateral plume size. When the SR is the highest, plume shape tends to be more laterally extensive, which contributes to more dissolution and residual trapping, and vice versa. Thus, estimates of end-member plume footprints can be established by visualizing the RS design runs corresponding to the minimal, median, and maximum SRs: at EOI (Figure 4.6) and EOM (Figure 4.7). For FAM1 & 2a, at each time scale, the end-member gas plumes are not as drastically different as in FAM2b, 3, and 4, since their SR uncertainty range is comparatively small. In FAM2b, 3, and 4, the differences are much more significant: gas plume of minimum SR sits around the wellbore and doesn't migrate far (which results in minimum dissolution and trapping), while gas plume of maximum SR migrates far away from the wellbore. This explains why PPT is always of prime importance for these families. PPT determines the mean permeability of the model: the higher the mean, the

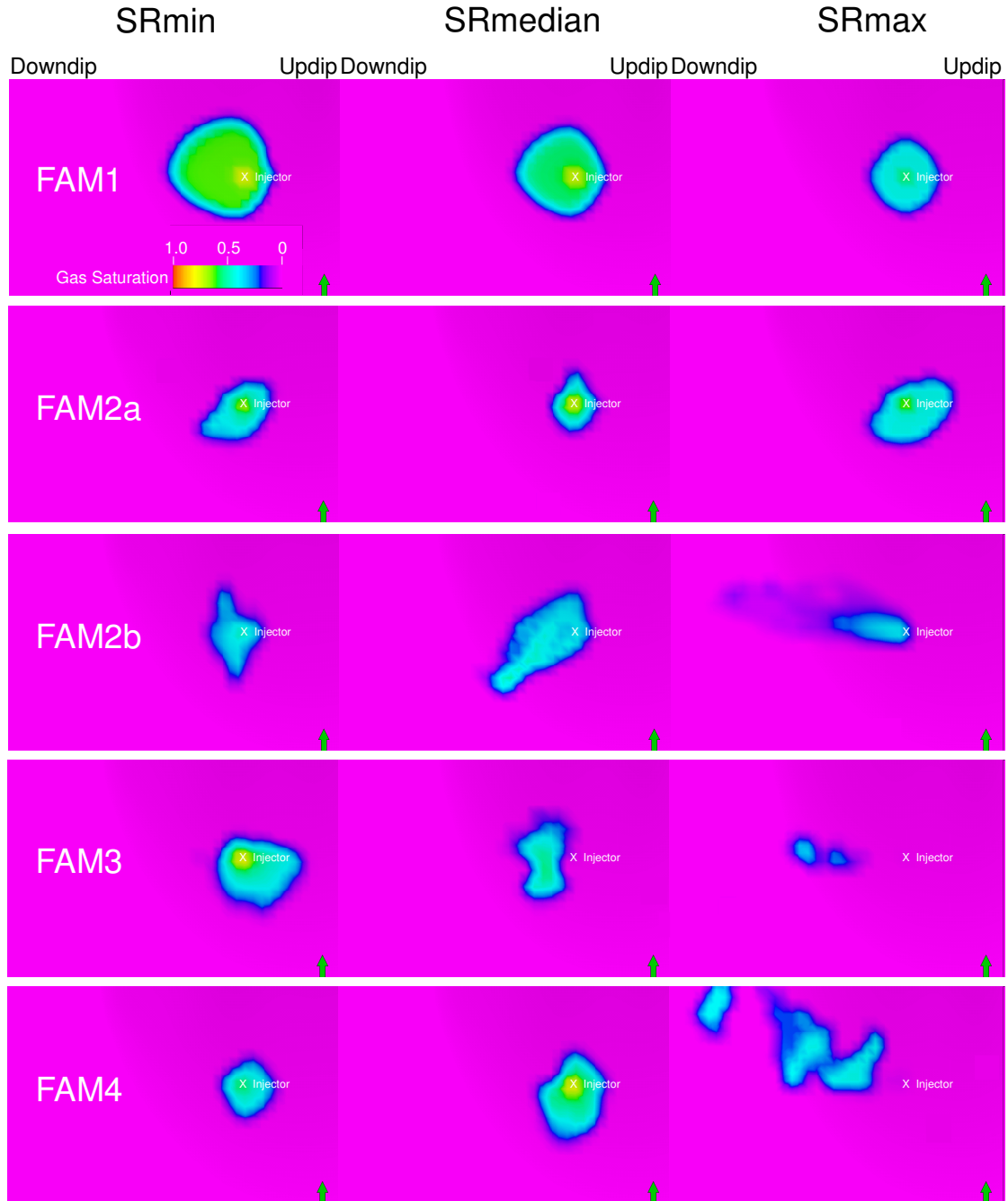


FIGURE 4.6: Gas saturation (mobile + trapped CO_2) predicted by each family (arrow points North) at EOI: (Left) Minimum SR; (Middle) Median SR; (Right) Maximum SR.

faster the CO_2 can migrate, and the more gas dissolution and trapping per unit time. In FAM4, at the maximum SR (~ 1), little trapped and mobile gas remains at EOM (Figure 4.7; bottom right). In this case, mean permeability is high and salinity is low, the gas plume spreads widely and quickly and is mostly dissolved by EOM.

Moreover, in cases where the temperature gradient is low (i.e., a cool basin), the gas plume migrates downdip. Due to low temperature and high fluid pressure, gas density

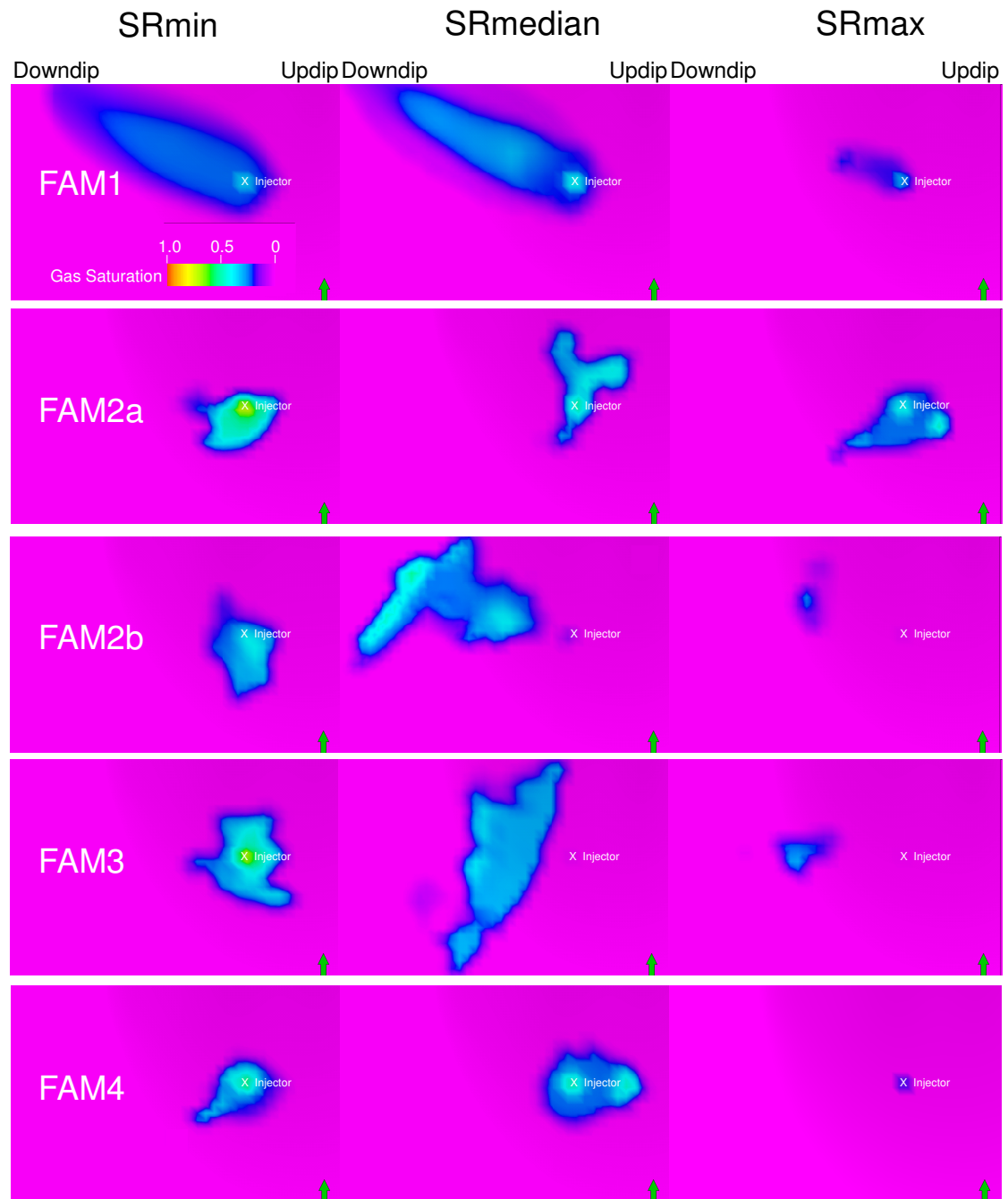


FIGURE 4.7: Gas saturation (mobile + trapped CO_2) predicted by each family (arrow points North) at EOM: (Left) Minimum SR; (Middle) Median SR; (Right) Maximum SR.

is higher than brine density, constituting a form of gravity-stable migration, which has been proposed under high injection pressure. Depending on the EOS, when temperature is higher than 120 °C (248 °F, which corresponds to a large section of our model), CO₂ dissolution in brine may reduce brine density compared to the original brine [8]. This effect is not calculated by the EOS of GASWAT, suggesting that if a different EOS is implemented, the simulated gravity-stable migration could be more pronounced. However, alternative EOS implemented by Eclipse 300 (i.e., CO2STORE module) is limited by temperature (maximum: 100 °C (212 °F)) and pressure (maximum: 600 bar) ranges as constrained by existing experimental data. CO2STORE cannot currently be extended to our model depth, nor does it account for depth-dependent temperature, which is essential for modeling an inclined reservoir. Clearly, future work can refine this study by testing alternative EOS models constrained by new experiments conducted under higher temperature and pressure conditions. Here, we demonstrate that in a cool basin, gravity-stable migration is possible when the depth of injection is sufficiently deep. Greater injection depth, though more expensive to operate, may offer greater storage security.

Finally, while the majority of the simulations predicts downdip migrations, a few runs are predicting up-dip migration due to high temperature gradient end member (e.g., median SR in FAM4 at EOM). At the study site, reduced uncertainty of TG is needed to evaluate whether gravity-stable migration is the most likely scenario.

Results and Discussion

Chapter 5

Conclusions

Injection of supercritical CO₂ into deep saline aquifers is considered a promising option to mitigate global climate change. To evaluate a storage site, reservoir simulation is performed using a geologic site model. However, GCS is a cost center. To resolve detailed aquifer heterogeneity, expensive subsurface characterization is required. The greater the detail, the higher the cost. Research is needed to develop a cost-effective strategy of data collection to support the building of site models. In this study, we evaluate the impact of different geologic, engineering, and environmental uncertainties on parameter importance and prediction uncertainty in modeling GCS in a deep inclined aquifer. Effect of geologic model complexity is investigated by building and simulating 4 model families according to experimental design. A response surface analysis then generates accurate proxy models for reservoir simulation with which uncertainty of predicting GCS performance metrics is evaluated. Results and insights are summarized below.

When model complexity is low, the most important uncertainty parameters influencing these performance metrics are engineering/environmental factors. When model increases in complexity, geologic uncertainty factors become more important. Clearly, key uncertainty factors are influenced by the modeling choice. For the CO₂ storage ratio, prediction uncertainty is large: 0.18~0.38 at end of injection, 0.71~0.99 at end of monitoring. By the end of injection, prediction envelope of the storage ratio differs little among the different model families; however, over the monitoring period, the prediction envelop deviates gradually from one another, reflecting different evolving large-scale heterogeneity experienced by each as plume migrates continuously. The simpler models predict narrower uncertainty ranges compared to those of the more complex models. At EOM, the difference between P10 storage ratio and P90 storage ratio in simpler models is less than 0.04 while the difference of that in complex models is greater than 0.14. In summary,

geologic factors and the associated conceptual model uncertainty can dominate the uncertainty in predicting storage ratio, brine leakage, and plume footprint. At the study site, better characterization of geologic data such as porosity-permeability transform and facies correlation structure can lead to reduced prediction uncertainty. Moreover, when reservoir temperature is relatively low (the -1 case temperature gradient), gravity-stable migration is possible. Given the current uncertainty in parameter and modeling choices, CO₂ plume predicted by the majority of simulations is either trapped near the injection site (e.g., due to low formation permeability and its heterogeneity) or is gravity-stable under conditions of higher permeability and lower temperature gradient, suggesting a low leakage risk. The inclined formation appears to be a viable candidate for safe GCS. Greater injection depth, though more expensive to operate, offers greater storage security in addition to enhanced storage capacity.

In this study, realization-based uncertainty analysis is not conducted to save computation time. Potential variability in the outcomes due to stochastic fluctuations is generally considered smaller than that due to facies variation, petrophysical property correlation, and other geologic considerations [5] [91]. Although DoE can evaluate correlated factors, MC analysis outcomes can lose accuracy when the degree of correlation is high [39]. Future work will investigate alternate techniques to develop conditional pdfs, in addition to updating the factor pdfs with new characterization data. Moreover, if an injection test is carried out at the study site, RS-based history matching can be conducted to reduce the current static model uncertainty, leading to more accurate future reservoir predictions. Finally, this study relies on statistical correlations of petrophysical properties developed from site or analog data, although such correlations may fail to be representative for locations away from the observed data [92]. Given our sensitivity analysis results (e.g., porosity-permeability transform is important when model complexity is accounted for), future research will aim to develop accurate and site-specific predictive petrophysical relations based on data such as sediment texture, composition, cement attributes, and burial history reconstruction [78].

Future work can also access other sources, for example, the uncertainty of estimated coefficients in the RS function. Clearly there could be multiple possible models for a second-order polynomial RS function, thus these coefficients in the RS function are uncertain. Confidence intervals of these coefficients could be established using statistical tests. Another uncertainty of particular interest could be process uncertainty in modeling CO₂ storage in geological formations, e.g., fluid/rock reactions, coupled flow and geomechanics, coupled flow with heat transfer (the energy balance equation and the flow equation are solved together), density-driven convection by CO₂-saturated brine, etc. These processes may exert profound influences on the fate of CO₂ flow, storage, and possible leakage from the reservoir, although they have not been evaluated in this study

where simulation runs are conducted with a single simulator (i.e., GASWAT). GASWAT cannot currently model many of these processes, though its capability may expand with time *as we gain insights concerning the importance of these processes*. For example, given a fixed petrophysical model, CO₂ storage can be simulated using different simulators with different levels of capabilities [93]. The results can be analyzed with the DoE to assess the importance of individual or combined processes (e.g., flow is coupled with reaction, which is further coupled to thermal and/or geomechanical processes). Such an analysis can be accomplished in future research to better understand process uncertainty and their importance in determining the fate of CO₂ in the subsurface. Conclusions

Appendix A

Example Script of Eclipse 300 GASWAT simulation

RUNSPEC

TITLE

BASE_CASE_STRUCTURAL

WELLDIMS

1 15 2 1 /

START

1 JAN 2011 /

GASWAT

PETOPTS

INITNNC /

MONITOR

UNIFIN

UNIFOUT

FIELD

DIMENS

126 162 15 /

–used for debug

–NOSIM

SATOPTS

HYSTER/

REGDIMS

1 /

TABDIMS

2 1 60 5* 1 1* 1* 1* 1 /

COMPS

2/

NSTACK

50/

AQUDIMS

– 4* analytical-aquifers connection-blocks

4* 6 2430 /

GRID

INCLUDE

'CASE_GRID.INC' /

INCLUDE

'CASE_GRID.GRDECL' /

INCLUDE

'CASE_PROP_PERMX.GRDECL' /

INCLUDE

'CASE_PROP_PERMY.GRDECL' /


```
INCLUDE
```

```
'CASE_PROP_PERMZ.GRDECL' /
```

```
INCLUDE
```

```
'CASE_PROP_PORO.GRDECL' /
```

```
INCLUDE
```

```
'CASE_PROP_NTG.GRDECL' /
```

```
EDIT
```

```
PROPS
```

```
EOS
```

```
PR/
```

```
–Reservoir salinity (unit in molarity)
```

```
SALINITY
```

```
1.9013/
```

```
–Regional Reservoir salinity
```

```
SALINTR
```

```
1.9013/
```

```
EHYSTR
```

```
1* 0 1* 1* KR/
```

```
GSF
```

```
– GASWAT case (primary drainage curve of gas phase)
```

```
– Gas saturation function Hysteresis(drainage curve)
```

```
–TABLE 1: drainage curve of gas phase for saline formation
```

```
– Source: SPE99326,Viking formation, data is modified
```

```
– Sg krg,drn
```

```
0.000 0.0000 0
```

```
0.060 0.0000 0
```

```
0.152 0.0230 0
```

```
0.205 0.0350 0
```

```
0.273 0.0370 0
```

0.342 0.0570 0
 0.430 0.0980 0 /

–table 2 (imbibition curve)

– Gas Bounding imbibition curve(different from the primary drainage curve)

– Sg' krg, ibm

0.200 0.0000 0
 0.320 0.0080 0
 0.340 0.0180 0
 0.360 0.0310 0
 0.380 0.0460 0
 0.400 0.0630 0
 0.430 0.0980 0 /

WSF

– for GASWAT case (primary drainage of water phase)

–TABLE 1: drainage curve of water phase for saline formation

– Source: SPE99326,(Viking formation)

– Sw krw

0.570 0.0000
 0.658 0.0960
 0.727 0.1860
 0.795 0.2660
 0.848 0.3410
 0.940 0.5280
 1.000 1.0000 /

– bounding imbibition (assume the same as the primary drainage curve)

– table 2 (imbibition curve)

– Sw Krw

0.570 0.0000
 0.658 0.0960
 0.727 0.1860
 0.795 0.2660
 0.848 0.3410
 0.940 0.5280

1.000 1.0000 /

CNAMES

CO2 H2O /

TCRIT

548.46 1165.14 /

PCRIT

1071.33808767417 3197.84866773523 /

VCRIT

1.50573524 0.89703376 /

ZCRIT

0.27408 0.22942 /

VCRITVIS

1.50573524 0.89703376 /

ZCRITVIS

0.27408 0.22942 /

MW

44.01 18.015 /

ACF

0.225 0.344 /

OMEGAA

0.457235529 0.457235529 /

OMEGAB

0.077796074 0.077796074 /

SSHIFT

-0.0427303384582379 0.014263521541762 /

BIC

0.0 /

PARACHOR

78 53.1 /

ROCKOPTS

1* 1* ROCKNUM /

ROCK

5801.5 9.8141E-007 /

REGIONS

SATNUM

306180*1 /

IMBNUM

306180*2 /

ROCKNUM

306180*1 /

PVTNUM

306180*1 /

FIPNUM

306180*1 /

SOLUTION

INCLUDE

'CASE.SOL.PROPS.GRDECL' /

SWAT

306180*1 /

SGAS

306180*0 /

ZMF

306180*0

306180*1 /

AQUCHWAT

1 14272.56 PRESSURE 10126.77 20 1* 1* 2* YES /

2 5151.82 PRESSURE 6096.34 20 1* 1* 2* YES /

3 5151.82 PRESSURE 6096.34 20 1* 1* 2* YES /

4 0 PRESSURE 3819.76 20 1* 1* 2* YES /

5 5151.82 PRESSURE 6096.34 20 1* 1* 2* YES /

6 5151.82 PRESSURE 6096.34 20 1* 1* 2* YES /

/

AQUANCON

–We mostly care about 3 & 4 (brine leakage)

4 126 126 1 162 1 15 I+ 2* YES /

1 1 1 1 162 1 15 I- 2* YES /

5 1 126 1 1 1 15 J- 2* YES /

2 1 126 162 162 1 15 J+ 2* YES /

6 1 126 1 162 15 15 K+ 2* YES /

3 1 126 1 162 1 1 K- 2* YES /

/

SUMMARY

RUNSUM

–Aquifer influx rate

AAQR

/

–Cumulative aquifer influx

AAQT

/

–Aquifer pressure

AAQP

/

–Res Volume Injection Rate

FVIR

–Res Volume Injection Total

FVIT

–Gas Injection Total at well

WGIT

/

– Molar amount of specified component dissolved in water

FCWM

1 / – component 1 (CO₂)

– Molar amount of specified component mobile in gas

FCGMM

1 /

– Molar amount of specified component trapped in gas

FCGMI

1 /

– Component Molar Injection Total

FCMIT

1 /

PERFORMA

FGIPL – Gas in place (liquid phase) solution gas

FGIPG – free gas in place

FGIP – total gas in place (liquid+gas)

FGIT – total gas injected

FGIR – Field gas injection rate

FWCD – Dissolved in water

FGCDI –immobile gas

FGCDM –mobile gas

FPR –Field Pressure

–Flowing bottom hole pressure

WBHP

/

–regional gas in place, but we have only 1 region

–RGIP

–/

–AACMR

–2 1 /

–/

SCHEDULE

TSCRIT

– INIT MIN MAX

– STEP STEP STEP

0.1 1E-3 1* /

CVCRIT

– 1* MAX 1* MAX

– NEWTON LINEAR

1* 1* 1* 150 /

RPTSCHED

/

RPTRST

–XMF Liquid CO2 composition

–AQSP output of aqueous speciation

BASIC=2 FIP TEMP PRES SGAS SGTRH SWAT XMF XFW CFW YMF YFW

DENG DENW VWAT VGAS AQPH AQSP /

WELSPECS

–'INJ1' is the simulation well name used to describe flow from 'INJ1'

INJ1 'GROUP 1' 38 112 1* GAS 3* NO /

/

COMPDAT

```
INJ1 38 112 1 1 OPEN 1* 0.1161 0.62500 97.48 0.00 1* Z 119.16 /
INJ1 38 112 2 2 OPEN 1* 0.1286 0.62500 107.91 0.00 1* Z 119.16 /
INJ1 38 112 3 3 OPEN 1* 0.1630 0.62500 136.78 0.00 1* Z 119.16 /
INJ1 38 112 4 4 OPEN 1* 0.4046 0.62500 339.54 0.00 1* Z 119.16 /
INJ1 38 112 5 5 OPEN 1* 1.2726 0.62500 1068.04 0.00 1* Z 119.16 /
INJ1 38 112 6 6 OPEN 1* 0.8120 0.62500 681.53 0.00 1* Z 119.16 /
INJ1 38 112 7 7 OPEN 1* 0.1138 0.62500 95.52 0.00 1* Z 119.16 /
INJ1 38 112 8 8 OPEN 1* 0.1216 0.62500 102.06 0.00 1* Z 119.16 /
INJ1 38 112 9 9 OPEN 1* 0.1462 0.62500 122.70 0.00 1* Z 119.16 /
INJ1 38 112 10 10 OPEN 1* 0.0851 0.62500 71.42 0.00 1* Z 119.16 /
INJ1 38 112 11 11 OPEN 1* 0.0029 0.62500 2.48 0.00 1* Z 121.59 /
INJ1 38 112 12 12 OPEN 1* 0.0031 0.62500 2.64 0.00 1* Z 121.59 /
INJ1 38 112 13 13 OPEN 1* 0.0028 0.62500 2.39 0.00 1* Z 121.59 /
INJ1 38 112 14 14 OPEN 1* 0.0028 0.62500 2.34 0.00 1* Z 121.59 /
INJ1 38 112 15 15 OPEN 1* 0.0027 0.62500 2.30 0.00 1* Z 121.59 /
/
```

GRUPTREE

```
'GROUP 1' FIELD /
/
```

WELLSTRE

```
- CO2 H2O
seqCO2 1.0 0.0 /
/
```

WINJGAS

```
INJ1 STREAM seqCO2/
/
```

WCONINJE

```
INJ1 GAS 1* RATE 19300.00 1* 10973.4120 /
/
```

DATES

```
1 JAN 2021 /
/
```



```
DATES
1 JAN 2031 /
/
DATES
1 JAN 2041 /
/
DATES
1 JAN 2051 /
/
DATES
1 JAN 2061 /
/
WCONINJE
INJ1 GAS SHUT RATE 0.00 1* 10973.4120 /
/
TSCRIT
– INIT MIN MAX
– STEP STEP STEP
0.1 1E-3 365 /
DATES
1 JAN 2070 /
/
DATES
1 JAN 2090 /
/
DATES
1 JAN 2130 /
/
DATES
1 JAN 2170 /
/
DATES
1 JAN 2210 /
/
DATES
1 JAN 2250 /
/
DATES
1 JAN 2290 /
```

```
/
DATES
1 JAN 2330 /
/
DATES
1 JAN 2370 /
/
DATES
1 JAN 2410 /
/
DATES
1 JAN 2450 /
/
DATES
1 JAN 2490 /
/
DATES
1 JAN 2530 /
/
DATES
1 JAN 2570 /
/
DATES
1 JAN 2610 /
/
DATES
1 JAN 2650 /
/
DATES
1 JAN 2690 /
/
DATES
1 JAN 2730 /
/
DATES
1 JAN 2770 /
/
DATES
1 JAN 2810 /
```

```
/
DATES
1 JAN 2850 /
/
DATES
1 JAN 2890 /
/
DATES
1 JAN 2930 /
/
DATES
1 JAN 2970 /
/
DATES
1 JAN 3010 /
/
DATES
1 JAN 3050 /
/
DATES
1 JAN 3090 /
/
DATES
1 JAN 3130 /
/
DATES
1 JAN 3170 /
/
DATES
1 JAN 3210 /
/
DATES
1 JAN 3250 /
/
DATES
1 JAN 3290 /
/
DATES
1 JAN 3330 /
```

```
/
DATES
1 JAN 3370 /
/
DATES
1 JAN 3410 /
/
DATES
1 JAN 3450 /
/
DATES
1 JAN 3490 /
/
DATES
1 JAN 3530 /
/
DATES
1 JAN 3570 /
/
DATES
1 JAN 3610 /
/
DATES
1 JAN 3650 /
/
DATES
1 JAN 3690 /
/
DATES
1 JAN 3730 /
/
DATES
1 JAN 3770 /
/
DATES
1 JAN 3810 /
/
DATES
1 JAN 3850 /
```

```
/
DATES
1 JAN 3890 /
/
DATES
1 JAN 3930 /
/
DATES
1 JAN 3970 /
/
DATES
1 JAN 4010 /
/
Example script of Eclipse 300 GASWAT simulation
```

Bibliography

- [1] J E Fox, P W Lambert, R F Mast, N W Nuss, and R D Rein. Porosity Variation in the Tensleep and its Equivalent the Weber Sandstone, Western Wyoming: a Log and Petrographic Analysis. *Rocky Mountain Association of Geologists Symposium*, pages 185–215, 1975.
- [2] S Benson. Relative Permeability Explorer Beta. <http://pangea.stanford.edu/research/bensonlab>, 2006.
- [3] IPCC. Carbon Dioxide Capture and Storage, Chp 5, Underground Geological Storage. <http://www.ipcc.ch/pdf/special-reports/srccs/>, 2005.
- [4] P.H. Stauffer, R.C. Surdam, Z. Jiao, and Bentley R.D. Miller, T.A. Combining Geologic Data and Numerical Modeling to Improve Estimates of the CO₂ Sequestration Potential of the Rock Springs Uplift, Wyoming. *Energy Procedia*, 1:2717–2724, 2009.
- [5] S Q Li, Y Zhang, and X Zhang. Geologic Modeling and Fluid-flow Simulation of Acid Gas Disposal in Western Wyoming. *AAPG Bulletin*, page in press, 2011.
- [6] J M Nordbotten, M A Celia, S Bachu, and H K Dahle. Semianalytical Solution for CO₂ Leakage through an Abandoned Well. *Environmental Science and Technology*, 39(2):602–611, 2005.
- [7] A Firoozabadi and P Cheng. Prospects for Subsurface CO₂ Sequestration. *American Institute of Chemical Engineers*, 56:1398–1405, DOI 10.1002/aic.12287, 2010.
- [8] C Lu, W S Han, S L, B J McPherson, and P C Lichtner. Effects of Density and Mutual Solubility of a CO₂-Brine System on CO₂ Storage in Geological Formations: "Warm" vs. "Cold" Formations. *Advances in Water Resources*, 32:1685–1702, DOI 10.1016/j.advwaters.2009.07.008, 2009.
- [9] Stefan Bachu. Screening and Ranking of Sedimentary Basins for Sequestration of CO₂ in Geological Media in Response to Climate Change. *Environmental Geology*, 44:277–289, 2003.

- [10] K Michael, A Golab, V Shulakova, J EnnisKing, G Allinson, S Sharma, and T Aiken. Geological Storage of CO₂ in Saline Aquifers: A Review of the Experience from Existing Storage Operations. *Int. J. Greenhouse Gas Control*, 4:659–667, 2010.
- [11] S T Ide, K Jessen, and F M Orr Jr. Storage of CO₂ in Saline Aquifers: Effects of Gravity, Viscous, and Capillary Forces on Amount and Timing of Trapping. *International Journal of Greenhouse Gas Control*, 1:481–491, 2007.
- [12] L W Gelhar. *Stochastic Subsurface Hydrology*. Prentice Hall, New York, 1992.
- [13] M Flett, R Gurton, and G Weir. Heterogeneous Saline Formations for Carbon Dioxide Disposal: Impact of Varying Heterogeneity on Containment and Trapping. *Journal of Petroleum Science and Engineering*, 57:106–118, 2007.
- [14] S Q Li, Y Zhang, and X Zhang. A Study of Conceptual Model Uncertainty in Large Scale CO₂ Storage Simulation. *Water Resources Research*, 47:W05534, doi:10.1029/2010WR009707., 2011.
- [15] A Kumar, M Noh, G A Pope, K Sepehrnoori, S Bryant, and L W Lake. Reservoir Simulation of CO₂ Storage in Deep Saline Aquifers. *SPE*, (89343):SPE/DOE Symposium on Improved Oil Recovery, 17–21 April 2004, Tulsa, Oklahoma, 2004.
- [16] R Juanes, E J Spiteri, F M Orr Jr., and M J Blunt. Impact of Relative Permeability Hysteresis on Geological CO₂ Storage. *Water Resources Research*, 42:W12418, DOI 10.1029/2005WR004806, 2006.
- [17] C Doughty. Modeling Geologic Storage of Carbon Dioxide: Comparison of Non-hysteretic and Hysteretic Characteristic Curves. *Energy Conversion and Management*, 48:1768–1781, 2007.
- [18] E Spiteri and R Juanes. Impact of Relative Permeability Hysteresis on the Numerical Simulation of WAG Injection. *Journal of Petroleum Science and Engineering*, 50:115–139, 2006.
- [19] W S Han and B J McPherson. Optimizing Geologic CO₂ Sequestration by Injection in Deep Saline Formations below Oil Reservoirs. *Energy Conversion and Management*, 50:2570–2582, 2009.
- [20] R Qi, T C LaForce, and M J Blunt. Design of Carbon Dioxide Storage in Aquifers. *International Journal of Greenhouse Gas Control*, 3:195–205, 2009.
- [21] K Sasaki, T Fujii, Y Niibori, T Ito, and T Hashida. Numerical Simulation of Supercritical CO₂ Injection into Subsurface Rock Masses. *Energy Conversion and Management*, 49:54–61, 2007.

- [22] Q Zhou, J T Birkholzer, C Tsang, and J Rutqvist. A Method for Quick Assessment of CO₂ Storage Capacity in Closed and Semi-closed Saline Formations. *International Journal of Greenhouse Gas Control*, 2:626–639, 2008.
- [23] H Yamamoto, K Zhang, K Karasaki, A Marui, H Uehara, and N Nishikawa. Numerical Investigation Concerning the Impact of CO₂ Geologic Storage on Regional Groundwater Flow. *International Journal of Greenhouse Gas Control*, 3:586–599, 2009.
- [24] B Liu, Y Zhang, and X Zhang. Acid Gas Storage in a Deep Saline Aquifer: A Numerical Sensitivity Study on Parameter and Model Uncertainty. *Journal of Hazardous, Toxic, and Radioactive Waste*, 15(4):doi:10.1061/(ASCE)HZ.1944–8376.0000061., 2011.
- [25] C D White, B J Willis, K Narayanan, and S P Dutton. Identifying and Estimating Significant Geologic Parameters with Experimental Design. *SPE Journal*, 6(3):311–324, 2001.
- [26] C Y Peng and R Gupta. Experimental Design and Analysis Methods in Multiple Deterministic Modeling for Quantifying Hydrocarbon In-Place Probability Distribution Curve. *SPE*, (87002-MS):Proceedings: Asia Pacific Conference on Integrated Modelling for Asset Management, 29–30 March 2004, Kuala Lumpur, Malaysia, 2004.
- [27] D K Larue and F Friedmann. Stratigraphic Uncertainty in Field Development Studies: a Conceptual Modeling Approach. *The Leading Edge*, January:28–33, 2001.
- [28] F X Jian, D K Larue, and A J Toldi. Reservoir Modeling Methods and Characterization Parameters for a Shoreface Reservoir: What is Important for Fluid Flow Performance? *SPE*, (77428), 2002.
- [29] A Castellini, A Chawathe, D Larue, J L Landa, F X Jian, and J L Toldi. What is Relevant to Flow? A Comprehensive Study Using a Shallow Marine Reservoir. *SPE*, (79669):Paper prepared for presentation at the SPE Reservoir Simulation Symposium held in Houston, Texas, 3–5 Feb, 2003, 2003.
- [30] H Li and C D White. Geostatistical Models for Shales in Distributary Channel Point Bars (Ferron Sandstone, Utah): from Ground-penetrating Radar Data to Three-dimensional Flow Modeling. *AAPG Bulletin*, 87(12):1851–1868, 2003.
- [31] W S Meddaugh, S D Griest, and S J Gross. *Application of Design of Experiments to Expedite Probabilistic Assessment of Reservoir Hydrocarbon Volumes (OOIP)*, pages 751–756. 2004. in book: Geostatistics Banff.

- [32] W J Milliken, M Levy, S Strebelle, and Y Zhang. The Effect of Geologic Parameters and Uncertainties on Subsurface Flow: Deepwater Depositional Systems. *SPE*, (109950):Paper was prepared for presentation at the 2007 SPE Annual Technical Conference and Exhibition held in Anaheim, California, 11–14 Nov. 2007., 2007.
- [33] K Choi, M Jackson, G Hampson, A Jones, and T Reynolds. Impact of Heterogeneity on Flow in Fluvial-Deltaic Reservoirs: Implications for the Giant ACG Field, South Caspian Basin. *SPE*, (107137):Paper was prepared for presentation at the SPE Europe/EAGE Annual Conference and Exhibition held in London, UK, 11–14 June, 2007., 2007.
- [34] I Zabalza-Mezghani, E Manceau, M Feraille, and A Jourdan. Uncertainty Management: from Geological Scenarios to Production Scheme Optimization. *Journal of Petroleum Science and Engineering*, 44:11–25, 2004.
- [35] B Yeten, A Castellini, B Guyaguler, and W H Chen. A Comparison Study on Experimental Design and Response Surface Methodologies. *SPE*, (93347):Paper was prepared for presentation at the 2005 SPE Reservoir Simulation Symposium held in Houston, Texas, 31 Jan – 2 Feb, 2005., 2005.
- [36] B Li and F Friedmann. A Novel Response Surface Methodology Based on “Amplitude Factor” Analysis for Modeling Nonlinear Responses Caused by Both Reservoir and Controllable Factors. *SPE*, (95283):Paper was prepared for presentation at the 2005 SPE Annual Technical Conference and Exhibition held in Dallas, Texas, 9–12 Oct., 2005., 2005.
- [37] B Li and F Friedmann. Semiautomatic Multiple Resolution Design for History Matching. *SPE*, (102277):Paper was prepared for presentation at the 2006 SPE Annual Technical Conference and Exhibition held in San Antonio, Texas, 24–27 Sept., 2006, 2006.
- [38] B Bourbiaux. Fractured Reservoir Simulation: a Challenging and Rewarding Issue. *Oil and Gas Science and Technology*, 65(2):227–238, 2010.
- [39] F Wang and C D White. Designed Simulation for a Detailed 3D Turbidite Reservoir Model. *SPE*, (75515):Paper was prepared for presentation at the SPE Gas Technology Symposium held in Calgary, Alberta, Canada, 30 April–2 May, 2002., 2002.
- [40] F Friedmann, A Chawathe, and D K Larue. Assessing Uncertainty in Channelized Reservoirs Using Experimental Design. *SPE Reservoir Evaluation and Engineering*, (85117):264–274, 2003.

- [41] G M Narahara, J J Spokes, D D Brennan, G Maxwell, and M Bast. Well Count Optimization Incorporating a Wide Range of Uncertainties for the Deepwater Agbami Field. *SPE*, (16988):Paper was prepared for presentation at the Offshore Technology Conference held in Houston, Texas, 3–6 May, 2004., 2004.
- [42] M S Al Salhi, M F Van Rijen, Z A Alias, F Visser, H Dijk, H M Lee, R H Timmerman, A A Upadhyaya, and L Wei. Reservoir Modeling for Redevelopment of a Giant Fractured Carbonate Field, Oman: Experimental Design for Uncertainty Management and Production Forecasting. *SPE*, (10537):Paper was prepared for presentation at the International Petroleum Technology Conference held in Doha, Qatar, 21–23 Nov., 2005., 2005.
- [43] J Zhang, M Delshad, and K Sepehrnoori. Development of a Framework for Optimization of Reservoir Simulation Studies. *Journal of Petroleum Science and Engineering*, 59:135–146, 2007.
- [44] C Amudo, T Graf, N R Harris, R Dandekar, F Ben Amor, and R S May. Experimental Design and Response Surface Models as a Basis for Stochastic History Match – a Niger Delta Experience. *IPTC*, (12665):Paper was prepared for presentation at the International Petroleum Technology Conference held in Kuala Lumpur, Malaysia, 3–5 Dec., 2008., 2008.
- [45] K J Wood, L W Lake, R T Johns, and V Nunez. A Screening Model for CO₂ Flooding and Storage in Gulf Coast Reservoirs Based on Dimensionless Groups. *SPE Reservoir Evaluation and Engineering*, (100021):513–520., 2008.
- [46] W Sifuentes, M J Blunt, and M A Giddins. Modeling CO₂ Storage in Aquifers: Assessing the Key Contributors to Uncertainty. *SPE*, (123582):Paper was prepared for presentation at the 2009 SPE Offshore Europe Oil and Gas Conference and Exhibition held in Aberdeen, UK, 8–11 Sept., 2009, 2009.
- [47] A Forooghi, A A Hamouda, and T Eilertsen. Co-optimization of CO₂ EOR and Sequestration in a North Sea Chalk Reservoir. *SPE*, (125550):Paper was prepared for presentation at the 2009 SPE/EAGE Reservoir Characterization and Simulation Conference held in Abu Dhabi, UAE, 19–21, Oct., 2009, 2009.
- [48] Y Ghomian, K Sepehrnoori, and G A Pope. Efficient Investigation of Uncertainties in Flood Design Parameters for Coupled CO₂ Sequestration and Enhanced Oil Recovery. *SPE*, (139738):Paper was prepared for presentation at the SPE International Conference on CO₂ Capture, Storage, and Utilization held in New Orleans, Louisiana, 10–12 Nov., 2010., 2010.

- [49] P M O'Dell and K C Lindsey. Uncertainty Management in a Major CO₂ EOR Project. *SPE*, (137998):Paper was prepared for presentation at the Abu Dhabi International Petroleum Exhibition and Conference held in Abu Dhabi, UAE, 1–4 Nov., 2010., 2010.
- [50] S Purwar, C J Jablonowski, and Q P Nguyen. A Method for Integrating Response Surfaces into Optimization Models with Real Options: A Case Study in Gas Flooding. *SPE*, (129566):Paper was prepared for presentation at the SPE Hydrocarbon Economics and Evaluation Symposium held in Dallas, Texas, 8–9 March, 2010, 2010.
- [51] Y Ghomian, G A Pope, and K Sepehrnoori. Hysteresis and Field-Scale Optimization of WAG Injection for Coupled CO₂-EOR and Sequestration. *SPE*, (110639): Paper was prepared for presentation at the 2008 SPE/DOE Improved Oil Recovery Symposium held in Tulsa, Oklahoma, 19–23 April, 2008, 2008.
- [52] Y Mosse, E Portier, and T Schaaf. CCS Project in a Gas Field of the Sbaa Basin, SW Algeria - What is at Stake? *SPE*, (128495):Paper was prepared for presentation at the SPE North Africa Technical Conference and Exhibition held in Cairo, Egypt, 14–17 Feb., 2010., 2010.
- [53] A N Beni, C Clauser, and M Erlstrom. System Analysis of Underground CO₂ Storage by Numerical Modeling for a Case Study in Malmo. *American Journal of Science*, 311:335–368, DOI 10.2475/04.2011.03, 2011.
- [54] Q Zhou, J T Birkholzer, E Mehnert, Y Lin, and K Zhang. Modeling Basin- and Plume-Scale Processes of CO₂ Storage for Full-Scale Deployment. *Ground Water*, 48:494–514, DOI 10.1111/j.1745–6584.2009.00657.x, 2010.
- [55] Douglas C. Montgomery. *Design and Analysis of Experiments*. John Wiley & Sons, Inc, 7th edition, 2008.
- [56] R.H. Myers and D.C. Montgomery. *Response Surface Methodology — Process and Product Optimization Using Designed Experiments*. John Wiley & Sons, New York, 1995.
- [57] P.R. Lamerson. The Fossil Basin and its Relationship to the Absaroka Thrust System, Wyoming and Utah. *Rocky Mountain Association of Geologists*, 1(Geological Studies of the Cordilleran Thrust Belt):279–340, 1982.
- [58] F. Royse. *An Overview of the Geological Structure of the Thrust Belt in Wyoming, Northern Utah and Eastern Idaho*, pages 273–311. 1982. Geology Of Wyoming.
- [59] M.E. Maclachlan. Triassic System, Geological Atlas of the Rocky Mountain Region. *Rocky Mountain Association of Geologists*, pages 166–176, 1972.

- [60] J.A. Peterson. Triassic System, Geological Atlas of the Rocky Mountain Region. *Rocky Mountain Association of Geologists*, pages 177–189, 1972.
- [61] C. Fraley. Algorithms for Model-based Gaussian Hierarchical Clustering. *SIAM Journal of Scientific Computing*, 20(1):270–281, 1998.
- [62] J Gidman, F J Conner, and D J Fischer. Deciphering Core and Log Porosity Differences and Evaluating the Scale Dependency of Core Analysis in a Complex Lithology. *SCA*, (9411), 1994.
- [63] S J Lindquist. Practical Characterization of Eolian Reservoirs for Development: Nugget Sandstone, Utah-Wyoming Thrust Belt. *Sedimentary Geology*, 56:315–339, 1988.
- [64] M M Saggaf and Ed L Nebrijia. A Fuzzy Logic Approach for the Estimation of Facies from Wire-line Logs. *AAPG Bulletin*, 87:1223–1240, DOI 10.1306/02260301019, 2003.
- [65] Senenergy Ltd. *Interactive Petrophysics V 3.6 Online Help Manual*, 2010.
- [66] Wyoming Oil Gas Conservation Commission. Wyoming Oil Gas Conservation Commission Online Well Database. <http://wogcc.state.wy.us>.
- [67] Final Report: Carbon Sequestration Monitoring Activities; Department of Energy Agreement no. de-nt0004730. Technical report, Laramie, Wyoming, 2011.
- [68] B Bennion and S Bachu. Supercritical CO₂ and H₂S-Brine Drainage and Imbibitions Relative Permeability Relationships for Intergranular Sandstone and Carbonate Formations. *SPE*, (99326):Society of Petroleum Engineers of Europec/EAGE, Vienna, Austria, 2006.
- [69] B Bennion and S Bachu. The Impact of Interfacial Tension and Pore-size Distribution/Capillary Pressure Character on CO₂ Relative Permeability at Reservoir Conditions in CO₂-brine Systems. *SPE*, (99325):Society of Petroleum Engineers of Europec/EAGE, Vienna, Austria, 2006.
- [70] L E Tillman. Sedimentaty Facies and Reservoir Characteristics of the Nugget Sandstone (Jurassic), Painter Reservoir Filed, Uinta County, Wyoming. *Rocky Mountain Association of Geologists Symposium - Sandstone Reservoirs*, pages 97–108, 1989.
- [71] S J Lindquist. Nugget Formation Reservoir Characteristics Affecting Production in the Overthrust Belt of Southwestern Wyoming. *Journal of Petroleum Technology*, 35:1355–1365, 1983.

- [72] D L Cox, S J Lindquist, C L Bargas, K G Havholm, and R M Srivastava. Intergrated Modeling for Optimum Management of a Giant Gas Condensate Reservoir, Jurassic Eolian Nugget Sandstone, Anschutz Ranch East Field, Utah Overthrust (U.S.A.). *AAPG Computer Applications in Geology*, 3:287–321, 1994.
- [73] D J Keele. The Marriage of Eolian Rock Properties and the Style of the Structural Deformation of the Nugget Formation; Anschutz Ranch East Field: Northeast Utan and Southwest Wyoming. *MS thesis*, page Utah State University, 2008.
- [74] S E Laubach, R M Reed, and R H Lander. Fracture with Crack-seal Texture and Porosity, Depth 6274 m, Wyoming (Photograph of the Month). *Journal of Structural Geology*, 32:p.1865, DOI 10.1016/j.jsg.2010.10.003, 2010.
- [75] E. A. Pinzon, A. Ortiz, and S. E. Laubach. New Techniques on Fracture Pattern Characterization: An Example of Comparison between Jurassic Nugget Sandstones (Utah Rocky Mountains) and Eocene Mirador Formation Sandstones (Colombia Llanos Foothills Basin). *European Association of Geoscientists and Engineers (EAGE)*, 2006.
- [76] H. Lewis and G. D. Couples. *Production Evidence for Geological Heterogeneities in the Anschutz Ranch East Field, western USA*, pages 321–338. 1993. in North, C. P., and Prosser, D. J. (eds), Geological Society of London Special Publication 73.
- [77] S. Morad, K. Al-Ramadan, J. M. Ketzer, and L. F. De Ros. The Impact of Diagenesis on the Heterogeneity of Sandstone Reservoirs: a Review of the Role of Depositional Facies and Sequence Stratigraphy. *AAPG Bulletin*, 94(8):1267–1309, 2010.
- [78] J M Ajdukiewicz and R H Lander. Sandstone Reservoir Quality Prediction: The State of the Art. *AAPG Bulletin*, 94:1083–1091, DOI 10.1306/intro060110, 2010.
- [79] N.M. Doelger. *The Stratigraphy of the Nugget Sandstone*, pages 163–178. 1987. WGA, The Thrust Belt Revisited.
- [80] A D Hansen. Reservoir Characterization and Outcrop Analogs to the Navajo Sandstone in the Central Utah Thrust Belt Exploration Play. *MS thesis*, 2007.
- [81] G A Kocurek. *Sedimentary Environments (3rd Edition)*. Blackwell Science, Cambridge Massachusetts, 1996.
- [82] W M Jordan. *Regional Environmental Study of the Early Mesozoic Nugget and Navajo Sandstones*. PhD thesis, Univ. Wisconsin, Madison, 1965.

- [83] G A Kocurek and R H Dott. Jurassic Paleogeography and Paleoclimate of the Central and Southern Rocky Mountains Regions. *Rocky Mountain Section, Society for Sedimentary Geology*, pages 101–116, 1983.
- [84] Schlumberger. *Petrel User's Manual*, 2009.
- [85] Y Z Ma. Propensity and Probability in Depositional Facies Analysis and Modeling. *Mathematical Geosciences*, 41:737–760, 2009.
- [86] Y Z Ma, A Seto, and E Gomez. Depositional Facies Analysis and Modeling of the Judy Creek Reef Complex of the Upper Devonian Swan Hills, Alberta, Canada. *AAPG Bulletin*, 93(9):1235–1256, 2009.
- [87] W J Milliken, A S Emanuel, and A Chakrabarty. Applications of 3D Streamline Simulation to Assist History Matching. *SPE*, (74712):This paper was revised for publication from paper SPE 63155, first presented at the 2000 SPE Annual Technical Conference and Exhibition, Dallas, 1–4 October., 2001.
- [88] Schlumberger. *ECLIPSE Technical Manual: the GASWAT Option*, 2009.
- [89] M W West. Seismotectonics of North-Central Utah and Southwestern Wyoming (Speical Study). *Paleoseismology of Utah*, 4, 1994.
- [90] J Carrera and S P Neuman. Estimation of Aquifer Parameters under Transient and Steady State Conditions: 3. Application to Synthetic and Field Data. *Water Resources Research*, 22:228–242, 1986.
- [91] Seto A. Gomez Ernest Ma, Y. Z. Frequentist Meets Spatialist: A Marriage Made in Reservoir Characterization. *SPE*, (115836), 2008. Society of Petroleum Engineers, AIME, San Antonio,Texas.
- [92] T R Taylor, M R Giles, L A Hathon, T N Diggs, N R Braunsdorf, G V Birbiglia, M G Kittridge, C I Macaulay, and I S Espejo. Sandstone Diagenesis and Reservoir Quality Prediction: Models, Myths, and Reality. *AAPG Bulletin*, 94(8):1093–1132, 2010.
- [93] H Class, A Ebigbo, R Helmig, H K Dahle, J M Nordbotten, M A Celia, P Audigane, M Darcis, J Ennis-King, Y Fan, B Flemisch, S E Gasda, M Jin, S Krug, D Labregere, A N Beni, R J Pawar, A Sbai, S G Thomas, L Trenty, and L Wei. A Benchmark Study on Problems Related to CO₂ Storage in Geologic Formations. *Computational Geosciences*, 13:409–434, DOI 10.1007/s10596-009-9146-x, 2009.